

RUPRECHT-KARLS-UNIVERSITÄT HEIDELBERG



KIRCHHOFF-INSTITUT FÜR PHYSIK

Habilitationsschrift

zur

Erlangung der Venia legendi
für das Fach Physik

der

Ruprecht-Karls-Universität
Heidelberg

vorgelegt von

Marc Weber

aus Heidelberg

2000

Test of Quantum Chromodynamics with the Hadronic Final State in Deep-Inelastic Scattering at HERA

Abstract

Electron-proton collisions at HERA have opened a new kinematic regime in deep-inelastic scattering and made possible unique tests of Quantum Chromodynamics. Eight years after the start of HERA a wealth of measurements is available. The following results are discussed: (i) Perturbative QCD in next-to-leading order gives a good description of multi-jet production. Current QCD Monte Carlo models have difficulties describing the hadronic final state precisely. (ii) The value of the strong coupling α_s is found to be consistent with the world average. The renormalization scale dependence of α_s corresponds to the QCD prediction. (iii) Overall, the concept of analytical power corrections and of a universal effective strong coupling $\bar{\alpha}_0$ is supported. The resulting values of α_s determined from different observables vary significantly though. (iv) The gluon density of the proton is determined at momentum fractions $x > 0.01$. (v) Experimental signatures suggesting deviations from DGLAP parton evolution are observed at low x . Their unambiguous interpretation is not yet possible. (vi) Analyses of charged particle multiplicities and momentum spectra reveal limitations of analytical QCD predictions.

Contents

1	Introduction	1
1.1	Fundamentals of QCD	1
1.2	The QCD Lagrangian	2
1.3	The renormalization group equation	4
1.4	Deep-inelastic scattering	6
1.5	Parton evolution equations	9
1.6	Structure of the virtual photon	13
1.7	Fit of parton density functions	14
1.8	Di-parton cross sections	16
1.9	Parton showers and the colour dipole model	17
1.10	Hadronization models	18
1.11	Reference frames, jet algorithms and event shape observables	19
1.11.1	Reference frames	19
1.11.2	Jet algorithms	21
1.11.3	Event shape variables	23
1.12	The HERA collider	25
1.13	The H1 and ZEUS detectors	25
2	Data description and test of QCD matrix elements	28
2.1	QCD models for DIS	29
2.1.1	Radiative QED corrections	30
2.2	Perturbative QCD calculations in next-to-leading order	30
2.3	Jet shape and subjet multiplicities	33
2.4	Dijet cross sections	35
2.4.1	Jet rates at small x and Q^2	36
2.4.2	Dijet production at large Q^2 and E_T^{Breit}	37
2.4.3	Dijet production in CC and NC interactions at highest Q^2	38
2.5	Azimuthal asymmetries	41
2.6	Three-jet events	42

3	Determination of the strong coupling constant α_s	46
3.1	Principle of α_s determination	46
3.2	α_s from jet cross sections	48
3.2.1	Single inclusive jet cross sections	48
3.2.2	Differential dijet event rates	51
3.2.3	Dijet event rates $R_{2+1}(Q^2)$	53
3.3	Event shape distributions and test of power corrections	54
3.4	Overview of α_s measurements at HERA	57
4	Determination of parton densities	59
4.1	Fitting techniques	59
4.2	Gluon density from dijet events	60
4.3	Gluon density from D^* events	63
5	Test of parton evolution equations	67
5.1	E_T flow	67
5.2	Charged particle p_T spectra	68
5.3	Dijet cross sections at low Q^2 and large $E_{T\ jet}$	69
5.4	Forward jet production	71
5.5	Forward π^0 production	73
6	Inclusive particle distributions	75
6.1	Charged particle multiplicities	75
6.2	Fragmentation functions and scaling violations	76
6.3	Particle spectra at small x	78
6.4	Angular correlations	80
6.5	Current-target hemisphere correlations	82
6.6	Bose–Einstein correlations	83
7	Conclusions	87

Preface

Deep-inelastic scattering (DIS) experiments have made fundamental contributions in establishing Quantum Chromodynamics (QCD) as the theory of strong interactions. Evidence of proton structure and of the existence of partons was found through observation of Bjorken scaling in electron-nucleon scattering at SLAC [1]. The subsequent discovery of logarithmic scaling violations [2] introduced through gluon radiation off quarks supported the non-abelian structure of QCD. Later experiments extracted nucleon structure functions and performed the first measurements of the strong coupling α_s . In addition, measurements of DIS have crucially influenced the construction of the theory of electroweak interactions.

In 1992 the electron-proton collider HERA at DESY started operation. Due to its high centre-of-mass energy of $\sqrt{s} \approx 300$ GeV, HERA extends the kinematic range of fixed target experiments by several orders of magnitude in both the virtuality Q^2 of the exchanged boson and the fractional parton momentum x . Collisions at Q^2 as high as 50,000 GeV², corresponding to a spatial resolution of 10^{-18} m, and at x as small as 10^{-5} , corresponding to regions of high parton density, are accessible. The collider detectors H1 and ZEUS cover essentially the full solid angle and are instrumented to measure the scattered lepton *and* the hadronic final state precisely.

The structure of DIS events is complicated compared with the ideal situation in e^+e^- annihilation. The presence of a hadron in the initial state implies that the effective collision energy varies from event to event and that the proton's *parton densities* must be known or determined; the partons in the proton give rise to *initial-state parton showers*; the debris of the *proton remnant* may contaminate the hadronic final state; there are *two* leading order QCD processes, QCD-Compton $eq \rightarrow eqg$ and boson-gluon-fusion $eg \rightarrow eq\bar{q}$. These characteristics of DIS may make understanding of the hadronic final state challenging but simultaneously offer unique opportunities. Parton evolution equations can be investigated in the region of high parton density; jet cross sections can be studied over a huge range of Q^2 where the fractions of quark- and gluon-induced reactions or the size of non-perturbative effects vary strongly; at high Q^2 , a region is accessible where the strength of electromagnetic and weak interactions are similar; the phenomenon of diffraction can be studied. It is of fundamental importance to test QCD in such an environment where its power or its limitations may be seen very clearly.

This review presents a selection of measurements of the hadronic final state in DIS which are available as preliminary or final results in spring 2000.¹ Most of the results are based on the data collected in the years 1994-1997 corresponding to an integrated luminosity of ≈ 50 pb⁻¹. Emphasis is placed on the description of measurements which can be compared with perturbative QCD predictions in a regime where either Q^2 or another energy scale e.g. transverse jet energy are large. Analyses of the hadronic final state in diffractive processes are not described here. Corresponding reviews and related information may be found in [3].

In the first section the basic properties of QCD and of deep-inelastic scattering at HERA are introduced. In section 2 the general description of the data by QCD models and perturbative QCD calculations is studied in characteristic phase space regions. Determinations of α_s and of parton density functions, in particular of the gluon density, are presented in section 3 and 4

¹Some analyses which become available directly before the conference DIS 2000 could not be considered.

respectively. Dedicated studies of the validity of the DGLAP parton evolution equations and of the structure of the proton at small x are summarized in section 5. Finally tests of perturbative QCD using inclusive particle distributions are described in section 6.

1 Introduction

1.1 Fundamentals of QCD

Quantum Chromodynamics is a non-abelian quantum field theory describing the strong interactions of *quarks* and *gluons*. Quarks are spin-1/2 fermions with fractional electrical charge of $+2/3$ or $-1/3$. Gluons are spin-1 bosons which are electrically neutral. Quarks and gluons carry *colour charge*. There are three quarks (of each flavour) and eight gluons of different colour. The symmetry group of colour transformations is SU(3). The colour charge of gluons leads to their *self interaction*, to the characteristic energy dependence of the strong coupling and thus to *asymptotic freedom* and *confinement*. Hadrons are colour singlets composed of quarks, antiquarks and gluons. These basic features of QCD are now firmly established by experiment.

Examples of strong interactions were first observed more than 100 years ago in α decays of radioactive nuclei. Early indications for the substructure of the proton were provided by the measurement of its magnetic moment in 1933 [4]. Quarks were postulated as the basic constituents of hadrons in 1964 by Gell-Mann and Zweig [5, 6] following the discovery of numbers of hadrons in cosmic ray and early accelerator experiments. They provide a suggestive classification of hadrons similar to the arrangement of atoms in the periodic table. One year later the concept of *colour charge* was introduced [7] in order to make spin 1/2 baryons composed of three quarks obey the Pauli principle.

Independent evidence of the substructure of hadrons came from the first deep-inelastic scattering experiments at SLAC [1] and their observation of scale invariance of the DIS cross sections. DIS experiments measured the spin of the quark-partons to be 1/2. Indirect evidence for the existence of gluons came from the observation that the momentum carried by quarks is only half of that of the proton and from the discovery of scaling violations.

In the early seventies, QCD was formulated as a non-abelian gauge theory of coloured quarks and gluons [8] and its properties of asymptotic freedom and confinement were discovered [9].

In e^+e^- annihilation the angular distribution of the jets originating from $q\bar{q}$ events confirmed the spin of quarks to be 1/2 [10]. The observation of three jet events at PETRA in the reactions $e^+e^- \rightarrow q\bar{q}g$ gave direct evidence for gluons [11] and the analysis of jet angular distributions showed that the spin of the gluon is 1 [12]. At LEP the existence of the triple gluon self interaction was shown [13].

1.2 The QCD Lagrangian

Lagrangian densities provide a compact way to define the structure of a quantum field theory of elementary particle interactions. Invariance of the Lagrangian under a transformation implies an associated conservation law according to Noether's theorem. Given the Lagrangian the Feynman rules needed for perturbative calculations can be derived. The Lagrangian of QCD (omitting gauge fixing and ghost terms) is [14]

$$\mathcal{L}_{QCD} = \bar{\psi}_{f,\alpha i} \left[i(\gamma)_{\alpha\beta}^{\mu} (\partial_{\mu} \delta_{ij} + ig A_{\mu a} (T_a)_{ij}) - m_f \delta_{\alpha\beta} \delta_{ij} \right] \psi_{f,\beta j} - \frac{1}{4} F_{\mu\nu,a} F_a^{\mu\nu} . \quad (1)$$

Repeated indices are summed over. The sums run over quark flavours ($f = 1, \dots, n_f = 6$), Dirac indices ($\alpha, \beta = 1, \dots, 4$), quark colour indices ($i, j = 1, \dots, N_c = 3$), gluon colour indices ($a = 1, \dots, N_c^2 - 1 = 8$) and spacetime indices ($\mu, \nu = 0, \dots, 3$), respectively. The $\psi_{f,\alpha i}$ are Dirac spinors corresponding to quark fields of flavour f and colour i . The quarks' masses are m_f . The strong coupling g is related to α_s by

$$\alpha_s = \frac{g^2}{4\pi} . \quad (2)$$

$(A_{\mu})_{ij} = A_{\mu a} (T_a)_{ij}$ are the gluon fields where the $A_{\mu a}$ are real numbers and the $N_C \times N_C$ matrices $(T_a)_{ij}$ are the generators of $SU(N_C)$ colour transformations. The $F_a^{\mu\nu}$ are the components of the field strength tensor $F^{\mu\nu} = F_a^{\mu\nu} T_a$. They are related to the gluon fields according to

$$F_a^{\mu\nu} = \partial_{\mu} A_{\nu a} - \partial_{\nu} A_{\mu a} - gf_{abc} A_{\mu b} A_{\nu c} . \quad (3)$$

The T_a satisfy the commutation relation

$$[T_a, T_b] = T_a T_b - T_b T_a = if_{abc} T_c , \quad (4)$$

where f_{abc} are the structure constants of $SU(N_C)$. They satisfy the following relation:

$$\sum_{c,d} f_{acd} f_{bcd} = \mathbf{C}_A \delta_{ab} \quad \text{with } C_A = N_C = 3 . \quad (5)$$

The (T_a) are conventionally chosen to be proportional to the Gell-Mann matrices λ_a , $T_a = 1/2 \lambda_a$, such that they fulfil

$$\text{Tr}(T_a T_b) = \mathbf{T}_R \delta_{ab} \quad \text{with } T_R = 1/2 . \quad (6)$$

Then

$$\sum_a (T_a)_{ik} (T_a)_{kj} = \mathbf{C}_F \delta_{ij} \quad \text{with } C_F = (N_C^2 - 1)/2N_C = 4/3 . \quad (7)$$

The constants C_A , C_F and T_R are the *colour factors* of $SU(3)$.

The Lagrangian \mathcal{L}_{QCD} is invariant under local gauge transformations in colour space i.e. under redefinition of the quark and gluon fields by an unobservable phase that may vary with spacetime. Under local gauge transformations, the quark fields transform as

$$\psi_j(x) \rightarrow \psi'_j(x) = U_{ji}(x)\psi_i(x) , \quad (8)$$

where the U_{ji} are elements of $SU(N_C)$ and may be expressed as $U_{ji} = [\exp(i \sum_{a=1}^{N_C^2-1} \beta_a(x)T_a)]_{ji}$ using the generators T_a and the real function $\beta_a(x)$. The gluon fields transform as

$$[A'_\mu(x)]_{ij} = U(x)_{ik}(A_\mu(x))_{kl}U(x)^{-1}_{lj} + \frac{i}{g}[\partial_\mu U(x)]_{ik}U(x)^{-1}_{kj} . \quad (9)$$

According to the Lagrangian \mathcal{L}_{QCD} three fundamental interactions occur:

- the interaction of **quarks with gluons** corresponding to the term $g\bar{\psi}_\alpha i\gamma^\mu_{\alpha\beta}A_{\mu a}(T_a)_{ij}\psi_\beta$ and to the vertex $\bar{q}gq$.
- the interaction of **three gluons** corresponding to the term $gf_{abc}(\partial_\mu A_{\nu a} - \partial_\nu A_{\mu a})A_{\mu b}A_{\nu c}$ and to the triple-gluon vertex ggg
- the interaction of **four gluons** corresponding to the term $g^2 f_{abc}f_{ade}A_{\mu b}A_{\nu c}A_d^\mu A_e^\nu$ and to the four-gluon vertex $gggg$.

The interactions of quarks with gluons corresponds to the electromagnetic interaction of electrons with photons. The three-gluon and four-gluon self interactions are characteristic for

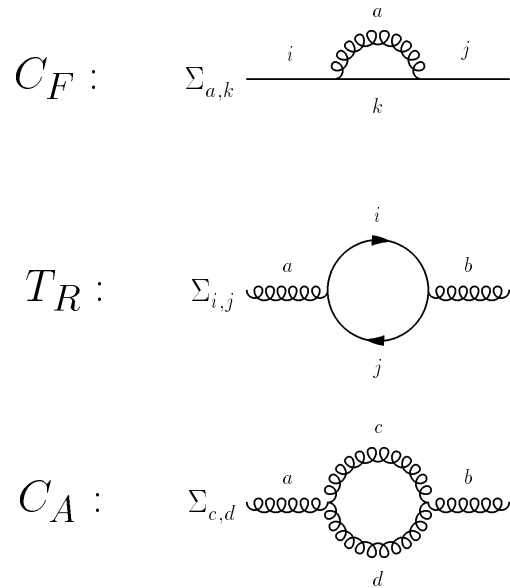


Figure 1: Illustration of the relation of colour factors C_F, T_R, C_A with gluon bremsstrahlung, gluon splitting and the three-gluon interaction.

QCD as a non-abelian field theory and have no analogue in QED. The same coupling g determines the strength of quark-gluon, three-gluon and four-gluon interactions. The four-gluon interaction is proportional to g^2 . The coupling g is independent of the quark flavour and colour.

The relative coupling strengths of gluon bremsstrahlung off a quark, of gluon splitting into quark and antiquark, and of the three-gluon interaction are proportional to the colour factors C_F, T_R and C_A respectively as is illustrated in Figure 1.

1.3 The renormalization group equation

A major obstacle in calculating cross sections perturbatively is the appearance of divergences. Loop diagrams as in Figures 2 (b) and (c) give rise to *ultraviolet* divergences. These correspond to the creation of virtual particles at infinite momenta violating energy conservation. Meaningful calculations are made possible through *regularization* and *renormalization* procedures.

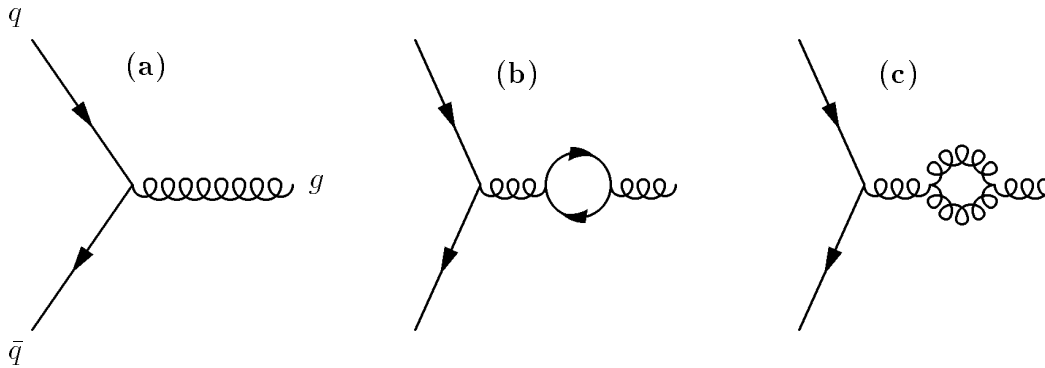


Figure 2: Feynman graphs related to the running of α_s

Regularization means the systematic manipulation of divergent integrals to yield finite expressions. This may be achieved by simply introducing a finite upper integration boundary μ . In practice dimensional regularization, the formal change from $(n = 4)$ -dimensional integrals to those of dimension $n = 4 - 2\epsilon$, is frequently used. The regularized integrals lead to expressions with poles $1/\epsilon$. Renormalization means the systematic subtractions of such terms. It corresponds to the replacement of the bare coupling g related to the vertex $\bar{q}gq$ in Figure 2 (a) by a physical coupling which considers all diagrams of Figure 2. In the $\overline{\text{MS}}$ (modified minimal subtraction) renormalization scheme [15] the terms $1/\epsilon + (\ln 4\pi - \gamma_E)$ are subtracted. (γ_E is Euler's constant.)

Different renormalization schemes may be used but an arbitrary mass parameter μ , the *renormalization scale*, is always introduced. It corresponds to the mass at which the subtractions removing the ultraviolet divergences are performed. The requirement that physical observables must not depend on μ leads to the renormalization group equations [16]. They imply a dependence of the strong coupling α_s on μ which is given by the so-called β -function [9]

$$\mu \frac{\partial \alpha_s(\mu^2)}{\partial \mu} = \beta(\alpha_s) = -\frac{\beta_0}{2\pi} \alpha_s^2(\mu^2) - \frac{\beta_1}{4\pi^2} \alpha_s^3(\mu^2) - \frac{\beta_2}{64\pi^3} \alpha_s^4(\mu^2) + \dots \quad (10)$$

with

$$\beta_0 = 11 - \frac{2}{3} n_f, \quad \beta_1 = 51 - \frac{19}{3} n_f, \quad \beta_2 = 2857 - \frac{5033}{9} n_f + \frac{325}{27} n_f^2, \quad (11)$$

where n_f is the number of quarks of mass less than μ . The coefficients β_0 and β_1 are independent of the renormalization scheme chosen while β_2 and higher order coefficients depend on it. Here β_2 is quoted in the $\overline{\text{MS}}$ renormalization scheme. The β_i are known up to β_3 [17].

The solution of (11) in leading order, that is including only the β_0 term, is

$$\alpha_s(\mu^2) = \frac{\alpha_s(\mu_0^2)}{1 + \frac{\beta_0}{4\pi} \alpha_s(\mu_0^2) \ln(\mu^2/\mu_0^2)}. \quad (12)$$

Once α_s is known at a given reference scale, for example at $\mu_0 = M_Z$, (12) predicts its value at any other (large) scale μ^2 . For $\mu^2 \rightarrow \infty$, $\alpha_s(\mu^2)$ decreases to zero. This property, called *asymptotic freedom*, is one of the major characteristics of QCD and was noticed when the first calculation of β_0 became available in 1973. It makes possible successful perturbative calculations at sufficiently high values of μ^2 . In contrast α_s becomes large for small values of μ^2 . This leads to the *confinement* of quarks into hadrons and explains why coloured quarks are not observed directly.

In practice a dimensionful parameter Λ is frequently used to express the functional form of $\alpha_s(\mu^2)$ or to specify the value of α_s without the need to refer to a scale. Λ is defined by

$$\ln \frac{\mu_0^2}{\Lambda^2} = \int_{\alpha_s(\mu_0)}^{\infty} \frac{dx}{\beta(x)} = \left[\frac{4\pi}{\beta_0 \alpha_s(\mu_0^2)} + \dots \right] + C \quad (13)$$

in leading order where ‘...’ stands for higher order terms. The constant C is arbitrary. Choosing $C = (\frac{\beta_1}{2\beta_0}) \ln(\beta_0/4)$ [15, 18], $\alpha_s(\mu^2)$ as a function of Λ is given in NNLO by [19]

$$\alpha_s(\mu^2) = \frac{4\pi}{[\beta_0 \ln(\mu^2/\Lambda^2)]} - \frac{8\pi\beta_1 \ln[\ln(\mu^2/\Lambda^2)]}{\beta_0 [\beta_0 \ln(\mu^2/\Lambda^2)]^2} + \frac{64\pi}{[\beta_0 \ln(\mu^2/\Lambda^2)]^3} \times \left[\frac{\beta_1^2}{4\beta_0^2} \{ \ln^2[\ln(\mu^2/\Lambda^2)] - \ln[\ln(\mu^2/\Lambda^2)] - 1 \} + \frac{\beta_2}{32\beta_0} \right]. \quad (14)$$

The four-loop expression for α_s can be found in [20].

The relation of Λ and β_i implies that Λ depends on the renormalization scheme. Λ also depends on the number of active flavours n_f . Requiring that $\alpha_s(\mu^2)$ is a continuous function if μ^2 equals a quark mass threshold, a relation of $\Lambda^{(n_f)}$ at different n_f can be derived [21, 22, 20]. In LO [19]

$$\beta_0^{n_f-1} \ln \left(\frac{\Lambda^{(n_f)}}{\Lambda^{(n_f-1)}} \right)^2 = (\beta_0^{n_f} - \beta_0^{n_f-1}) \ln \left(\frac{M_Q}{\Lambda^{(n_f)}} \right)^2 + 2 \left(\frac{\beta_1^{n_f}}{\beta_0^{n_f}} - \frac{\beta_1^{n_f-1}}{\beta_0^{n_f-1}} \right) \times \ln \left[\ln \left(\frac{M_Q}{\Lambda^{(n_f)}} \right)^2 \right] - 2 \frac{\beta_1^{n_f-1}}{\beta_0^{n_f-1}} \ln \frac{\beta_0^{n_f}}{\beta_0^{n_f-1}}. \quad (15)$$

Note that equation (15) depends on the running quark mass M_Q [14] that defines the flavour threshold.

One consequence of the relation of α_s and Λ is the much increased relative uncertainty on Λ compared with that of α_s . Thus $\alpha_s(M_Z) = 0.119 \pm 0.003$ translates into $\Lambda_{\overline{MS}}^{(5)} = 220_{-35}^{+40}$ MeV (using (14)).

The running of α_s is shown in Figure 3. The corresponding scale dependence of α , the fine structure constant, is also shown. Besides being much smaller than α_s , α increases with μ_R . This fundamental difference between α and α_s is introduced through the presence of boson self-interactions as in diagram 2 (c), which are absent in QED.

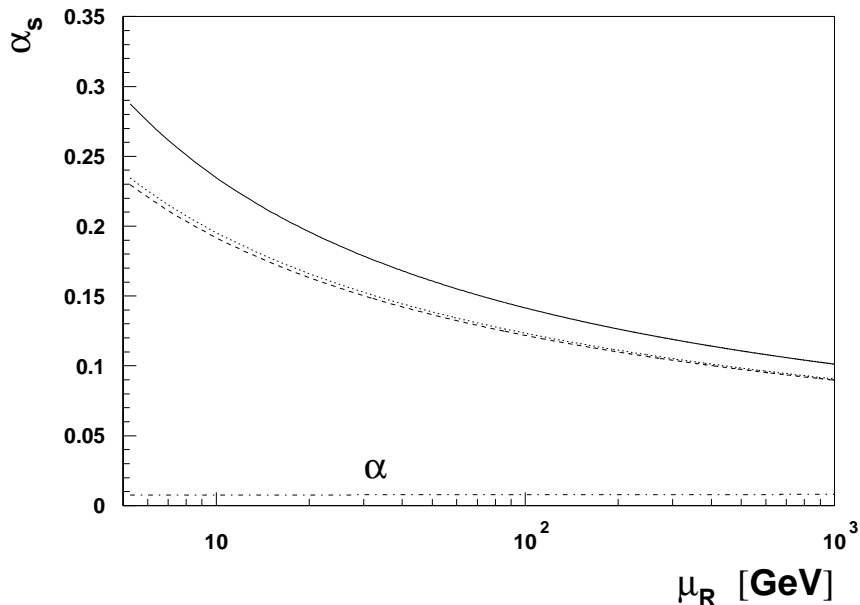


Figure 3: Running of α_s in leading order (full line), NLO (dashed line) and NNLO (dotted line). The running of α is also shown (dashed-dotted line).

1.4 Deep-inelastic scattering

Deep-inelastic scattering of leptons off nucleons corresponds in the Quark-Parton Model (QPM) to the elastic interaction of a virtual boson with a free quark in the nucleon (see Figure 4). The interaction can be expressed as the sum of incoherent scatterings from point-like partons, the quarks, which are free inside the proton on the time scale of $\approx 1/\sqrt{Q^2}$ of the scattering process. The QPM corresponds to the zeroth order approximation of QCD. Neutral current (NC) ep interactions $ep \rightarrow eX$ are mediated through exchange of a photon or a Z^0 boson. Charged current (CC) ep interactions $ep \rightarrow \nu X$ are mediated through exchange of W^\pm bosons.

Kinematic variables

The kinematics of the scattering process at a given centre-of-mass energy are determined through

knowledge of two independent variables such as the polar angle and the energy of the scattered lepton. Usually cross sections are given as a function of two of the Lorentz invariant quantities Q^2 , x and y :

$$Q^2 = -(q)^2 = -(k - k')^2, \quad x = \frac{Q^2}{2P \cdot q}, \quad y = \frac{P \cdot q}{P \cdot k}, \quad (16)$$

where k and k' are the four-momenta of the incoming and scattered lepton, and P is the four-momentum of the incoming proton.

The virtuality Q^2 corresponds to the negative square of the virtual boson's four-momentum. The Bjorken scaling variable x is interpreted in the QPM as the fraction of the proton momentum carried by the struck quark in the proton infinite-momentum frame. The inelasticity y measures the fractional energy transferred to the hadronic system in the proton rest frame. Both x and y range from 0 to 1. They are related to Q^2 through

$$Q^2 = sxy \quad (17)$$

where $s = (k + P)^2 \approx 4E_e E_p$ is the centre-of-mass energy squared. E_e and E_p are the energies of the incoming electron and proton respectively. (Here and in the following equations the masses of the proton and the lepton are always neglected.)

The invariant mass of the hadronic final state W is given by

$$W^2 = (q + P)^2 \approx Q^2 \frac{1-x}{x}. \quad (18)$$

Lepton-nucleon scattering processes with $W^2 \gg m_{\text{Proton}}^2$ are *inelastic*. Those with in addition $Q^2 \gg m_{\text{Proton}}^2$ are called *deep-inelastic*.

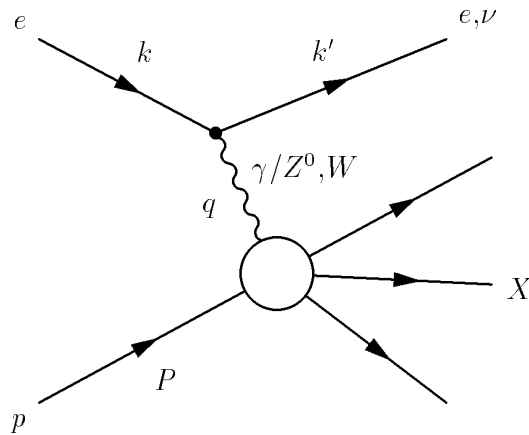


Figure 4: Illustration of deep-inelastic electron-proton scattering.

The range of Q^2 and x covered by the HERA collider experiments extends up to $Q^2 \approx 50,000$ GeV² and down to $x \approx 10^{-5}$. That is more than two orders of magnitude higher in Q^2 and more than two orders of magnitude higher lower in x than fixed target experiments [24, 25, 26, 27].

Structure functions and DIS cross sections

The cross section for deep-inelastic NC processes as a function of x and Q^2 can be expressed as

$$\frac{d^2\sigma_{NC}^{e\pm p}}{dx dQ^2} = \frac{2\pi\alpha^2}{Q^4 x} \left\{ [1 + (1-y)^2] F_2(x, Q^2) - y^2 F_L(x, Q^2) \mp [1 - (1-y)^2] x F_3(x, Q^2) \right\}. \quad (19)$$

The cross section shows the characteristic $1/Q^4$ dependence known from Rutherford scattering. It is proportional to the fine structure constant α^2 due to the exchange of a virtual photon, the dominant contribution at low Q^2 . The *structure functions* F_i parameterize the structure of the proton. The contribution of the longitudinal structure function $F_L (= F_2 - 2xF_1)$ is small except at large values of y . The parity-violating structure function $x F_3$ is small for $Q^2 \ll M_Z^2$ where Z^0 exchange is negligible. In the QPM and for $Q^2 \ll M_Z^2$ the structure function F_2 is given by

$$F_2(x, Q^2) = F_2(x) = x \sum_q e_q^2 [q(x) + \bar{q}(x)] \quad (20)$$

where e_q is the quark charge in units of the charge of the electron. $q(x)$ and $\bar{q}(x)$ are the proton's density of quarks and antiquarks at a given momentum fraction x . Within the QPM the $q(x)$ and $\bar{q}(x)$ and thus F_2 do not depend on Q^2 , and F_L is zero. Including higher order QCD effects like gluon radiation introduces a dependence of the parton densities on Q^2 as is discussed in section 1.5. The parton densities and correspondingly the structure functions can not (yet) be derived within QCD and must be determined from experiment.

At *high* Q^2 , Z^0 exchange and $\gamma - Z^0$ interference terms become important. Then equation (20) needs to be modified and F_3 cannot be neglected any more:

$$F_2(x, Q^2) = x \sum_q [q(x) + \bar{q}(x)] A_q^\pm, \quad x F_3(x, Q^2) = 2x \sum_q [q(x) - \bar{q}(x)] B_q^\pm \quad (21)$$

where

$$\begin{aligned} A_q^\pm &= \left[e_q^2 + 2e_q v_q (-v_e \mp \lambda a_e) P_Z + (v_e^2 + a_e^2 \pm 2\lambda a_e v_e) (v_q^2 + a_q^2) P_Z^2 \right] \\ B_q^\pm &= \left[e_q a_q (\lambda v_e \pm a_e) P_Z + v_q a_q (-\lambda(v_e^2 + a_e^2) \mp 2v_e a_e) P_Z^2 \right]. \end{aligned} \quad (22)$$

The v_f and a_f are the weak vector and axial-vector couplings of a fermion f , here electron e or quark q . They are given by

$$v_f = T_{3f} - 2e_f \sin^2 \theta_W, \quad a_f = T_{3f} \quad (23)$$

where θ_W is the Weinberg angle and e_f and T_{3f} are the electric charge and the third component of the weak isospin² respectively. λ denotes the electron beam polarization where $\lambda = +1, -1, 0$ correspond to right-handed, left-handed and unpolarized lepton beams respectively. The term P_Z is related to the ratio of the Z^0 and the γ propagators

$$P_Z = \frac{Q^2}{Q^2 + M_Z^2} \frac{1}{\sin^2 2\theta_W}. \quad (24)$$

The cross section for CC processes in the QPM is given by

$$\frac{d^2 \sigma_{CC}^{ep}}{dx dQ^2} = \frac{G_F^2}{\pi} \left(\frac{M_W^2}{M_W^2 + Q^2} \right)^2 \begin{cases} u + c + t + (1-y)^2(\bar{d} + \bar{s} + \bar{b}) & \text{for } e_L^- \\ \bar{u} + \bar{c} + \bar{t} + (1-y)^2(d + s + b) & \text{for } e_R^+ \\ 0 & \text{for } e_R^-, e_L^+ \end{cases} \quad (25)$$

The CC cross section is much smaller than the NC cross section for $Q^2 \ll M_W^2$ as can be seen using the relation $G_F = \pi\alpha/\sqrt{2}\sin^2\theta_W M_W^2$. NC and CC cross sections start to be of similar magnitude when Q^2 approaches M_W^2 as is shown in Figure 5. (Note that in the kinematic range of HERA the bottom and top quark do not contribute.)

1.5 Parton evolution equations

The simple picture of F_2 and parton density functions obtained in the QPM is modified when QCD corrections are considered. Initial-state gluon radiation may reduce the momentum fraction of the quark seen by the virtual photon. Similarly the scattered quark may have been created

² $T_3 = +1/2$ for u, e^+, ν and $-1/2$ for $d, e^-, \bar{\nu}$.

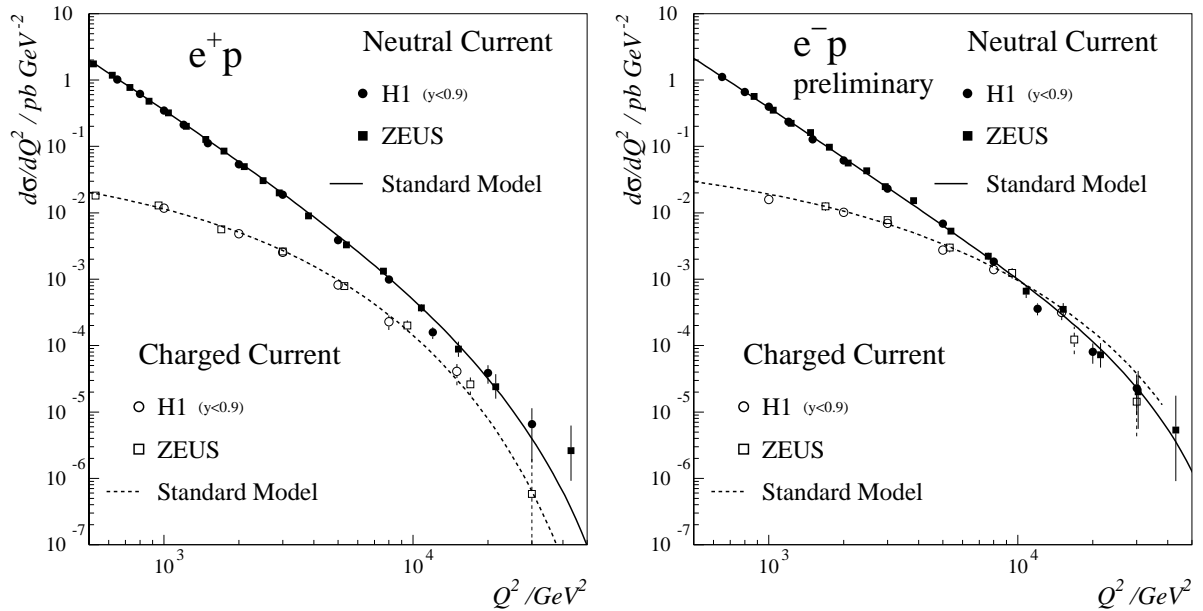


Figure 5: NC and CC differential cross sections $d\sigma/dQ^2$ for e^+p and e^-p DIS as measured by H1 [28, 29] and ZEUS [30, 31].

through quark-antiquark splitting of a gluon. The corresponding QCD-Compton and boson-gluon-fusion diagrams are shown in Figure 6. These diagrams introduce initial-state collinear divergences which are regulated and absorbed into the parton densities in order to get a finite result. This procedure introduces a dependence of the parton densities on the *factorization scale* μ_F similarly to the way the absorption of ultraviolet divergences leads to the *renormalization scale* dependence of the strong coupling. The dependence of the parton densities on the factorization scale is given by the parton evolution equations.

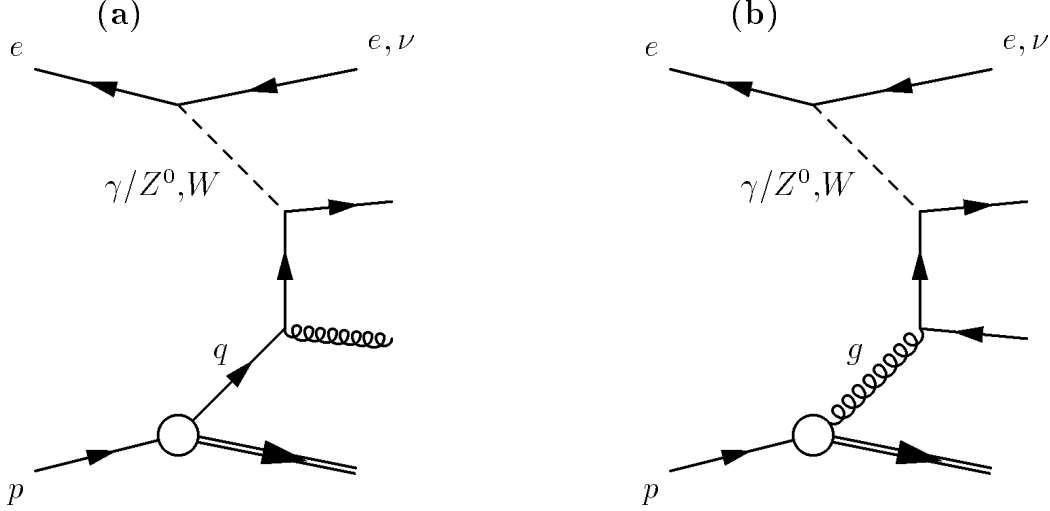


Figure 6: Feynman graphs contributing to DIS in $O(\alpha_s)$: QCD-Compton scattering (a) and boson-gluon-fusion (b).

DGLAP equations

The Dokshitzer-Gribov-Lipatov-Altarelli-Parisi (**DGLAP**) [32] parton evolution equations describe the dependence of the parton densities on the factorization scale μ_F^2 which is chosen to be Q^2 in the following equations

$$\begin{aligned} \frac{dq_i(x, Q^2)}{d \ln Q^2} &= \frac{\alpha_s(Q^2)}{2\pi} \int_x^1 \frac{d\xi}{\xi} \left[P_{qq}\left(\frac{x}{\xi}\right) q_i(\xi, Q^2) + P_{qg}\left(\frac{x}{\xi}\right) g(\xi, Q^2) \right] \\ \frac{dg(x, Q^2)}{d \ln Q^2} &= \frac{\alpha_s(Q^2)}{2\pi} \int_x^1 \sum_i \frac{d\xi}{\xi} \left[P_{gq}\left(\frac{x}{\xi}\right) q_i(\xi, Q^2) + P_{gg}\left(\frac{x}{\xi}\right) g(\xi, Q^2) \right]. \end{aligned} \quad (26)$$

The index i denotes the quark flavour. The *splitting functions* $P_{qq}(z)$, $P_{qg}(z)$, $P_{gg}(z)$, $P_{gq}(z)$ are calculable perturbatively and are given in LO by:

$$\begin{aligned} P_{qq}(z) &= C_F \frac{1+z^2}{1-z}, \quad P_{qg}(z) = T_R [z^2 + (1-z)^2] \\ P_{gg}(z) &= 2C_A \left(\frac{z}{1-z} + \frac{1-z}{z} + z(1-z) \right), \quad P_{gq}(z) = C_F \frac{1+(1-z)^2}{z} \end{aligned} \quad (27)$$

In leading order the $P_{ba}(z)$ are related to the probability of the parton of type a splitting into partons b and c carrying momentum fractions of z and $(1-z)$ respectively. They are valid for

small angle (collinear) emissions. The divergences $1/z$ or $1/(1-z)$ are characteristic for gluon emission. They are absent in P_{qg} which corresponds to the splitting of $g \rightarrow q\bar{q}$. The P_{qq} and P_{gq} correspond to the vertex $q \rightarrow qg$ with the gluon or the quark carrying momentum fraction z (see Figure 7). The colour factors C_F , T_R and C_A were introduced in section 1.1.

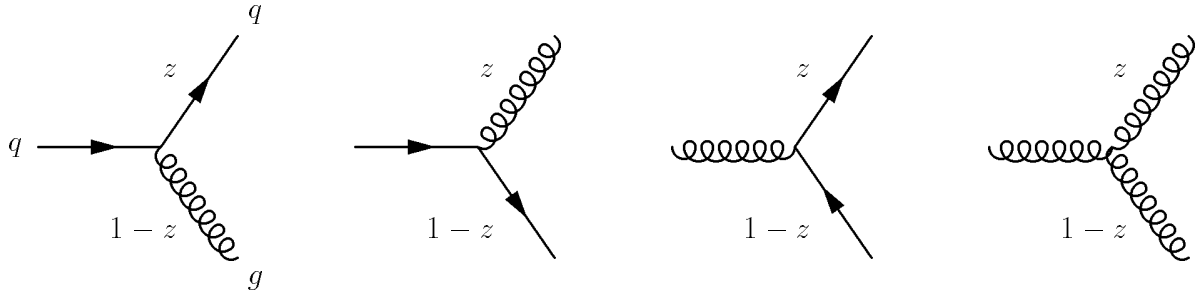


Figure 7: Vertices corresponding to the splitting functions P_{qq} , P_{gq} , P_{qg} and P_{gg} (from left to right).

The DGLAP equations are valid in the phase space region where the gluons have strongly ordered transverse momenta

$$Q^2 \gg k_{T_n}^2 \gg \dots \gg k_{T_1}^2 . \quad (28)$$

The longitudinal momenta are ordered due to momentum conservation

$$x < x_{n-1} < \dots < x_1 . \quad (29)$$

The DGLAP equations correspond to the sum of ladder diagrams (in an axial gauge) with multigluon emissions (see Figure 8). Each emission gives rise to terms proportional to $\alpha_s \int dk_T^2/k_T^2$ due to the propagator. The resulting nesting integrations give

$$\int^{Q^2} \frac{dk_{T_n}^2}{k_{T_n}^2} \dots \int^{k_{T_3}^2} \frac{dk_{T_2}^2}{k_{T_2}^2} \int^{k_{T_2}^2} \frac{dk_{T_1}^2}{k_{T_1}^2} \sim \frac{[\ln Q^2]^n}{n!} . \quad (30)$$

Thus effectively the DGLAP equations sum terms $[\alpha_s \ln Q^2]^n$ where each additional emission gives an extra power of $\ln Q^2$.

The asymptotic behaviour of the gluon density in the region low x and large Q^2 can be derived from the DGLAP equations in the double-leading-logarithm approximation **DLA**. At low x the splitting function $P_{gg} \approx 2C_A \frac{1}{z}$ dominates such that the gluon density is much larger than the quark densities. Equation (26) thus reduces to

$$\frac{dg(x, Q^2)}{d \ln Q^2} = \frac{\alpha_s(Q^2)}{2\pi} \int_x^1 \frac{d\xi}{\xi} P_{gg}\left(\frac{x}{\xi}\right) g(\xi, Q^2) . \quad (31)$$

Multigluon emissions with $Q^2 \gg k_{T_n}^2 \gg \dots \gg k_{T_1}^2$ and $x \ll x_{n-1} \ll \dots x_1$ lead to factors of $[\ln Q^2]^n/n!$ as above combined with terms $\ln(1/x)$ from the nested integrations

$$\int_x^1 \frac{dx_{n-1}}{x_{n-1}} \dots \int_{x_2}^1 \frac{dx_1}{x_1} \int_{x_1}^1 \frac{d\xi}{\xi} g(\xi, Q_0^2) \sim \frac{1}{n!} \left(\ln \frac{1}{x} \right)^n . \quad (32)$$

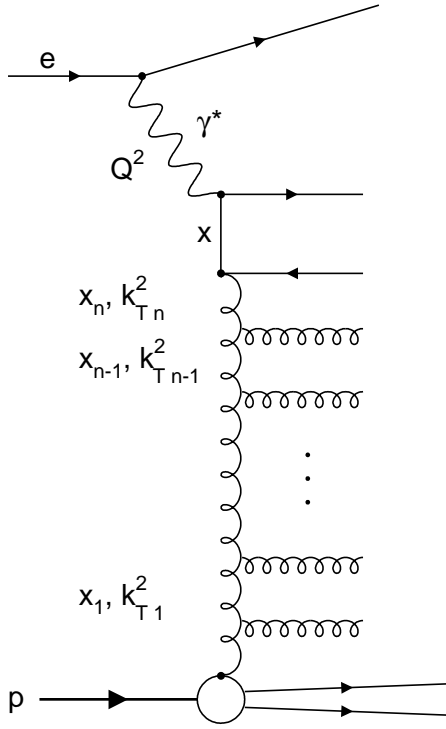


Figure 8: Ladder diagram to illustrate parton evolution.

Thus in the DLLA the leading powers of $[\alpha_s \ln(1/x) \ln Q^2]^n$ are summed. At small values of x the terms $\ln(1/x)$ become large. The DLLA thus provides a quantitative prediction of the rise of F_2 at small values of x [33].

BFKL equations

At small values of x terms proportional to $\alpha_s \ln(1/x)$ are also important. These terms are summed over within the Balitsky-Fadin-Kuraev-Lipatov (**BFKL**) equation [34] assuming strong ordering of the longitudinal momenta of the emitted partons $x \ll x_{n-1} \ll \dots x_1$. No assumption on the transverse momenta k_T is made. The BFKL equation is formulated in terms of the unintegrated gluon density $f(x, k_T^2)$ which relates to the familiar gluon density $g(x, Q^2)$ used above via

$$xg(x, Q^2) = \int^{Q^2} \frac{dk_T^2}{k_T^2} f(x, k_T^2). \quad (33)$$

The x dependence of the unintegrated gluon density is predicted to be

$$\frac{df(x, k_T^2)}{d \ln 1/x} = \int dk_T'^2 K(k_T, k_T') f(x', k_T'^2) \quad (34)$$

at small x and not too large Q^2 [34].

In LO and for fixed α_s equation (34) can be solved analytically which leads to the characteristic small x behaviour proportional to $x^{-\lambda}$ where $\lambda \approx 1/2$. Unfortunately NLO calculations have yielded large corrections to λ [35]. In [36] it is argued that the reliability of the BFKL

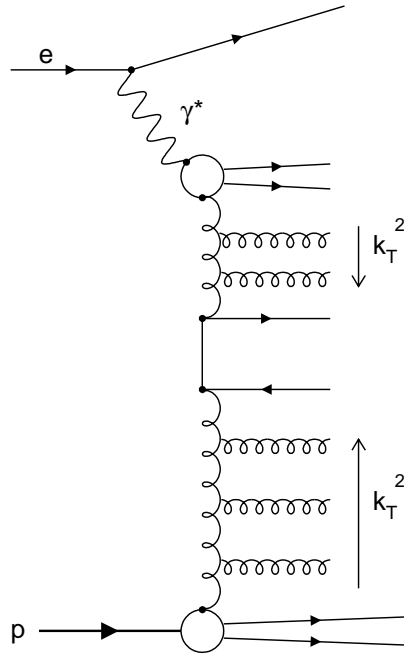


Figure 9: Diagram illustrating the effect of unordered k_T introduced through a resolved photon.

predictions can be improved by imposing a *consistency* (or kinematic) *constraint* which makes possible the resummation of subleading $\ln(1/x)$ terms. The consistency constraint effectively ensures energy-momentum conservation in a large phase space region. Predictions for forward π and jet cross sections based on the leading-order BFKL equations in conjunction with the consistency constraint have been calculated [37] and are compared with measurements in section 5.

CCFM equations

The Ciafaloni-Catani-Fiorani-Marchesini (CCFM) equation [38] is a modified parton evolution equation based on gluon emission with angular ordering. It reproduces the results of DGLAP evolution at large x and of BFKL at small x .

1.6 Structure of the virtual photon

In DIS the virtual photon is usually assumed to be pointlike. As in photoproduction the photon can, however, fluctuate into a $q\bar{q}$ pair or (at low Q^2) into a vector meson carrying the quantum numbers of the photon. These quantum fluctuations are expected to be strongly suppressed with increasing Q^2 but may be resolved by an interaction with an energetic parton of the proton when $E_{T\text{ parton}}^2 \gg Q^2$. The parton acts as a probe of *photon structure* similarly to the way the pointlike virtual photon resolves the partonic structure of the proton.

The interaction of a *resolved* photon with a parton of the proton are illustrated in Figure 9. The concept of virtual photon structure leads to photon density functions and corresponding parton evolution equations. Parton ladders ordered in k_T from both the photon and the proton to the hard scattering process effectively lead to a parton cascade that is unordered.

1.7 Fit of parton density functions

The standard procedure to determine parton density functions from structure function and related measurements consists of the following steps:

- The x dependence of the parton densities f_i is parameterized at a given starting scale Q_0^2 . Typical parameterizations are of the form

$$A_i x^{-\lambda_i} (1-x)^{\beta_i} (1 + \gamma_i \sqrt{x} + \delta_i x), \quad (35)$$

where the A_i , λ_i , β_i , γ_i , δ_i with $i = u, d, \dots, g$ are free parameters to be determined. The starting scale Q_0^2 is mostly chosen to be a few GeV^2 in order to be large enough for perturbative QCD to be applicable.

- The $f_i(x, Q_0)$ are numerically evolved to values of Q^2 where DIS data exist, using the DGLAP equations with the NLO splitting functions.
- the predicted values of structure functions (or other observables) are calculated from the $f_i(x, Q)$ and the χ^2 of the predictions and the corresponding measurements is determined.

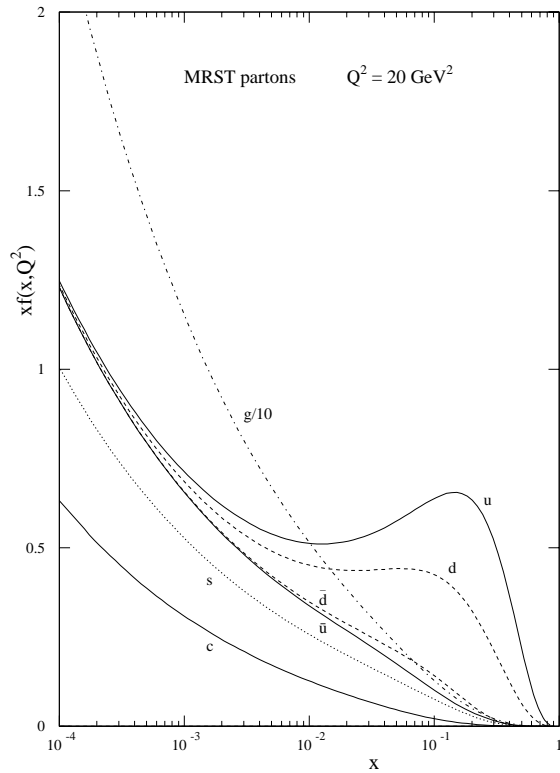


Figure 10: Example of parton density functions taken from MRST [42].

Iteration of these steps allows the determination of the initial parameters A_i , λ_i , β_i , γ_i , δ_i and thus of the parton densities in multi-dimensional fits. The number of parameters to be determined is not small. In a recent H1 fit, for example, 13 free parameters were determined [28].

This requires precise measurements in a large kinematic range and in practice a combination of data from different scattering processes and experiments. Global fits to the world data are regularly provided by the groups CTEQ, GRV and MRST. They include data from DIS experiments with muon and neutrino beams, Drell-Yan production $pN \rightarrow \mu^+ \mu^- X$, from $pp \rightarrow \gamma X$, the W asymmetry and inclusive jet production at large $E_{T,jet}$ in $p\bar{p}$ collisions and, of course, from $e\bar{p}$ collisions at HERA. For a detailed description of these fits see [39, 40, 41].

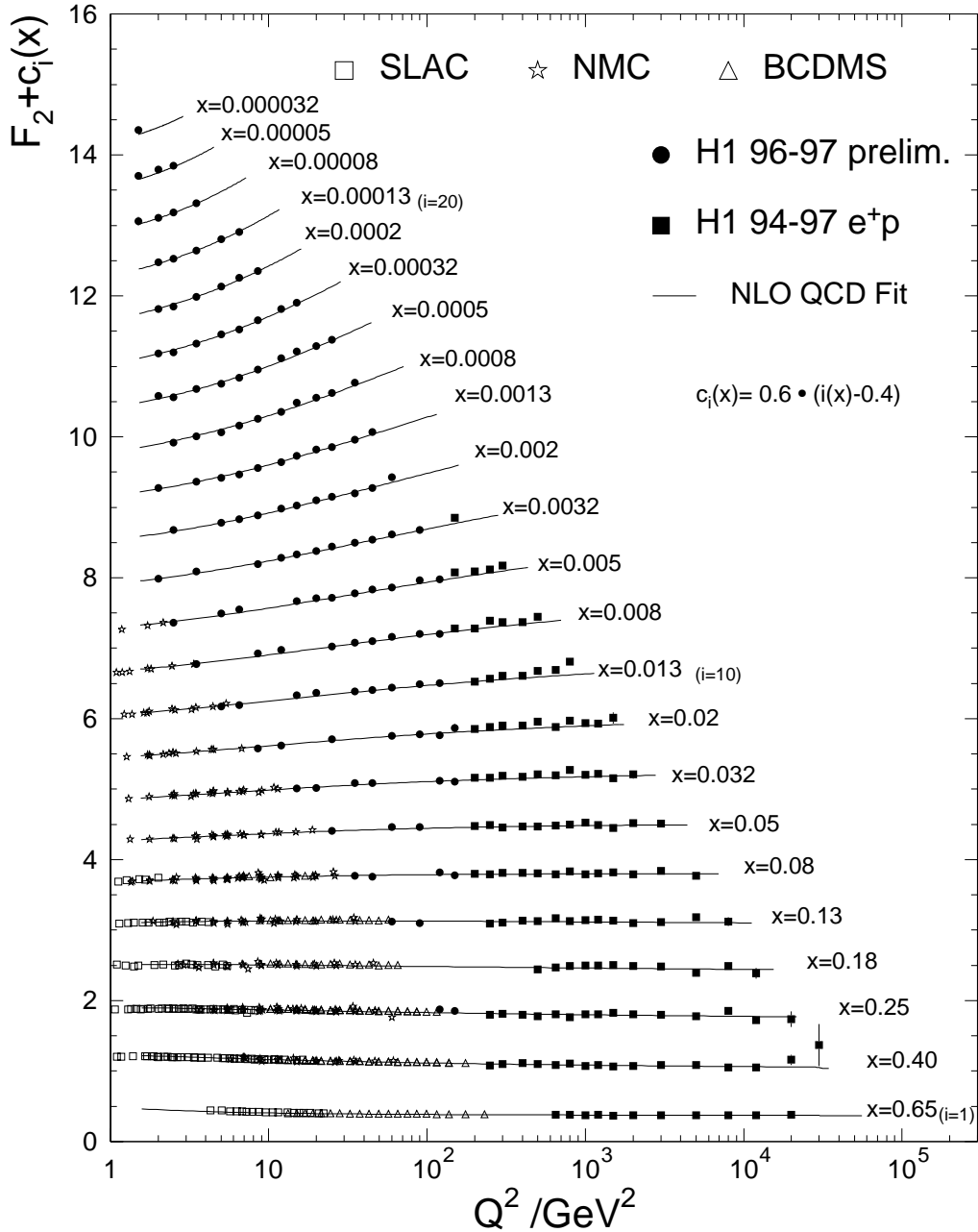


Figure 11: Overview of F_2 measurements of H1 [43, 28] and fixed target experiments [24, 25, 27] and comparison with perturbative QCD predictions in NLO [28].

Parton density functions at $Q^2 = 20 \text{ GeV}^2$ as determined by MRST are shown in Figure 10 for illustration. The most characteristic features are the peak of the u and d quark densities close to $x \approx 1/3$ corresponding to the valence quark region. The shift with respect to $x = 1/3$ is due to gluon bremsstrahlung. The gluon density at low x is much larger than the quark densities. Its rise is driven by the dominant triple gluon vertex $g \rightarrow gg$ leading to efficient gluon multiplication. The gluons at low x drive the rise of the quark and antiquark (sea quark) densities produced via $g \rightarrow q\bar{q}$.

Measurements of the structure function F_2 at HERA in the approximate range of $1 < Q^2 < 30,000 \text{ GeV}^2$ and $10^{-5} < x < 0.65$ are fully compatible with NLO QCD fits based on the DGLAP equations as is shown in Figure 11.

1.8 Di-parton cross sections

Dijet production in DIS proceeds in $O(\alpha_s)$ through the **QCD-Compton** (QCDC) process $eq \rightarrow eqg$ and **Boson-Gluon-Fusion** (BGF) $eg \rightarrow eq\bar{q}$ as shown in Figure 6. The differential di-parton cross section depends on five independent kinematic variables. Besides x and Q^2 (or y) the three additional variables z , x_p and ϕ are frequently used [44]. The variable x_p is defined by

$$x_p = \frac{Q^2}{2p \cdot q} = \frac{Q^2}{Q^2 + m_{12}^2} = \frac{x}{\xi} \quad (36)$$

where q is the four-momentum of the virtual boson and p that of the incoming parton. The p_i , $i = 1, 2$ are the four-momenta of the two outgoing partons from the hard scattering process and m_{12} is their invariant mass. The variable ξ corresponds to the fraction of the proton's four-momentum P carried by the incoming parton with momentum $p = \xi P$. The variable z can be defined for either parton i by

$$z_i = \frac{p \cdot p_i}{p \cdot q} = \frac{1}{2} (1 - \cos \theta_i^*) \quad (37)$$

where θ_i^* is the scattering angle of the parton i in the centre-of mass system of virtual boson and incoming parton. The z_i are related by $z_1 + z_2 = 1$. ϕ is the (azimuthal) angle between the planes spanned by the incoming and outgoing lepton and by the outgoing partons in the hadronic centre-of-mass system.

The complete di-parton cross sections for NC and CC DIS in $O(\alpha_s)$ are given explicitly in [44]. The dominant contribution to QCD-Compton scattering is proportional to

$$d\sigma_{QCDC} \sim \frac{1 + x_p^2 z^2}{(1 - z_q)(1 - x_p)}, \quad (38)$$

where z_q stands for the value of z associated with the scattered quark. The QCD-Compton cross section diverges if $z_q \rightarrow 1$ or $x_p \rightarrow 1$. This corresponds to radiation of a soft gluon ($z_q, x_p \rightarrow 1$) or of a gluon collinear to the incoming quark ($z_q \rightarrow 1$) or outgoing quark ($x_p \rightarrow 1$).

The dominant contribution to boson-gluon-fusion is proportional to

$$\sigma_{BGF} \sim \frac{[z^2 + (1 - z)^2][x_p^2 + (1 - x_p)^2]}{z(1 - z)}. \quad (39)$$

It diverges if one of the quarks is collinear to the incoming gluon or if one of the quarks is soft. Note that this term is symmetric in z_i in contrast to the QCD-Compton cross section.

In order to use the above formulae for meaningful comparisons with measurements an infrared safe observable, e.g. a jet cross section, must be defined and the parton cross sections must be convoluted with the corresponding parton density functions $f_i(\xi, \mu_F^2)$. Perturbative calculations for specific observables in NLO and the corresponding NLO programs are discussed in section 2.

1.9 Parton showers and the colour dipole model

Perturbative calculations at fixed order of α_s cannot be expected to describe all regions of phase space adequately. Higher-order collinear emissions leading to enhanced contributions (logarithms) in the perturbative series may be sizeable even when suppressed by additional powers of α_s . In order to describe observables sensitive to multiple parton emissions such as inclusive particle distributions, jet multiplicities at small jet separation, width and substructure of jets etc. it is important to consider the dominant terms in all orders of α_s . This is achieved by **parton showers** [45] which can conveniently be implemented in Monte Carlo programs.

Parton showers consist of successive branchings $a \rightarrow bc$ originating from an initial quark or gluon a . As discussed above, each branching is characterized by the momentum fraction that is transferred from the original parton a to b and c and by the virtuality t of a before the branching. The branching probability is given by

$$\sigma \sim \frac{dt}{t} dz \frac{\alpha_s}{2\pi} P_{ba}(z) \quad (40)$$

where P_{ba} are the splitting functions introduced earlier.

In *initial-state* parton showers a parton with small virtuality evolves to increasingly larger negative virtualities ($t < 0$) by emitting partons which are either real or timelike ($m^2 > 0$). Finally a spacelike quark is produced which interacts with the virtual boson. The outgoing quark is again on mass-shell or timelike.

Any radiated parton with timelike virtuality can be the starting point of a *final-state* (timelike) parton shower. In this case the virtuality of the original parton is reduced with each branching until a minimum value Q_0 is reached where the parton evolution is stopped. In Monte Carlo models hadronization is performed at this stage.

The variable t may be seen as evolution ‘time’. The probability that parton i at t_0 has *not* split up to t is given by the *Sudakov form factor*

$$\Delta_i(t) = \exp \left[- \sum_j \int_{t_0}^t \frac{dt'}{t'} \int dz \frac{\alpha_s}{2\pi} P_{ji}(z) \right]. \quad (41)$$

Based on equations (40) and (41) the parton shower can be simulated with Monte Carlo methods. In practice initial-state parton showers are evolved *backward* from the hard scattering to the incoming parton. This avoids rejection of events when after shower evolution the

kinematics do not allow the hard scattering process to be generated. The probability to evolve backwards is given by a modified form factor which includes parton density functions $f(z, t)$ when choosing the next branching point t .

The effect of soft gluon emissions is considered by angular ordering of successive gluon emissions. This feature is due to the destructive interference of soft gluons emitted at angles larger than the opening angles of the previous emission. Parton showers with angular ordering are called *coherent*.

An alternative description to parton showers is provided by the **colour dipole model** (CDM) [46]. In the CDM a $q\bar{q}$ produced in e^+e^- annihilation is treated as an antenna consisting of a colour dipole emitting gluon radiation. New dipoles are formed from the qg and $\bar{q}g$ which independently radiate further gluons. Dipoles can also be formed between gg pairs. This procedure automatically includes coherence effects.

In DIS the first dipole is formed between the struck quark and the proton remnant. Unlike quark and gluons the proton remnant is not pointlike. Emissions of small wavelengths from an extended antenna are suppressed. Similarly colour dipole radiation in the region of the proton remnant is suppressed in the CDM. The struck quark is also treated as an extended object since the virtual photon only resolves the struck quark with a resolution proportional to $1/Q$. The detailed features of the suppression are determined by model parameters.

The CDM does not distinguish between initial and final state radiation. The transverse momenta of gluons ordered in rapidity (corresponding to x_i) are unordered, similarly to the situation in BFKL evolution.

1.10 Hadronization models

Hadronization is a non-perturbative process which is not yet understood at a fundamental level. Phenomenological hadronization models have been constructed in order to relate perturbative QCD predictions for partons to the hadronic distributions measured by experiments.

The most important hadronization models are the *string model* [47] and the *cluster model* [48]. They provide the full hadronic final state given an initial partonic configuration.

String model

The colour flux between a quark q and antiquark \bar{q} is represented by a relativistic string of constant energy density per unit length. With increasing $q\bar{q}$ separation the string's potential energy increases. The string finally breaks into new string pieces by creating $q\bar{q}$ pairs from the vacuum in a tunnelling process provided the string energy becomes large enough. Gluons are represented by 'kinks' of the strings between $q\bar{q}$ pairs. Mesons are formed when no energy is left to produce further $q\bar{q}$ pairs. The energy fraction of hadrons is distributed according to fragmentation functions. The transverse momentum of hadrons is distributed according to a Gaussian. The form of the fragmentation function and the width of the Gaussian are given by parameters that are determined by comparison with measurements. Further parameters of the string model are related to the fraction of strange quark pairs produced and to the fraction of diquarks, needed for baryon production.

In DIS strings are stretched between the proton remnant and the scattered partons. The string configurations differ for scattering off valence and sea quarks, for QCD-Compton and boson-gluon-fusion.

Cluster model

In the cluster model the gluons originating from the perturbative parton evolution are split non-perturbatively into $q\bar{q}$ pairs. Neighbouring quarks are then combined to form colour singlets. Low mass clusters are allowed to decay isotropically into pairs of hadrons. The branching ratios are determined by the density of meson states with the appropriate quantum numbers. High mass clusters are split into clusters of smaller mass. An attractive feature of the cluster model is its small number of parameters.

Both models are based on the general principles of *local parton-hadron duality* [49] and *preconfinement* [50].

- *Local parton-hadron duality*: As a long-distance process involving only small momentum transfers hadronization is not expected to change the quantum numbers and momenta of partons substantially. Partons are thus converted into hadrons *locally* in phase space.
- *Preconfinement*: The confinement of partons is local in colour and is independent of the hard scattering scale Q . This is expected from the corresponding properties of perturbative QCD radiation.

Other approaches to hadronization invoke application of *power corrections* or use of *fragmentation functions*:

- *Power corrections*: Hadronization corrections are expected to decrease with increasing size of the hard scattering scale Q . Power corrections proportional to $1/Q^p$ can be calculated for distributions (or their mean values) of given observables. This approach is discussed in detail in section 3.
- *Fragmentation functions*: Fragmentation functions $D_i^h(z, Q)$ parameterize the probability of a parton i to fragment into a hadron h with momentum fraction z . Fragmentation functions have large similarities with parton density functions. They cannot be calculated perturbatively but are universal and their dependence on the scattering scale Q is given by the DGLAP evolution equations. Investigations of fragmentation functions at HERA are discussed in section 6.

1.11 Reference frames, jet algorithms and event shape observables

1.11.1 Reference frames

Analyses of the hadronic final state in DIS can be performed in different reference frames. The most common choices are the *laboratory frame*, the *hadronic centre-of-mass frame* and the *Breit frame*. Their definition and characteristics are briefly introduced below.

Laboratory frame

In the laboratory frame the relation of experimental observables with detector components is most direct. This has the advantage that acceptance and resolution effects may more easily be understood. A disadvantage for QCD studies is the correlation of the scattered lepton with the hadronic final state through momentum conservation.

Hadronic centre-of-mass frame

In the hadronic centre-of-mass frame the momenta \mathbf{q} and \mathbf{p} of the virtual boson and the incoming proton, respectively, satisfy the relation $\mathbf{p} + \mathbf{q} = \mathbf{0}$. Conventionally the proton direction is defined as the z axis with positive z corresponding to the proton direction. In the QPM the four-momentum of the scattered quark after absorption of the virtual boson is $xp + q$. The scattered quark is collinear with the boson and, correspondingly, its transverse energy E_T is zero. Higher order QCD radiation can lead to partons with $E_T > 0$. The direct interpretation of particles or jets with large E_T as a signal for QCD radiation is one of the main advantages of QCD analyses in the hadronic centre-of-mass frame. The Lorentz transformation of the reconstructed particles to the hadronic centre-of-mass frame relies on the measurement of \mathbf{q} e.g. via the reconstruction of the scattered lepton. The experimental error of the kinematic reconstruction thus introduces a corresponding uncertainty in the boosted particle momenta.

Breit frame

The Breit frame and the hadronic centre-of-mass frame are related through a longitudinal boost. In the Breit frame $2x\mathbf{p} + \mathbf{q} = \mathbf{0}$. The virtual boson is purely space-like and its four-momentum q is $\{0, 0, 0, -Q\}$. In the QPM the initial quark (as seen in the Breit frame) has longitudinal momentum $Q/2$ and is back-scattered with momentum $-Q/2$. As in the hadronic centre-of-mass frame the presence of partons/jets with significant transverse momentum is indicative of QCD radiation (see Figure 12).

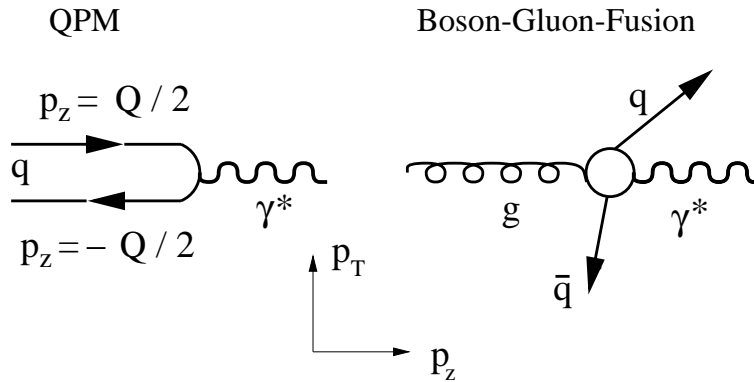


Figure 12: Illustration of the scattering process as seen in the Breit frame for quark scattering in the QPM and boson-gluon-fusion.

The direction of the proton defines the *target hemisphere* ($p_z > 0$), that of the struck quark defines the *current hemisphere* ($p_z < 0$). In the QPM the current hemisphere in the Breit

frame corresponds to one hemisphere of a $q\bar{q}$ event in e^+e^- annihilation. The Breit frame offers maximum separation between the proton remnant and the struck quark which makes it particularly suited for comparisons of jet fragmentation in DIS and e^+e^- .

1.11.2 Jet algorithms

Jet algorithms have become a powerful tool in high energy physics. The observation of collimated jets of hadrons provides one of the most suggestive confirmations of the presence of quarks and gluons as the elementary particles of QCD. Measurement of jet related observables has made possible many quantitative tests of perturbative QCD predictions.

Various jet algorithms have been used in DIS at HERA. They may be characterized by:

- the *reference frame* in which the jet algorithm is applied;
- the *distance measure* of particles and jets;
- the treatment of the *proton remnant*;
- the *recombination scheme* of unresolved particles to a single pseudo-particle or jet;
- the *stopping condition* in a clustering procedure.

The most popular algorithms are briefly introduced below and their properties are summarized in Table 1.

Cone algorithms

Cone algorithms were first proposed by Sterman and Weinberg for e^+e^- annihilations [51] and were then used intensively in $p\bar{p}$ collisions [52]. They maximize the transverse energy flow within a cone of radius $R = \sqrt{\Delta\eta^2 + \Delta\phi^2}$ where $\eta = -\ln \tan(\theta/2)$ is the pseudorapidity and ϕ is the azimuthal angle. The definition of R ensures that the jets found with cone algorithms are invariant under longitudinal boosts of the event particles. Cone algorithms are usually applied in the hadronic centre-of-mass or Breit frame. In both cases $E_{T\ jet}$ reflects the scale of the underlying scattering process. A minimum jet transverse energy $E_{T\ jet}$ is required separating the jets from the proton remnant.

Problems of cone algorithms have been the ambiguities of combining overlapping jets and of defining the seed cells for the cone axes. This has led to various versions of cone algorithms, in some cases even to versions which are not infrared safe [53]. To improve the agreement between data and fixed order predictions an ad-hoc parameter R_{sep} was introduced in theoretical calculations. Now cone algorithms are becoming less popular and k_T clustering algorithms are recommended to be used instead [53].

Modified JADE algorithm

This algorithm originates from the JADE algorithms used in e^+e^- annihilation [54]. It is applied in the laboratory frame. The algorithm is modified compared with the version in e^+e^- annihilation in two respects [55]: (a) a missing-momentum vector is determined and added to

the particles entering the jet algorithm. This allows for the considerable momentum of the proton remnant escaping detection through the beam pipe. (b) the scattered lepton is removed from the final state particles entering the jet algorithm.

The jet algorithm calculates the distance $m_{ij}^2 = 2E_i E_j (1 - \cos \theta_{ij})$ of pairs of particles or ‘proto’ jets i, j . Here E_i and E_j are the energies of the particles i and j , and θ_{ij} is the angle between them. In its conventional form, the jet algorithm combines the pair of particles i, j with the minimum m_{ij}^2 to a ‘proto’ jet by adding their four-momenta p_i and p_j . Other *recombination schemes* have also been used [110, 111]. This prescription is repeated iteratively for the remaining particles and ‘proto’ jets until all possible combinations i, j lead to $m_{ij}^2/W^2 > y_{cut}$, where y_{cut} is the jet resolution parameter and W is the invariant mass of the hadronic final state. Alternatively the clustering may be continued until a fixed number of jets is reached (mostly 2 jets + the proton remnant jet) and the minimum value of $y_{i,j}$ and other variables reconstructed from the jet four-momenta may be investigated. These or similar *stopping conditions* are also used for the following cluster algorithms.

By definition all particles are assigned to a jet. In this sense the algorithm is *exclusive*.

Modified Durham algorithm

The modified Durham algorithm uses the distance measure $k_T^2 = 2 \min[E_i^2, E_j^2] (1 - \cos \theta_{ij})$. Otherwise it is identical to the modified JADE algorithm.

In [56] a new algorithm, the factorizable k_T algorithm, was introduced that leads to jet cross sections with particularly simple factorization properties related to the initial-state collinear divergences. The corresponding n -jet cross sections are of the form

$$\frac{d^2 \sigma^{(n)}}{dx dQ^2} = \frac{2\pi\alpha^2}{Q^4 x} \{ [1 + (1 - y)^2] F_2^{(n)} - y^2 F_L^{(n)} \} \quad (42)$$

where the $F_2^{(n)}$ and $F_L^{(n)}$ are given by

$$F^{(n)}(x, Q^2, y_{cut}) = \sum_{q=u,d,s,\dots,g} \int_x^1 \frac{dz}{z} C_q^{(n)}(z, Q^2, \mu_F, y_{cut}) f_q(x/z, \mu_F). \quad (43)$$

The f_i are the parton densities and $C_q^{(n)}$ are the perturbative coefficients. The appealing property of this and related algorithms is that the perturbative coefficients $C_q^{(n)}$ do not explicitly depend on x or ξ . They have the same structure as the corresponding inclusive coefficients but depend in addition on the jet distance parameter y_{cut} . Unfortunately, in experimental measurements jet polar angle acceptance cuts are usually applied which may spoil these properties.

Factorizable k_T algorithm for DIS

The factorizable k_T algorithm [56] is applied in the Breit frame. It introduces two distance measures: one is the relative $k_{T\ ij}^2 = 2 \min[E_i^2, E_j^2] (1 - \cos \theta_{ij})$ between particles i, j as above; the second is the $k_{T\ i}^2 = 2E_i^2 (1 - \cos \theta_i)$ of each particle with respect to the proton remnant. In each clustering step the minimum $k_{T\ ij}$ and the minimum $k_{T\ i}$ are determined. If the minimum $k_{T\ i}$ is smaller than $k_{T\ ij}$, the particle i is assigned to the remnant jet and is not considered

further. Otherwise the particles i, j are combined to a ‘proto’ jet. The clustering ends if the minimum $k_{T\ i,j}$ of all particles divided by Q^2 or a fixed scale exceeds a given value y_{cut} .

Factorizable JADE algorithm for DIS

This algorithm uses the distance measures $d_{ip} = 2E_i x E_p (1 - \cos \theta_i)$ and $d_{ij} = 2E_i E_j (1 - \cos \theta_{ij})$ [57]. Otherwise it is identical to the factorizable k_T algorithm for DIS.

Longitudinally invariant k_T algorithm

This algorithm uses the distance parameters $d_{ij} = \min[E_i^2, E_j^2] R_{ij}^2$ and $d_i = E_{iT}^2 R^2$ [58, 59]. R_{ij} is given by the difference in pseudorapidity and azimuthal angle ϕ between the particles i, j according to $R_{ij} = \sqrt{(\eta_i - \eta_j)^2 + (\phi_i - \phi_j)^2}$. R is an adjustable parameter of the algorithm which is usually set to 1. In each iteration the minimum $d_{i,j}$ and the minimum d_i are determined. If the minimum d_i is smaller than $d_{i,j}$, the particle i is considered as a jet. (It can not be combined with other particles nor is it assigned to the proton remnant.) Otherwise the particles i, j are combined to a ‘proto’ jet. The clustering ends when no particles and ‘proto’ jets are left. The last particles/‘proto’ jets considered as jets are those with the highest energies.

After jet finding all jets are separated by distances larger than R . Typically events with a given number of jets of minimum energy are selected (e.g. events with at least two jets of $E_T^{Breit} > 10$ GeV). These jets may not contain all particles in the event. In this sense the algorithm is *inclusive*.

algorithm	frame	remnant treatment	resolution criteria
Cone	hadronic cms Breit	minimum $E_{T\ jet}$	$R_{ij} = \sqrt{(\eta_i - \eta_j)^2 + (\phi_i - \phi_j)^2}$, $E_{T\ jet}$
JADE	laboratory	missing-momentum particle	$m_{ij}^2 = 2E_i E_j (1 - \cos \theta_{ij})$
Durham	laboratory	missing-momentum particle	$k_{T\ ij}^2 = 2 \min(E_i, E_j)^2 (1 - \cos \theta_{ij})$
factorizable k_T for DIS	Breit	introduction of $k_{T\ i}^2$	$k_{T\ ij}^2 = 2 \min[E_i^2, E_j^2] (1 - \cos \theta_{ij})$ $k_{T\ i}^2 = 2E_i^2 (1 - \cos \theta_i)$
factorizable JADE	Breit	introduction of d_i	$d_{ij} = 2E_i E_j (1 - \cos \theta_{ij})$ $d_i = 2E_i x E_p (1 - \cos \theta_i)$
longitudinally boost invariant k_T	Breit	introduction of d_i	$d_{ij} = \min[E_{T\ i}^2, E_{T\ j}^2] R_{ij}^2$ $d_{ip} = E_{iT}^2 R^2$

Table 1: Properties of jet algorithms used in DIS at HERA.

1.11.3 Event shape variables

The value of an event shape variable characterizes the topology of the event, which may be pencil-like, planar or spherical. Various variables exist. These variables are calculated using the particles in the current hemisphere of the Breit frame only.

Thrust T_z and T_c

$$T_z = \frac{\sum_h |\mathbf{p}_h \cdot \mathbf{n}|}{\sum_h |\mathbf{p}_h|} = \frac{\sum_h |\mathbf{p}_{z h}|}{\sum_h |\mathbf{p}_h|}, \quad T_c = \max \frac{\sum_h |\mathbf{p}_h \cdot \mathbf{n}_T|}{\sum_h |\mathbf{p}_h|} \quad (44)$$

For T_z the longitudinal momentum components are projected onto the incoming boson axis \mathbf{n} . For T_c the vector \mathbf{n}_T which maximizes the value of T_c is taken as thrust the axis.

Jet broadening B_c

$$B_c = \frac{\sum_h |\mathbf{p}_h \times \mathbf{n}|}{2 \sum_h |\mathbf{p}_h|} = \frac{\sum_h |\mathbf{p}_{\perp h}|}{2 \sum_h |\mathbf{p}_h|}. \quad (45)$$

 C parameter

$$C = 3(\lambda_1 \lambda_2 + \lambda_2 \lambda_3 + \lambda_3 \lambda_1) \quad (46)$$

where the λ_i are the eigenvalues of the linearized momentum tensor $\theta^{\mu\nu}$ which is given by

$$\theta^{\mu\nu} = \frac{\sum_h \mathbf{p}_h^\mu \mathbf{p}_h^\nu / |\mathbf{p}_h|}{\sum_h |\mathbf{p}_h|}. \quad (47)$$

Scaled jet mass ρ

$$\rho = \frac{(\sum_h p_h)^2}{4(\sum_h E_h)^2} = \frac{M^2}{2 E_{tot}^2}. \quad (48)$$

1.12 The HERA collider

The collider HERA located at DESY is the first facility with colliding electron and proton beams. The electron and proton storage rings are housed in a tunnel of 6.3 km circumference. The bending magnets of the proton ring are superconducting. The energies of the electron and proton beams are currently 27.5 GeV and 920 GeV respectively. The bunch separation corresponds to 96 ns. HERA has been colliding both electrons and positrons. The integrated luminosity, beam energies and colliding particle types in different years are listed in Table 2.

In 1999 HERA was operated with 175 colliding electron and proton bunches. The average beam currents were $I_e = 19$ mA and $I_p = 80$ mA. The average luminosity was $4 \cdot 10^{30}$ cm⁻²s⁻¹ corresponding to the design value.

Two interaction regions of the ep beams house the H1 and ZEUS detectors. Two fixed target detectors HERMES and HERA-B make use of the electron or proton beam only. HERMES is measuring spin structure functions. They use a target of polarized hydrogen, deuterium or helium gas placed in the electron beam vacuum chamber. Spin rotators before and after the gas target flip the spin of the electrons, which are polarized transversely due to the Sokolov-Ternov effect [60] and provide longitudinal polarization. The HERA-B experiment is investigating CP violation in the B meson system by placing a wire target within the halo of the proton beam.

In September 2000 the installations for the HERA luminosity upgrade will start. It implies major modifications of the interaction regions of the H1 and ZEUS detectors in order to create the space for stronger focussing magnets. After the upgrade the luminosity should increase by a factor of five such that data samples of ≈ 150 pb⁻¹/year will be collected. Spin rotators will be installed at H1 and ZEUS providing longitudinally polarized electrons.

Year	'92	'93	'94	'95	'96	'97	'98	'99	2000
$\int \mathcal{L}$ [pb ⁻¹]	0.05	0.9	0.9/5	10	15	33	8	17/26	> 25
Lepton	e^-	e^-	e^-/e^+	e^+	e^+	e^+	e^-	e^-/e^+	e^+
E_p [GeV]	820	820	820	820	820	820	920	920	920
E_e [GeV]	26.7	26.7	27.5	27.5	27.5	27.5	27.5	27.5	27.5

Table 2: Summary of the annual luminosity delivered by HERA for different beam particles and beam energies ⁴.

1.13 The H1 and ZEUS detectors

The instrumentation of the H1 and ZEUS detectors is optimized for reliable identification and precise measurement of the scattered electron and full coverage of the hadronic final state. Like any other high energy collider detector the H1 and ZEUS detectors consist of inner tracking chambers surrounded by electromagnetic and hadronic calorimeters. Both experiments use superconducting solenoids to create the magnetic field for track transverse momentum measurements. The field strength is 1.15 T for H1 and 1.4 T for ZEUS. The iron return yokes are

⁴The luminosity as seen by the H1 experiment is given. Data taking has not yet finished in 2000. HERA had provided ≈ 25 pb⁻¹ by May 2000.

instrumented to identify muons and to detect hadronic shower leakage out of the main calorimeters. Characteristic of H1 and ZEUS are:

- the asymmetry of the detectors with enhanced instrumentation in the direction of the proton beam;
- the strong emphasis on hadronic calorimetry;
- the high level of readout pipelining combined with fast and highly selective triggering.

These features are required by the large energy difference of the electron and proton beams, the high centre-of-mass energy, the short bunch spacing of 96 ns and the relatively large rate of background events induced by beam-gas and beam-wall interactions of the proton beam.

A major difference between H1 and ZEUS is their choice of main calorimeters. H1 chose a liquid argon calorimeter (LAr) in the central and forward region of the experiment. The LAr offers high granularity and good electron energy resolution together with stable calibration. The backward detector region is instrumented with a high resolution lead/scintillating-fibre calorimeter (SPACAL). ZEUS chose a compensating uranium-scintillator calorimeter with excellent hadronic energy resolution and combined energy and time measurement in the forward, central and backward region. The geometrical acceptance and the resolution of the main tracking detectors and calorimeters of H1 and ZEUS are given in Table 3. More detailed information may be found in [61, 62].

	H1		ZEUS
Tracking	central	backward	central
acceptance	25 – 155°	151 – 177.5°	15 – 164°
σ/p_T	< 0.01 p_T		0.0058 $p_T \oplus$ 0.0065 \oplus 0.0014/ p_T
Calorimetry	LAr	Spacal	UCAL
acceptance	4 – 154°	151 – 177.8°	2.6 – 176°
σ/E (electrons)	12%/ $\sqrt{E} \oplus$ 1%	7.5%/ $\sqrt{E} \oplus$ 1%	18%/ $\sqrt{E} \oplus$ 1%
σ/E (hadrons)	50%/ $\sqrt{E} \oplus$ 2%	\approx 40% at 4 GeV	35%/ $\sqrt{E} \oplus$ 1%

Table 3: Properties of the main drift chambers and calorimeters of H1 and ZEUS.

Both experiments have several trigger levels. The selection at the first trigger stage is made after $\approx 2.4 \mu\text{s}$ (H1) and $4.4 \mu\text{s}$ (ZEUS). During this time the detector readout information is stored in analogue or digital pipelines such that no dead time is introduced.

Since 1992 various detector upgrades have taken place which have improved electron identification and measurement and extended the detector acceptance closer to the beam line. Central (CST) and backward (BST) silicon tracking detectors, and high resolution backward calorimeters (SPACAL and VLQ) for H1 were installed. ZEUS installed new detectors at the very backward (BPC and BPT) and forward region of their experiment. For the measurement of diffractive events, proton and neutron detectors were installed in the very forward region of the H1 and ZEUS detectors.

The luminosity is determined by measuring the small angle bremsstrahlung process $ep \rightarrow e\gamma p$ in dedicated electron and photon detectors located ≈ 30 and ≈ 100 m upstream (wrt. proton direction) respectively.

2 Data description and test of QCD matrix elements

In this section measurements of observables sensitive to QCD radiation are presented in characteristic phase space regions. The quality of the data description by QCD models and perturbative QCD in leading and next-to-leading order is investigated. The most basic predictions of the QCD matrix elements are tested. Jets provide a particularly suggestive relation to the underlying partonic structure of a given event and frequently jet related observables are used below. Examples of two selected DIS events with pronounced jet structures are shown in Figure 13.

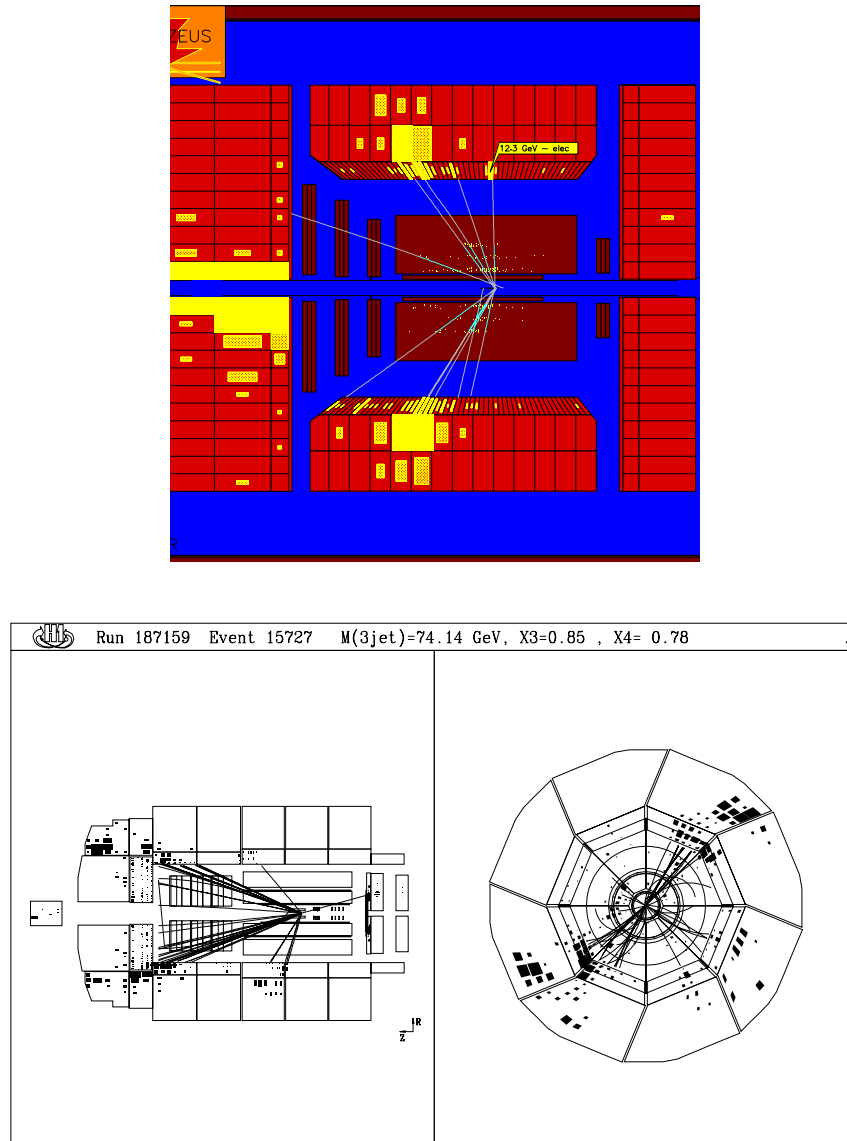


Figure 13: Neutral current DIS events with the scattered electron and two jets (top) or three jets (bottom).

2.1 QCD models for DIS

The analysis of elementary particle collisions is impossible without a detailed simulation of the expected event properties. This requires QCD models in form of *Monte Carlo generators* which generate artificial events with full information on all produced particles. Combined with detailed detector simulation programs Monte Carlo (MC) generators are important in order to

- determine the effect of detector acceptance and resolution;
- estimate the hadronization corrections needed for comparison with perturbative predictions;
- provide theoretical predictions in regions where fixed-order calculations are not applicable.

The main QCD MC models that have been used in DIS at HERA are ARIADNE [63], HERWIG [64], LEPTO [65] and RAPGAP [66].

ARIADNE is based on the colour dipole model. The first gluon emission is corrected to reproduce the LO matrix element. Boson-gluon-fusion does not naturally occur in the CDM. It is implemented using the LO matrix elements and then setting up the colour dipoles accordingly [67]. Hadronization is performed with the Lund string model. Diffractive events can be modeled by scattering on a Pomeron with given parton densities.

Here the version 4.10 of ARIADNE is mostly used where the phase space restriction related to the size of the proton was relaxed [68]. This leads to an improved data description at high Q^2 .

LEPTO models the QCD cascade with leading logarithm parton showers based on the DGLAP evolution equations. Hard processes are described by the LO matrix elements the divergences of which are avoided by restrictions on z_q and \hat{s} , the invariant mass of the diparton system. Hadronization is performed with the Lund string model. Diffractive events are produced by a non-perturbative rearrangement of the colour flow between the proton remnant and final state partons – the soft colour interactions (SCI) [69]. A refinement of the SCI is provided by the generalised area law (GAL) model [70]. In the GAL model soft colour interactions are suppressed depending on the difference in area spanned between two possible string configurations.

HERWIG models initial-state and final-state QCD radiation with DGLAP parting showers including colour coherence effects and azimuthal correlations due to gluon polarization. Hadronization is performed with the cluster fragmentation model.

RAPGAP contains implementations of various models for diffractive and non-diffractive processes. For standard DIS processes it is similar to LEPTO. RAPGAP is able to simulate DIS processes with a resolved (virtual) photon. As the cut-off parameter of the LO order matrix element the transverse parton momentum p_T is used. Hadronization is performed with the Lund string model.

Two further models which have not yet been widely used are the LDC model and CASCADE

LDCMC is based on the Linked Dipole Chain (LDC) model which corresponds to a reformulation of the CCFM equation in terms of the colour dipole model. Initial state partons are assumed to form a chain of linked colour dipoles which emit (final state) partons independently. Hadronization is performed with the Lund string model.

CASCADE [71] implements the CCFM equation in backward evolution and uses the unintegrated gluon density. Hadronization is performed with the Lund string model.

2.1.1 Radiative QED corrections

Photon radiation from the incoming or scattered lepton can lead to substantial effects in inclusive DIS, depending on the way the kinematic variables are reconstructed from the lepton or hadronic final state four-momenta [72]. Also the hadronic final state properties are significantly influenced by QED radiation. Emission of photons collinear to the incoming lepton, for example, may reduce the effective energy in the hard scattering process and shift the hadronic final state into the proton direction.

There are several programs to calculate radiative corrections in DIS [73]. The program HERACLES [74] which contains the $O(\alpha)$ corrections has been interfaced with LEPTO (and ARIADNE) in the Monte Carlo program DJANGO [75]. HERACLES is also used by RAPGAP.

All measurements presented in this review are corrected for the effects of QED radiation using DJANGO.

2.2 Perturbative QCD calculations in next-to-leading order

Confrontation of measurements with perturbative QCD calculations in NLO belongs to the most powerful tests of QCD at short distances. NLO calculations are theoretically well defined making meaningful extractions of physical quantities like the strong coupling or the parton densities possible. Renormalization (and factorization) scale dependences are (much) reduced in NLO compared with the leading-order predictions. The following principle restrictions of NLO calculations must be kept in mind:

- Contributions to the perturbative series higher than NLO are neglected. No complete calculations higher than NLO are yet available for exclusive observables in DIS or e^+e^- annihilation.
- Non-perturbative corrections should be small or must be taken into account.
- Only distributions of observables that are infrared and collinear safe can be predicted.
- NLO predictions are expected to be reliable at large energy scales or scattering angles. Collinear or soft radiation leads to enhanced terms and may require resummed calculations or next-to-next-to-leading order (NNLO) calculations in order to describe the data.

Given the NLO matrix elements the main difficulty of NLO calculations is the treatment of divergences. Several types of divergences are encountered in perturbative calculations: soft, collinear and ultraviolet singularities due to the *virtual* (loop) corrections and soft and collinear singularities due to the *real* corrections. The ultraviolet divergences and the initial-state collinear divergences are absorbed into the running coupling and into the parton density functions, respectively, as was discussed before. For infrared finite observables the remaining real and virtual singularities cancel according to the Kinoshita-Lee-Nauenberg mechanism.

For most observables analytical calculations are involved, and consequently the perturbative calculations for DIS are provided in the form of NLO Monte Carlo programs. These provide weighted events with the parton four-momenta and the four-momentum of the scattered lepton. The latest generation of NLO programs makes possible the calculation of (nearly) any infrared safe variable and arbitrary choice of selection criteria, parton densities, values of α_s or renormalization and factorization scales. Two general methods to organize the cancellation of singularities independently of the choice of observable are used: the *phase-space slicing method* [76] and the *subtraction method* [77]. In both methods the singular parts are first isolated and then treated analytically. The remaining finite parts are treated numerically.

- *Phase-space slicing method*: This method introduces a small technical cut-off, the phase-space slicing parameter, defining e.g. a cone around each parton. Infrared and collinear divergences associated with parton emission within the cone are integrated over analytically using soft and collinear approximations. Adding the resulting singular expression to the contribution from the virtual corrections gives a finite result. Outside the cone the integral over parton emissions is evaluated numerically.

The phase-space slicing parameter must be chosen small enough for the soft and collinear approximations to be valid. This can be tested by comparing calculations with different parameter values.

- *Subtraction method*: In this method a local counter-term is defined which matches the singularity structure of the real corrections exactly and which is simple enough to be integrated analytically over the single-parton subspace regions leading to soft and collinear divergences. The counter-term is subtracted from the real corrections and added to the virtual corrections to be integrated over. The remaining integrals are finite and can be evaluated numerically.

The difficulty of the subtraction method is the construction of the counter-term.

Currently four programs MEPJET [78], DISENT [79], DISASTER++ [80], JETVIP [81] are available.⁵

MEPJET was the first program for calculating general infrared safe quantities in deep-inelastic scattering. It employs the phase-space slicing method with an invariant cut-off parameter s_{min} .

⁵Two older programs DISJET [82] and PROJET [83] were restricted to the modified JADE cluster algorithm and partly made inadequate approximations.

MEPJET is at present the only program to include Z^0 and W^\pm exchange, polarized cross sections and quark mass effects in the leading order matrix element.

DISENT uses the subtraction method. The subtraction terms are obtained via dipole factorization [79]. Out of the four programs under consideration DISENT is the fastest, a property that is of major practical relevance. The factorization scale can essentially be chosen as a fixed multiple of the photon virtuality Q only.

DISASTER++ cancels singularities by means of the subtraction method together with a generalized partial fraction formula. DISASTER++ is the only program that allows for both arbitrary choices of the factorization scale and the number of flavours N_f on an event-by-event basis.

JETVIP includes photoproduction ($Q^2 \approx 0$) and processes with a *resolved virtual* photon in addition to the usual deep-inelastic scattering with a pointlike virtual photon. The phase-space slicing method with a cut-off parameter y_{cut} is used. The azimuthal dependence of the matrix elements is only contained to LO. This can influence jet cross sections when jet cuts in the laboratory frame are made.

A summary of the main features of these QCD programs for (1+1) and (2+1) jet cross sections is given in Table 4.

(1+1) and (2+1) jets	MEPJET	DISENT	DISASTER++	JETVIP
renormalization scale	all	all	all	all
factorization scale	all	Q^2 , const.	all	all
W^\pm/Z^0 exchange	×	–	–	–
inclusion of resolved γ^*p	–	–	–	×
inclusion of γp	–	–	–	×
ϕ -dependence	×	×	×	only LO
quark mass effects	only LO	–	–	–
polarized ep	×	–	–	–
(3+1) jets	LO	LO	LO	LO
(4+1) jets	LO	–	–	–

Table 4: Properties of QCD programs. A ‘×’ indicates that a given feature is implemented in the program. A ‘–’ indicates that it is not.

The above programs must make identical predictions within their statistical accuracy if the parton density functions, α_s , renormalization and factorization scales are chosen consistently. **Systematic comparison of the programs** were performed in [84, 86]. While excellent agreement is observed in LO, several inconsistencies were found in NLO. The most important inconsistencies are a systematic difference of 5-10% between MEPJET and DISENT or DISASTER++ and a surprisingly large dependence of JETVIP on the value of the phase-space slicing parameter [85]. The origin of these effects is not yet understood and it is recommended to use DISENT or DISASTER++ for NLO calculations when possible [86]. In [87] an inconsistency between DISENT and analytical calculations of thrust was reported for very large values of thrust which is, however, irrelevant for any of the jet cross sections presented here.

2.3 Jet shape and subjet multiplicities

Investigation of the internal structure of a jet through measurement of jet shape and subjet multiplicities tests the transition between perturbative QCD and non-perturbative effects. In LO perturbative QCD a jet is formed by a single parton. Only in NLO can jets be composed of two partons and thus acquire internal structure. Multiple gluon emissions and finally hadronization yield the jets as seen by experiment. Differences between quark and gluon jets are expected due to the different colour charge of quarks and gluons. Thus gluon jets should be broader than quark jets. The proper description of internal jet structure by QCD models is important for measurements of multi-jet cross sections.

A measure of jet shape is given by the variable $\Psi(r)$ defined as the fraction of jet transverse energy carried by the particles in the subcone of radius $r \leq R$ centered around the jet axis. By definition $\Psi(0) = 0$ and $\Psi(R) = 1$. ZEUS have measured $\Psi(r)$ in neutral and charged current DIS at $Q^2 > 100 \text{ GeV}^2$ [88] (see Figure 14). The jets are found with an iterative cone algorithm with cone radius $R = 1$ [89] applied in the laboratory frame. Events with jet transverse energies $E_{T,jet}^{lab} > 14 \text{ GeV}$ in the angular range of $-1 < \eta^{lab} < 2$ are selected. The event sample is dominated by events with a single jet.

The distribution $\Psi(r)$ measured in NC and CC processes at HERA is similar to that measured in e^+e^- annihilation by the OPAL experiment for roughly comparable jet energies. In contrast, the $\Psi(r)$ measured in $p\bar{p}$ collisions at the TEVATRON are found to rise significantly slower with increasing cone radius r , corresponding to broader jets. These differences are qualitatively expected since the jets selected in DIS and e^+e^- annihilation are predominantly quark jets whereas those of $p\bar{p}$ collisions are dominated by gluon jets.

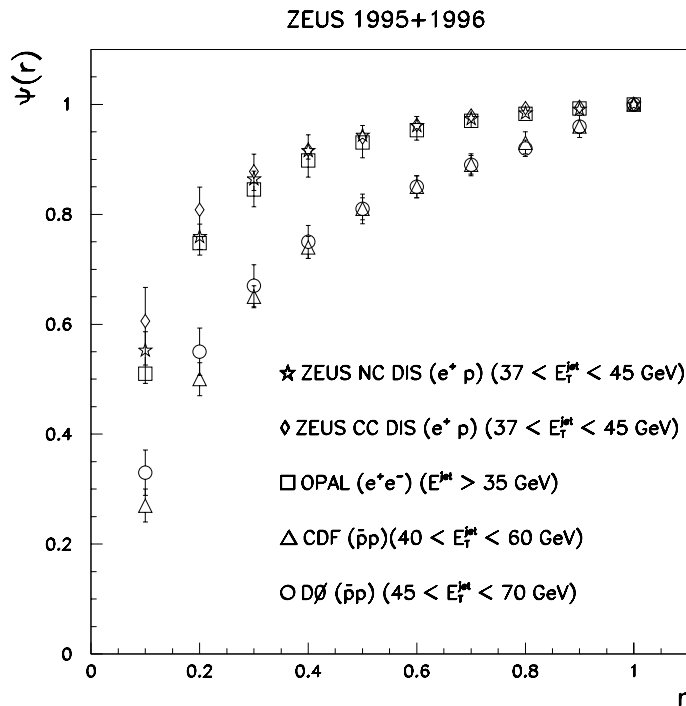


Figure 14: Jet shape distributions

H1 have measured jet energy fractions and subjet multiplicities at $10 < Q^2 < 120 \text{ GeV}^2$ reconstructing multi-jet events in the Breit frame [90]. The data sample of $\approx 2 \text{ pb}^{-1}$ was collected in '94. The subjet multiplicity is determined in the following way. First the longitudinally invariant k_T algorithm is applied to define jets with $E_{T,jet}^{Breit} > 5 \text{ GeV}$ yielding predominantly dijet events. Then clustering is repeated for all particles assigned to a given jet. The subjet multiplicity corresponds to the number of jets i, j with

$$\frac{\min_{i,j}(E_{T,i}^2, E_{T,j}^2) R_{ij}}{E_{T,jet}^2 R^2} > y_{cut} . \quad (49)$$

R is chosen to be 1. The subjet multiplicity as a function of y_{cut} is shown in Figure 15. For large y_{cut} no subjets other than the original jet are found, and the number of subjets is one. For very small y_{cut} every particle in the jet becomes a subjet. The subjet multiplicity is well described by LEPTO. The subjet multiplicity of quark and gluon jets as predicted by LEPTO are also shown separately. Gluon jets contain significantly more subjets than quark jets. The data are found to be well compatible with the quark jet prediction. This corresponds to the dominance of gluon-induced dijet events with a quark and antiquark jet in the final state. The dependence of jet shape and subjet multiplicities as a function of jet transverse energy and pseudorapidity is determined. As expected jets become more collimated with increasing transverse energy. The measured dependences are roughly reproduced by the QCD models ARIADNE, HERWIG and LEPTO.

Methods to identify quarks and gluon jets on an event-by-event basis have not yet been applied at HERA.

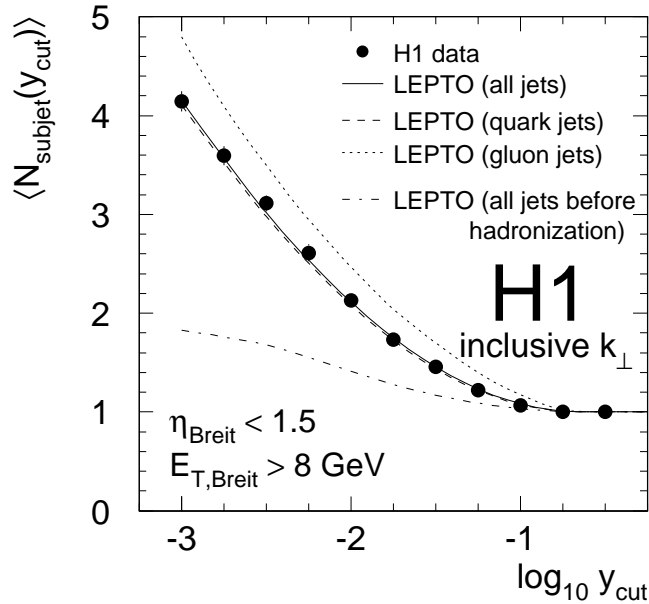


Figure 15: Mean subjet multiplicity in dijet events

2.4 Dijet cross sections

While single jet events can be produced by scattering off a nucleon's quark in the QPM, dijet production in DIS requires a strong interaction. Dijet cross sections are thus sensitive to the QCD matrix elements and various measurements of dijet cross sections have been performed in DIS at HERA. A recent ZEUS measurement of the dijet cross section as a function of Q^2 is shown in Figure 16. The jets are found with the longitudinally invariant k_T algorithm requiring $E_{T_{jet}}^{Breit} > 5$ GeV and $E_{T_{jet}}^{Breit} > 8$ GeV for the jet with minimum and maximum $E_{T_{jet}}^{Breit}$, respectively [91]. In addition it is required that $E_{T_{jet}}^{lab} > 5$ GeV. The jets are restricted to the angular range of $-2 < \eta^{lab} < 2$. The asymmetric selection in $E_{T_{jet}}^{Breit}$ avoids the region where the virtual correction to two parton final states cannot be compensated by the real corrections due to limited phase space for the third (soft) particle [92].

The data are well described by NLO calculations over the huge kinematic range of $10 < Q^2 < 10,000$ GeV² if the renormalization scale $\mu_R^2 = Q^2$ is chosen. In the following subsections dedicated dijet measurements in the region of low, medium and high Q^2 are presented and are discussed in more detail.

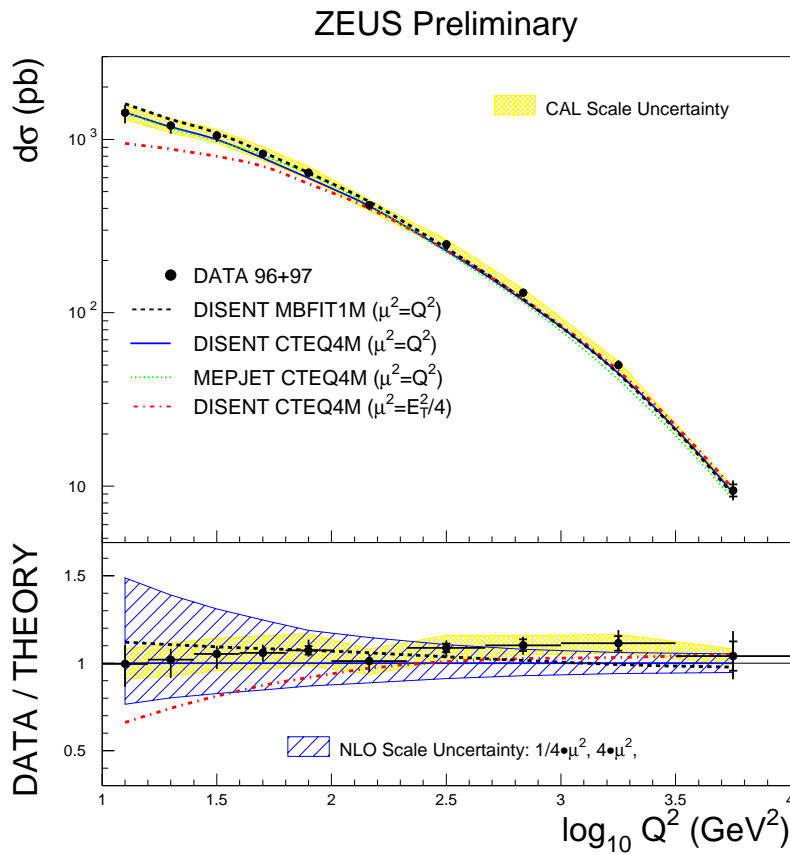


Figure 16: Dijet cross section $d\sigma/dQ^2$ in the range $10 < Q^2 < 10,000$ GeV² compared with QCD predictions in NLO.

2.4.1 Jet rates at small x and Q^2

H1 have measured the dijet rate $R_2(x) = N_2(x)/N_{DIS}(x)$ in the kinematic range of $5 < Q^2 < 100 \text{ GeV}^2$ [93]. The measurement is based on data collected in '96-'97 corresponding to an integrated luminosity of 22 pb^{-1} .

The jets are found with the longitudinally invariant k_T algorithm applied in the hadronic centre-of-mass (hcms) frame requiring $E_{T_{jet}}^{hcms} > 5 \text{ GeV}$ and $E_{T_{jet}}^{hcms} > 7 \text{ GeV}$ for the jet with minimum and maximum $E_{T_{jet}}^{hcms}$, respectively. The jets' pseudorapidities must satisfy $-1 < \eta^{lab} < 2.5$. The dominant experimental error of $\approx 10\%$ is due to the hadronic energy scale uncertainty of the H1 liquid argon calorimeter. This effect is typical for many jet measurements where events are selected due to requirements of a minimum transverse jet energy which cuts in a steeply falling distribution. The QCD models' dependence on the corrections for detector effects introduces an uncertainty of similar size.

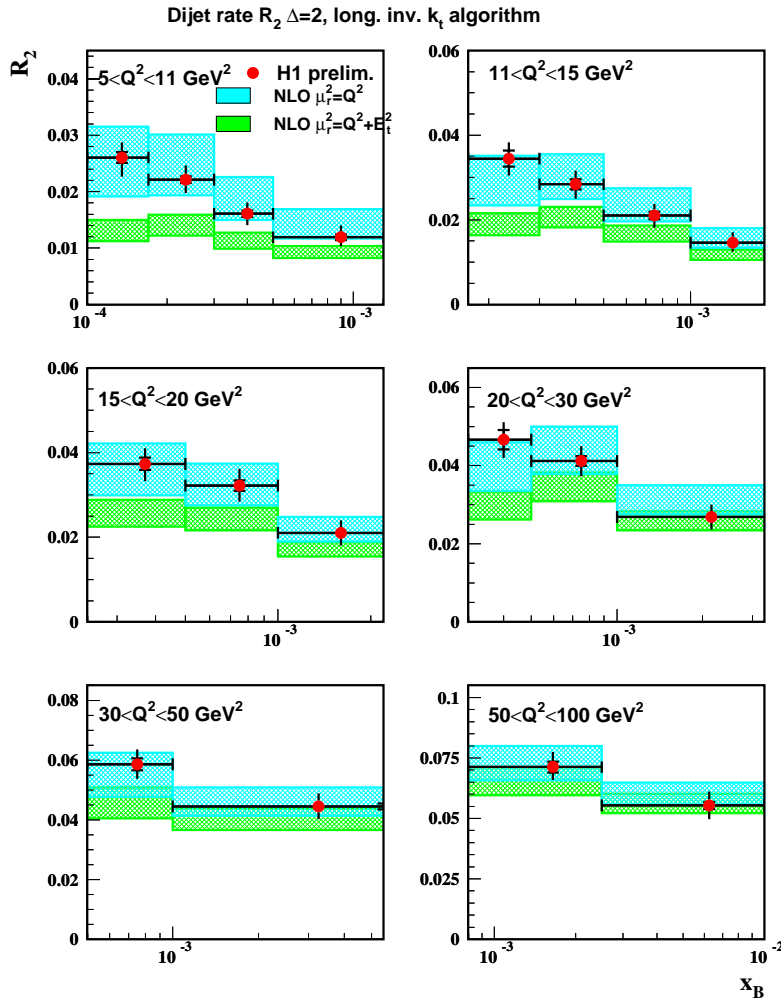


Figure 17: Dijet event rate $R_2(x)$ in the range $5 < Q^2 < 100 \text{ GeV}^2$ compared with QCD predictions in NLO.

In Figure 17 $R_2(x)$ is compared with perturbative QCD predictions in NLO for two choices of renormalization scale $\mu_R^2 = Q^2$ and $\mu_R^2 = E_{T,jet}^2 + Q^2$. The width of the shaded bands reflects the renormalization scale uncertainty of the NLO prediction which is estimated varying $\mu_R^2 = Q^2$ to $1/4 Q^2$ and $4 Q^2$ and correspondingly for the scale $\mu_R^2 = E_{T,jet}^2 + Q^2$. The choice of $\mu_R^2 = Q^2$ gives a fair description of the data in the full range of the measurement. The predictive power of the NLO calculation is limited by the large renormalization uncertainty, however. Choosing $E_{T,jet}^2 + Q^2$ as the renormalization scale leads to significant deviations from the measurement which are most pronounced at low Q^2 . For this choice of scale the relative uncertainty of the NLO variation, defined as above, is reduced. Note that choosing $E_{T,jet}^2$ as renormalization scale would further lower the NLO prediction. The interpretation of these findings is open. They may indicate that contributions higher than NLO are large.

The region of low Q^2 and x is of particular interest due to the possible break down of DGLAP parton evolution at low x . Related measurements are presented in much detail in section 5. Here we note that a full NLO calculation based on DGLAP evolution can describe the dijet rate $R_2(x)$ provided the renormalization scale is chosen to be Q^2 .

2.4.2 Dijet production at large Q^2 and $E_{T,jet}^{Breit}$

H1 have measured differential dijet event rates in the kinematic region of $Q^2 > 150 \text{ GeV}^2$. The measurement is based on data collected in '95-'97 corresponding to an integrated luminosity of 35 pb^{-1} . The jets are found with the factorizable k_T algorithm for DIS [94], and dijet events with $y_2 = k_T^2/100 \text{ GeV}^2 > 0.8$ are selected. The jets have to be detected in the polar angular range of $10^\circ < \theta_{jet}^{lab} < 140^\circ$. The average transverse jet energy in the Breit frame $E_{T,jet}^{Breit}$ is $\approx 10 \text{ GeV}$.

The dijet event distributions y_2 , θ_{fwd} and θ_{bwd} corresponding to the polar angle of the forward and backward jet, z_p and x_p are studied. The variable x_p is defined as in equation (36) but replacing the parton four-momenta by those of the reconstructed jets. The definition of z_p is given by

$$z_p = \min_{i=1,2} E_{jet\ i} (1 - \cos \theta_{jet\ i}) / \sum_{i=1,2} E_{jet\ i} (1 - \cos \theta_{jet\ i}). \quad (50)$$

For massless jets this definition corresponds to the minimum of the two z_i defined in equation (37).

The distributions of all observables are well described by perturbative QCD in NLO combined with hadronization corrections (see Figure 18). The QCD models LEPTO 6.5 (without SCI) and ARIADNE 4.08 describe the data less well than perturbative QCD in NLO.

The region of large Q^2 and large jet transverse energies $E_{T,jet}^{Breit}$ belongs to the phase space regions that are best understood in DIS at HERA. The good agreement with perturbative QCD in NLO is the basis for the determinations of the strong coupling α_s and of the parton density functions presented in sections 3 and 4.

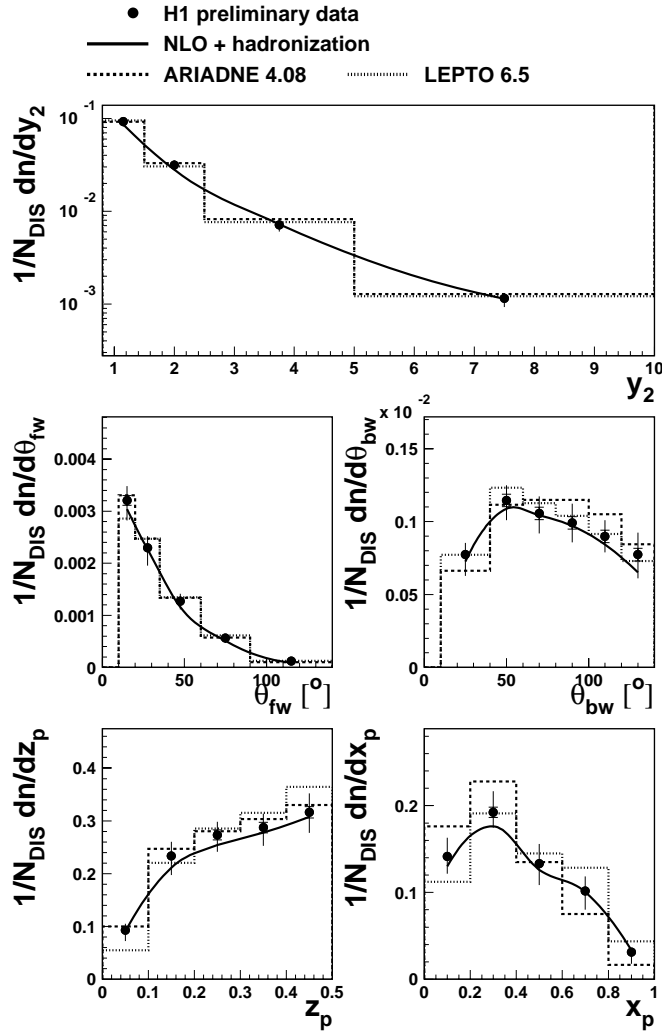


Figure 18: Dijet event distributions in NC processes at $Q^2 > 150 \text{ GeV}^2$ compared with the predictions of QCD models and perturbative QCD in NLO.

2.4.3 Dijet production in CC and NC interactions at highest Q^2

In the kinematic region of the highest accessible Q^2 at HERA the exchange of either gauge boson γ/Z^0 and W^\pm is observed, and the standard model of electroweak and strong interactions is probed at distances as small as 10^{-18} m . Possible deviations from the standard model may most likely be seen in this region. Detailed measurements of the *inclusive* DIS cross section at high Q^2 in both NC and CC interactions have been performed (see Figures 5 and 11) and no significant deviations from the standard model have been found.

It is important to complement these results by dedicated investigations of the hadronic final state. H1 have measured dijet distributions in the kinematic region of $640 < Q^2 < 25,000 \text{ GeV}^2$ in both CC and NC interactions [95].⁶ The data sample was collected in '94-'97. The

⁶Single jet distributions in CC events have been studied in detail in [96].

H1 preliminary

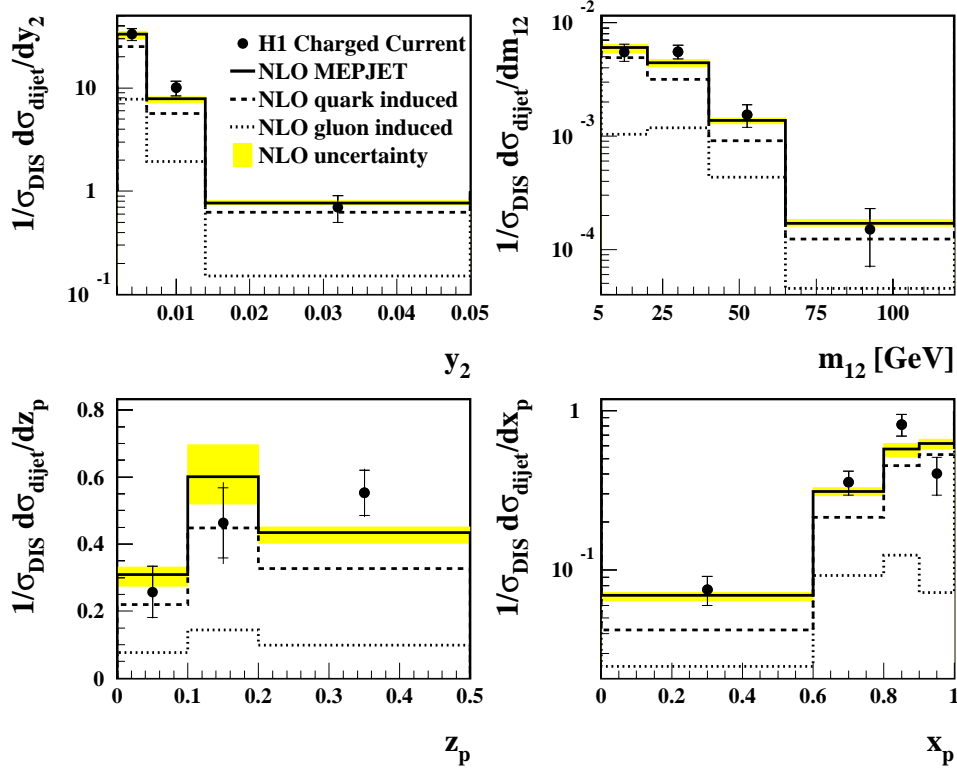


Figure 19: Dijet event distributions in CC processes at $Q^2 > 640 \text{ GeV}^2$ compared with perturbative QCD predictions in NLO.

jets are found with the modified Durham algorithm which is applied in the laboratory frame. This avoids boosting and thus increased experimental error in CC events where the outgoing neutrino is not directly observed in the detector and the kinematic variables are determined from the hadronic final state. Dijet events are selected by requiring the minimum jet distance $y_2 = k_T^2/W^2$ to exceed 0.002 which yields a fraction of dijet events of $\approx 25\%$. This choice of dijet selection is motivated by the small DIS cross sections at high Q^2 . Only events in the polar angular range of 10° to 140° are accepted. In total, 130 CC and 1400 NC dijet events remain. The number of NC events is larger than that of CC events since the contributions from pure photon exchange still dominate Z^0 exchange. In Figure 19 the measured dijet distributions of the CC event sample are compared with perturbative QCD in NLO as calculated with the program MEPJET. Hadronization corrections determined with QCD models are added to the NLO predictions. The measurement is dominated by statistical uncertainties. The systematic experimental uncertainties are $\approx 7\%$ on average.

The CC dijet distributions are well compatible with the NLO predictions and provide clear evidence for dijet production in CC interactions. The NLO predictions are also shown for quark

and gluon induced processes separately. The gluon-induced cross section is small at high Q^2 (and large x). Added to the quark-induced processes it improves the data description.

A good data description by perturbative QCD in NLO is also found for the NC events selected in the same kinematic range as the CC events [95] (not shown).

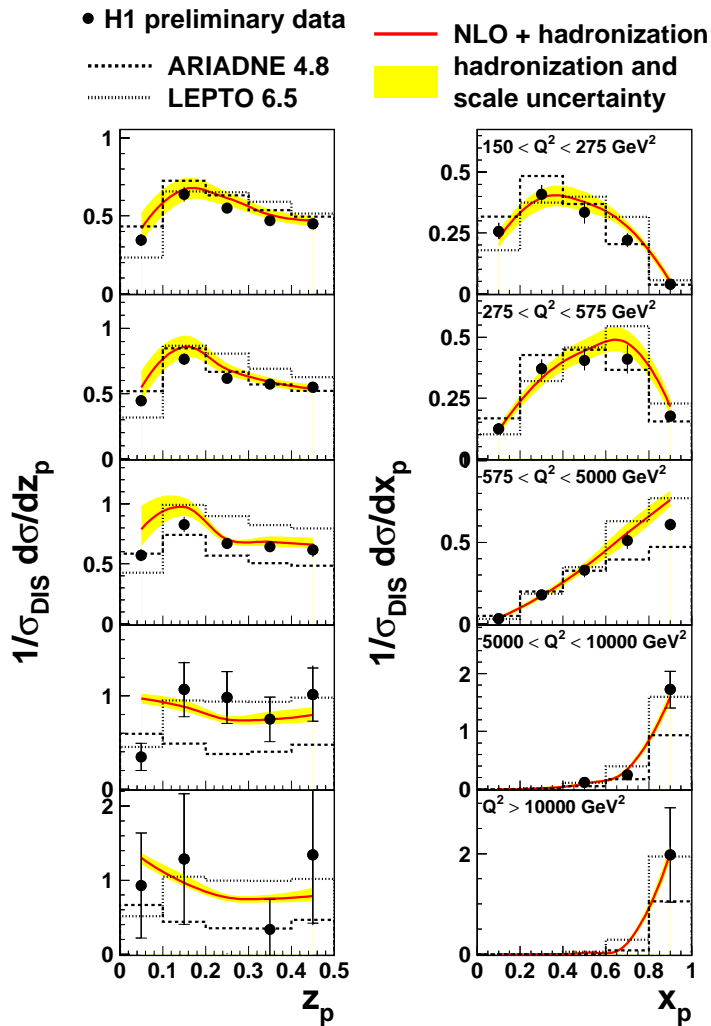


Figure 20: Dijet event distributions as a function of z_p and x_p at highest Q^2 .

An extension of the NC measurement to higher values of Q^2 than is possible for the CC events is shown in Figure 20 where the kinematic region of $150 < Q^2 < 30,000 \text{ GeV}^2$ is divided into five Q^2 bins including the bin $Q^2 > 10,000 \text{ GeV}^2$. The minimum jet distance is reduced to $y_2 > 0.001$ compared with the analysis above. Thus less hard jet structures are selected and the region where perturbative QCD in NLO is expected to become less reliable is approached. Nevertheless perturbative QCD in NLO (DISSENT) combined with hadronization corrections gives a fair description of the data over the full Q^2 range. Recall that DISSENT does not contain Z^0 exchange. The effect of Z^0 exchange on the (normalized) jet cross sections is estimated using ARIADNE and is found to be small.

The precision of the measurement in the three bins below $Q^2 < 5,000 \text{ GeV}^2$ is high. Thus it can be noticed that the data tend to fall below the NLO prediction in the region of small z_p and large x_p . This is expected since here the contribution from single jets which are not considered in the NLO calculation may still be visible. The data description by the QCD models LEPTO and ARIADNE is significantly worse than that obtained by QCD in NLO. These and related distributions have been used to optimize the parameters of LEPTO [97].

The fraction of gluon-induced events varies from $\approx 80\%$ to less than 5% in the Q^2 range covered and thus different matrix elements are tested. The successful description of the data is a significant test of QCD. In addition it is important to note that no peculiarities are observed in the bin $Q^2 > 10,000 \text{ GeV}^2$. A precision test of QCD (and the standard model) at $Q^2 > 10,000 \text{ GeV}^2$ will only be achieved after the luminosity upgrade of HERA.

2.5 Azimuthal asymmetries

The azimuthal dependence of the diparton cross section in equations (38) and (39) has been proposed as early as 1978 as an interesting test of perturbative QCD in DIS [98]. The partonic cross section is not uniform in the angle ϕ but shows the following asymmetry [99, 100, 101, 102, 103] in LO:

$$\frac{d\sigma}{d\phi} = A + B \cos \phi + C \cos 2\phi . \quad (51)$$

This is a consequence of helicity conservation at the lepton-photon and the photon-quark vertices and of interference of the different photon polarization states. Unfortunately the intrinsic transverse momentum k_T of a quark confined in the proton introduces azimuthal asymmetries of the same form [99]. Fixed target experiments measured a non-vanishing $\cos \phi$ term [104, 105] using charged particles with large momentum energy fractions to reconstruct ϕ . The observation is compatible with non-perturbative effects and was used to constrain k_T .

ZEUS have measured the azimuthal distribution using energetic charged particles in the kinematic range of $0.2 < y < 0.8$ and $0.01 < x < 0.1$ corresponding to $180 < Q^2 < 7220 \text{ GeV}^2$. Tracks with transverse momenta in the laboratory frame of $p_T^{lab} > 150 \text{ MeV}$ are accepted. The energy fraction of the particles, expressed in the variable $z_h = P \cdot p_h / P \cdot Q$, is required to be in the range of $0.2 < z_h < 1$. The selection of leading particles improves the hadron-parton correlation. Here ϕ is defined as the angle of a hadron in the plane perpendicular to the virtual boson direction. The intersection with the lepton scattering plane defines $\phi = 0$.

In Figure 21 the distribution of ϕ is shown for four values of minimum transverse particle momentum p_c in the hadronic centre-of-mass frame. At low p_c , a modulation proportional to $\cos \phi$ is observed while at large p_c a significant $\cos 2\phi$ term is observed.

The mean values of $\cos \phi$ and $\cos 2\phi$ as a function of minimum p_c are compared with QCD model predictions in Figure 22. The $\cos \phi$ distribution is in agreement with the predictions at large p_c . In particular at low p_c it is estimated to be sensitive to non-perturbative effects and to the QCD model parameters. In contrast, non-perturbative contributions to $\cos 2\phi$ are found to be negligible. The $\cos 2\phi$ distribution is described by the QCD models when the azimuthal dependence is properly included into the LO matrix elements. Removing the azimuthal dependence

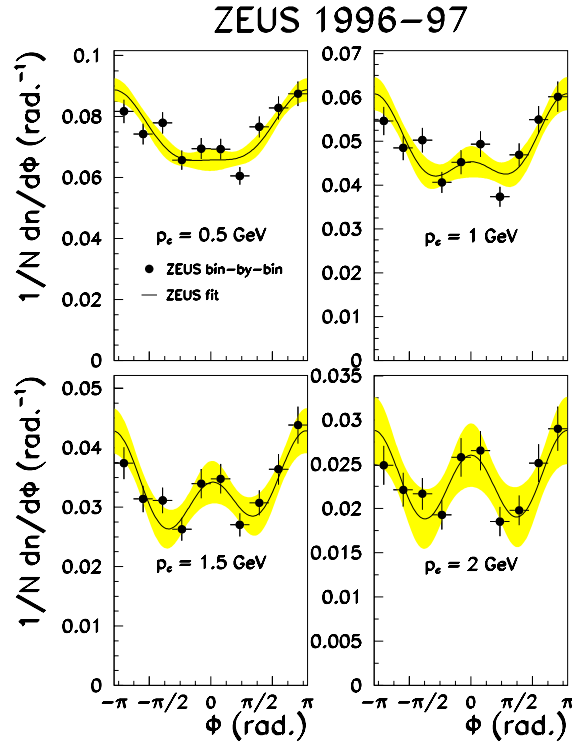


Figure 21: Azimuthal distribution of the leading charged particles for different requirements on the minimum transverse particle momentum p_c in the hadronic centre-of-mass frame.

of the matrix element in LEPTO leads to significant differences with the data. Calculations based on the LO matrix elements folded with fragmentation functions [103] lead to similar conclusions. It should be noted that the mean values for different minimum p_c are correlated since particles with large transverse momentum are contained in any bin. The measurement is dominated by statistical errors.

In conclusion, the azimuthal dependence of the LO matrix elements is confirmed, and significant azimuthal asymmetries as predicted by perturbative QCD are for the first time observed in DIS. No measurement of azimuthal dependence with jets or test of the NLO matrix elements has yet been performed. Modifications of equation (51) by terms proportional to $\sin \phi$ and $\sin 2\phi$ are expected for polarized leptons as will be available after the luminosity upgrade.

2.6 Three-jet events

Three-jet topologies have been studied in DIS at HERA in [106]. The jets are reconstructed with the inclusive k_T algorithm in the Breit frame. Each jet has to exceed a minimum transverse energy of $E_T^{Breit} > 5$ GeV and to satisfy $-1 < \eta^{lab} < 2.5$ to be within the acceptance of the H1 liquid argon calorimeter. For a given invariant mass of the three-jet system M_3 (and for massless jets), the topology of the jets can be fully characterised by five dimensionless variables. These can be chosen to be the energy fractions X_i of two of the jets, the angles θ_3 and Ψ_3 describing the

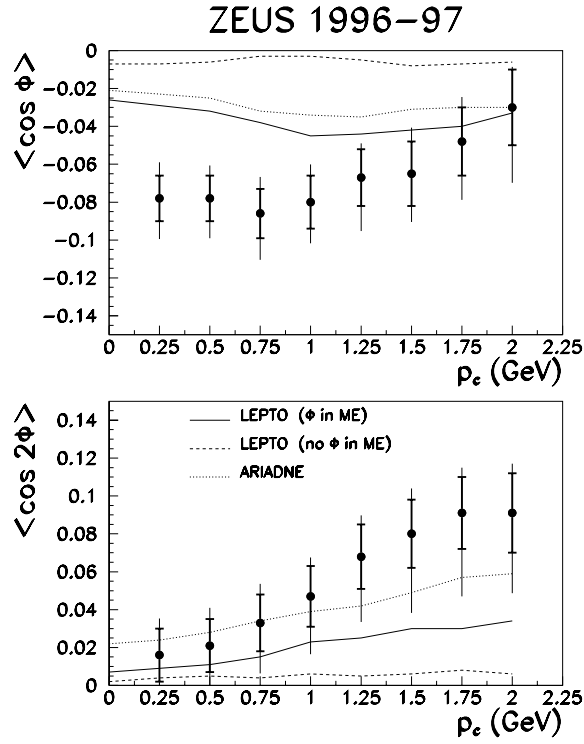


Figure 22: The mean values of $\cos \phi$ and $\cos 2\phi$ as a function of minimum transverse particle momentum.

orientation of the three-jet system with respect to the beam direction and an overall azimuthal angle [107] (see Figure 23):

- $X_i = 2E_i/M_3$, $i = 3, 4, 5$ where the index i denotes the three outgoing jets (partons) which are ordered in energy $E_3 > E_4 > E_5$. (The incoming parton and virtual boson are labeled $i = 1$ and 2.) Only two of these variables are independent due to the relation $X_3 + X_4 + X_5 = 2$.
- θ_3 is the polar angle of the most energetic jet with respect to the proton beam direction.
- The angle Ψ_3 describes the orientation of the jet plane with respect to the plane containing the proton beam and the most energetic jet. Ψ_3 is given by $\cos \Psi_3 = \frac{\mathbf{P}_3 \times \mathbf{P}_B \cdot \mathbf{P}_4 \times \mathbf{P}_5}{|\mathbf{P}_3 \times \mathbf{P}_B| |\mathbf{P}_4 \times \mathbf{P}_5|}$ where \mathbf{P}_B is the proton beam three-momentum and \mathbf{P}_i , $i = 3, 4, 5$ are the jet momenta. The value of Ψ_3 is strongly influenced by the least energetic jet. If this jet is radiated close to the plane defined by the beam and the highest energetic jet then $\Psi_3 \approx 0$ or $\Psi_3 \approx \pi$.

The data sample consists of two Q^2 ranges of $5 < Q^2 < 100 \text{ GeV}^2$ and $150 < Q^2 < 5000 \text{ GeV}^2$ collected in '97 and '95-'97, respectively. The selection criterion $0.2 < y < 0.6$ is always applied. In addition to the requirements on jet transverse energy $E_{T_{jet}}^{Breit}$ and η^{lab} , the three-jet mass must fulfil $M_3 > 25 \text{ GeV}$.

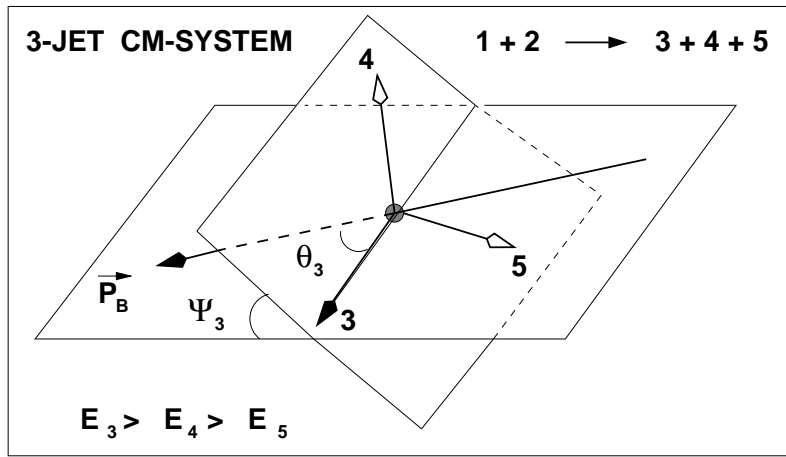


Figure 23: Definition of three-jet variables in the jet centre-of-mass system.

Perturbative QCD in LO (DISENT) gives a fair description of the Q^2 dependence of the three-jet cross section for Q^2 larger than $\approx 40 \text{ GeV}^2$ (see Figure 24). The deviations at small Q^2 are not surprising considering that the QCD prediction is in LO only.

The distribution of Ψ_3 is shown in Figure 25 for the low Q^2 sample. Here the additional cuts $|\cos \theta_3| < 0.6$ and $X_3 < 0.9$ are applied which reduce the strong influence of the jet selection criteria on the Ψ_3 distribution. The distribution is shape normalized and hadronization corrections are estimated to be smaller than 10%. The Ψ_3 distribution is well described by perturbative QCD in LO.

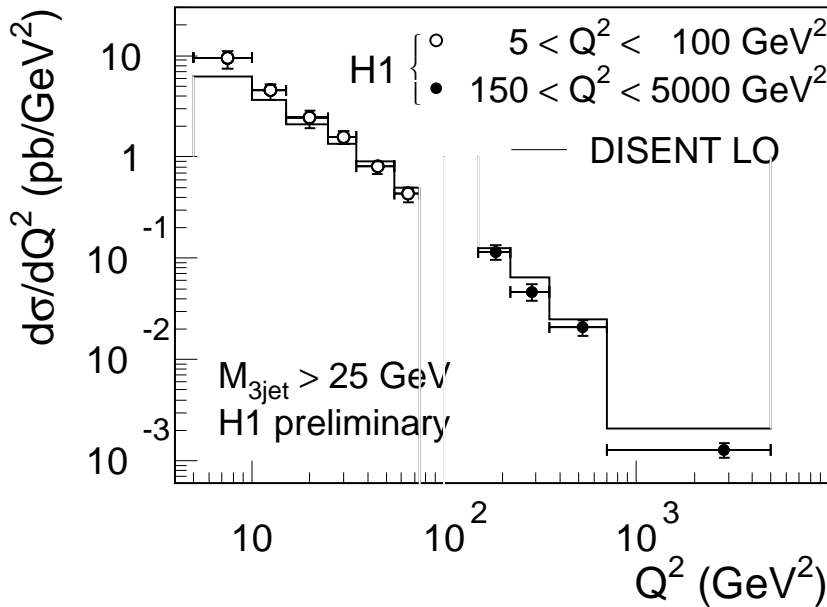


Figure 24: Three-jet cross section $d\sigma/dQ^2$ in the range of $5 < Q^2 < 5000 \text{ GeV}^2$ compared with perturbative QCD calculations in LO. Hadronization corrections are not applied. They lower the QCD prediction by 20-40%.

The largest phase space is available for configurations with $\Psi_3 \approx \pi/2$ where the least energetic jet is perpendicular to the plane containing the proton beam. Configurations where the least energetic jet is radiated close to the incoming parton are suppressed due to the requirement $E_{T\,jet}^{Breit} > 5$ GeV. The large difference of the perturbative QCD prediction and the phase space expectation shows that the distribution of Ψ_3 is strongly influenced by the QCD matrix elements.

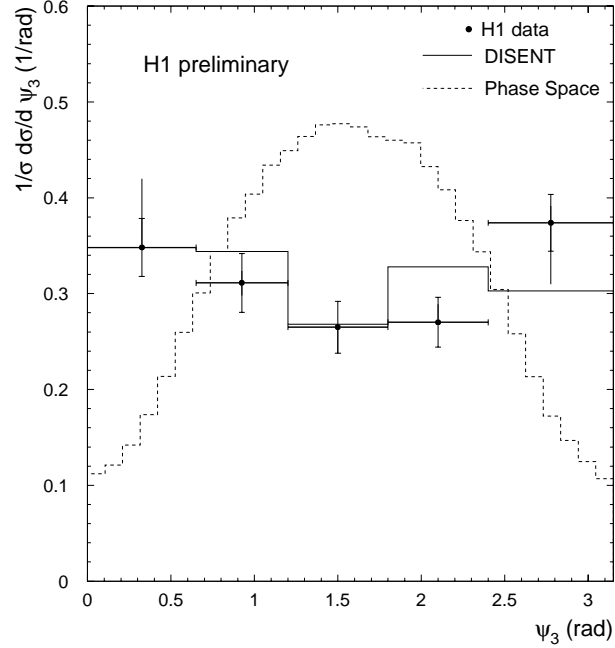


Figure 25: Three-jet distribution of Ψ_3 in the range $5 < Q^2 < 100$ GeV² compared with a perturbative QCD calculation in LO and a phase space prediction. Hadronization corrections are not applied.

3 Determination of the strong coupling constant α_s

Based on the good description of jet distributions by perturbative QCD, which was discussed above, the determination of the strong coupling α_s becomes possible. The precise determination of α_s is a major scientific goal of HERA. This is motivated by the following reasons:

- α_s is the only free parameter of QCD. Its value is much less well known than other fundamental couplings (see Table 3) which limits the precision of any perturbative QCD prediction.
- Comparison of α_s values determined from different processes e.g. e^+e^- annihilations, DIS or $p\bar{p}$ tests the consistency of QCD.
- Determination of α_s at different (energy) scales tests the renormalization scale dependence of the strong coupling.
- QCD corrections are important for precision tests of the electroweak sector of the standard model.

Various determinations of α_s based on jet or event shape variables have been performed at HERA [108, 109, 110, 111, 112, 113] and are discussed in the next sections.

interaction	coupling	value	uncertainty (ppm)
electromagnetic	α	1/137.0359895	0.045
weak	G_F	$1.16639 \times 10^{-5} \text{ GeV}^{-2}$	9
gravitational	G_N	$6.67259 \times 10^{-11} \text{ m}^3 \text{ kg}^{-1} \text{ s}^{-2}$	128
strong	$\alpha_s(M_Z)$	0.119	17000

Table 5: Coupling strength and relative uncertainty of the electromagnetic, weak, gravitational and strong interaction as given in [114].

3.1 Principle of α_s determination

Any collinear and infrared safe observable O which is sensitive to the value of α_s can in principle be used to determine α_s . The perturbative expansion for the differential cross section of O in DIS can be written in the form

$$d\sigma^{pert}/dO = \sum_n C_n \alpha_s^n = \sum_{q=u,d,s,\dots,g} \int_0^1 d\xi f_q(\xi, \mu_F) \sum_n c_{q,n} \alpha_s^n(\mu_R) \quad (52)$$

where the f_i are the parton densities at proton momentum fraction ξ and factorization scale μ_F . The C_n are the perturbative coefficients of order n . They depend on the parton density functions f_i whereas the coefficients $c_{q,n}$ are independent of f_q . For inclusive observables such as the

structure function F_2 , the leading contribution of the perturbative expansion is independent of α_s ($C_0 \neq 0$). In contrast, exclusive quantities such as the cross section of dijet events are proportional to α_s ($C_0 = 0$) which makes them directly sensitive to the value of α_s . Note that the leading coefficients do not depend on the renormalization scale while higher coefficients do.

Determination of α_s simply means finding the value α_s^{fit} for which $d\sigma^{pert}/dO(\alpha_s)$ describes the measurement best. In practice there are a number of complications due to:

- non-perturbative corrections such as hadronization to $d\sigma^{pert}/dO$;
- the renormalization scale dependence of $d\sigma^{pert}/dO$;
- the dependence of $d\sigma^{pert}/dO$ on the parton density functions.

The consequences of these effects and the resulting uncertainties are discussed in more detail below.

Hadronization

Perturbative QCD calculations are made for partons while experiments measure hadrons. Hadronization is irrelevant for inclusive observables like F_2 in DIS or R_Z , the ratio of the hadronic and muonic Z^0 decay width. It can, however, produce large effects for exclusive observables that must be considered. Hadronization effects may be estimated using

- (a) phenomenological fragmentation models
- (b) analytical parameterizations (power corrections).

The choice of (a) means that the observables of interest are calculated using QCD Monte Carlo models both with and without performing hadronization. The ratio of the resulting distributions is taken as hadronization correction.

The application of (b) is discussed in section 4.3.

Renormalization scale

The renormalization scale dependence is an artifact of the truncation of the perturbative series in finite order. The scale dependences are thus related to the size of *unknown* higher order corrections. In principle μ_R is arbitrary but there is common agreement that μ_R should be related to a physical energy scale in the scattering process. Best choices of μ_R have been suggested based on different theoretical arguments [115, 116, 117].

At HERA essentially Q^2 , $E_{T\ jet}$ or linear combinations of these have been used. Lacking a rigorous method to estimate the theoretical uncertainties related to any choice of μ_R , it became convention to vary the scale μ_R by factors of 1/2 and 2 and take the observed spread in $d\sigma^{pert}/dO$ as theoretical uncertainty. Significant improvements can only be expected once resummed calculations or calculations in next-to-next-to-leading order (NNLO) become available.

Parton density functions

The dependence of $d\sigma^{pert}/dO$ on the parton density functions f_i in DIS or in any collision with *hadrons* in the initial state leaves several choices:

- (a) The parton density functions derived from global fits to the world data are taken for the f_i . Then the strong coupling α_s is the only remaining unknown in equation (52) and can be fitted.
- (b) Both α_s and the parton density functions f_i are extracted simultaneously.
- (c) The value of the strong coupling is set to its world average value and the *parton densities* f_i are extracted instead. An example is given in section 4.5 where the gluon density at $x > 0.01$ is determined [131].

Method (a) was chosen in all determinations of α_s performed at HERA. The use of external parton density functions implies that data from other experiments influence the extracted α_s value. The groups CTEQ, GRV and MRST provide a number of different sets of parton density functions (PDF). Different data sets, fit procedures and values of the strong coupling α_s^{PDF} are used in their derivation. Measurements of α_s must consider the effect of these choices as systematic uncertainties. In particular, a possible correlation of the measured α_s value with α_s^{PDF} must be investigated.

Method (b) is the ideal choice which avoids most of the difficulties inherent to (a). Using data from a single experiment makes possible consistent treatment of systematic errors. In addition the correlation of α_s and the parton densities can be determined [118]. A larger set of distributions must be measured compared with (a) where only a single parameter $-\alpha_s-$ is to be determined. No analysis of this kind is published yet.

3.2 α_s from jet cross sections

Various determinations of α_s based on the measurement of jet cross sections or jet rates have been performed. These analyses essentially selected the kinematic range of Q^2 larger than 150 GeV² where hadronization effects and renormalization scale dependences are much reduced. In Table 6 an overview of the measurements is given. The latest (preliminary) results are presented in the subsections 3.2.1, 3.2.2 and 3.2.3. No HERA collaboration has yet determined α_s from structure function measurements. An early determination of α_s based on the ‘double asymptotic scaling’ properties of the gluon density at low x and high Q^2 has been presented in [120] using H1 F_2 measurements.

3.2.1 Single inclusive jet cross sections

H1 have measured the inclusive jet cross section as a function of Q^2 and $E_{T,jet}^{Breit}$ (see Figure 26) [121]. The measurement is based on the data collected in ‘95-‘97 corresponding to an integrated luminosity of $\approx 33 \text{ pb}^{-1}$. The kinematic region of $150 < Q^2 < 5000 \text{ GeV}^2$ and $0.2 < y < 0.6$ is selected. The jets are found with the longitudinally invariant k_T algorithm applied in the Breit frame. Only jets with $E_{T,jet}^{Breit} > 7 \text{ GeV}$ and $-1 < \eta^{lab} < 2.5$ are considered. Note that the reconstruction of a single jet with significant $E_{T,jet}^{Breit}$ is sufficient to select processes sensitive to the diagrams 6 (a) and (b) in leading order (see section 1.11). The fraction of DIS events with at least one accepted jet is $\approx 25\%$.

In a fit to all bins of Figure 26 using external parton densities, the strong coupling is determined to be

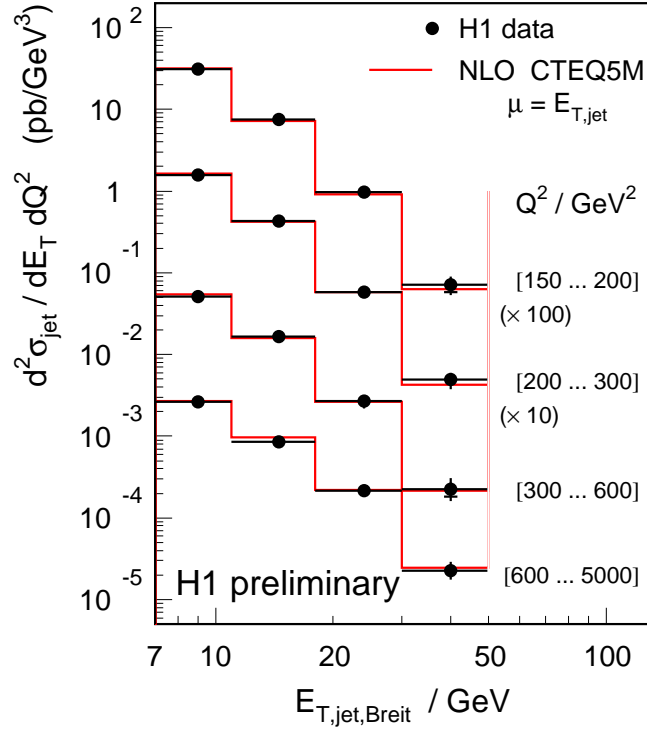


Figure 26: Inclusive jet cross sections as a function of $E_{T,jet}^{Breit}$ for different values of Q^2 .

$$\alpha_s(M_Z^2) = 0.1181_{-0.0030}^{+0.0030} (exp.)_{-0.0046}^{+0.0039} (theor.)_{-0.0015}^{+0.0036} (PDF)$$

for the choice $\mu_R = E_{T,jet}^{Breit}$ and

$$\alpha_s(M_Z^2) = 0.1221_{-0.0034}^{+0.0034} (exp.)_{-0.0059}^{+0.0054} (theor.)_{-0.0016}^{+0.0033} (PDF)$$

for the choice $\mu_R = Q$.

The dominant *experimental error* is caused by the hadronic energy scale uncertainty of the H1 liquid argon calorimeter which is 4% for jets⁷. The correlated uncertainty is 2%.

The *theoretical uncertainty* consists of the uncertainty of the hadronization corrections and the renormalization scale ambiguity which are of similar size. The hadronization corrections are small for the jet algorithm used and range between 3 and 10%. They are taken as the mean of the corrections predicted by the models ARIADNE, HERWIG and LEPTO. The renormalization scale uncertainty is estimated by varying the scale μ_R^2 to factors of 1/4 and 4 which changes α_s by $_{-0.0034}^{+0.0025}$ for $\mu_R = \langle E_{T,jet}^{Breit} \rangle$. The corresponding change for $\mu_R = Q$ of $_{-0.0049}^{+0.0044}$ is slightly larger.

The uncertainty related to the *parton density* has been determined considering all available parameterizations of the recent years. This is motivated by the relatively small spread of parton densities provided by the groups CTEQ, GRV and MRST compared with the larger variations between sets of parton densities of different years and different data sets. So far parton density

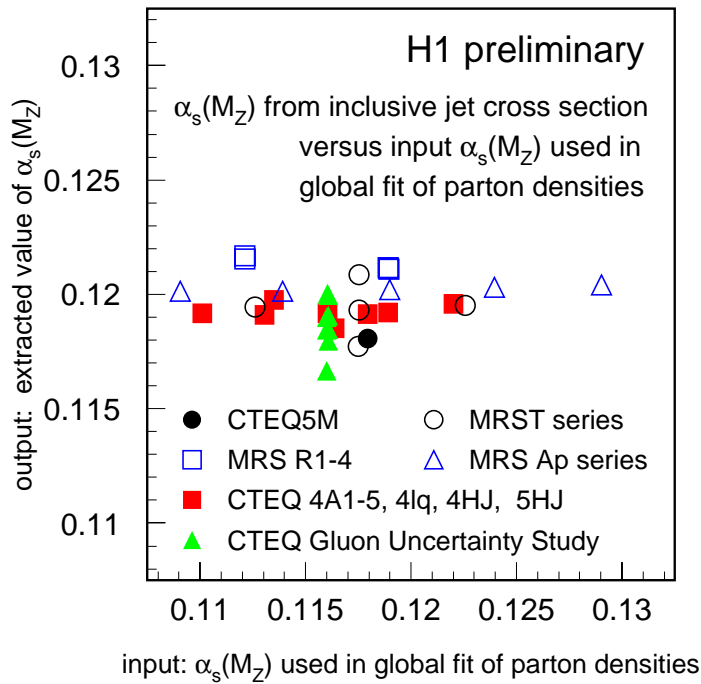


Figure 27: Correlation of α_s^{fit} with α_s^{PDF} .

functions with systematic error estimates have not been provided generally [123]. The influence of the parton densities on α_s is shown in Figure 27. It is remarkably small.

Renormalization scale dependence of α_s

The large range of Q^2 and $E_{T,jet}^{Breit}$ covered makes possible the investigation of the renormalization scale dependence of α_s . This proceeds in the following way: Given a choice of scale e.g. $\mu_R = E_{T,jet}$ and assuming a value of $\Lambda_{\overline{MS}}$ or $\alpha_s(M_Z)$, the prediction of $d\sigma^{pert}/dO = \sum_n C_n \alpha_s^n(\Lambda, \mu_R)$ is determined. A measurement of the cross section in a given bin of $E_{T,jet}$ is consequently probing the value of α_s in the range of $\alpha_s(E_{T,jet}^{min})$ and $\alpha_s(E_{T,jet}^{max})$.

Note that both choices of scale Q and $E_{T,jet}^{Breit}$ give a good description of the data. This suggests to test the running of α_s as a function of either scale! The results are shown in Figure 28. Both $\alpha_s(Q)$ and $\alpha_s(E_{T,jet}^{Breit})$ correspond to the dependence predicted by the renormalization group equation (RGE). The corresponding values of $\alpha_s(M_Z)$ calculated *using* the RGE are consistent with each other. The error bars in the figures include the scale variation of $1/4$ and $4\mu_R^2$ and are largely correlated.

This result represents an important test of QCD. Unfortunately the coverage in Q^2 or $E_{T,jet}^{Breit}$ can not be enlarged easily. At low Q^2 the NLO cross sections are large compared with the LO cross sections (the k factor is large), and the renormalization scale uncertainties increase. In addition the size of the hadronization corrections increases. Extending to larger Q^2 or $E_{T,jet}^{Breit}$ requires much more data while the gain is relatively small due to the flattening of the curve at large scales.

⁷In [28] a calibration uncertainty of 2% has been reached for inclusive DIS events.

The test of the renormalization scale dependence as a function of E_T^{Breit} , i.e. as a function of a variable related to the hardness of the parton radiation, is not restricted to DIS. The concept may as well be used in e^-e^+ annihilation.

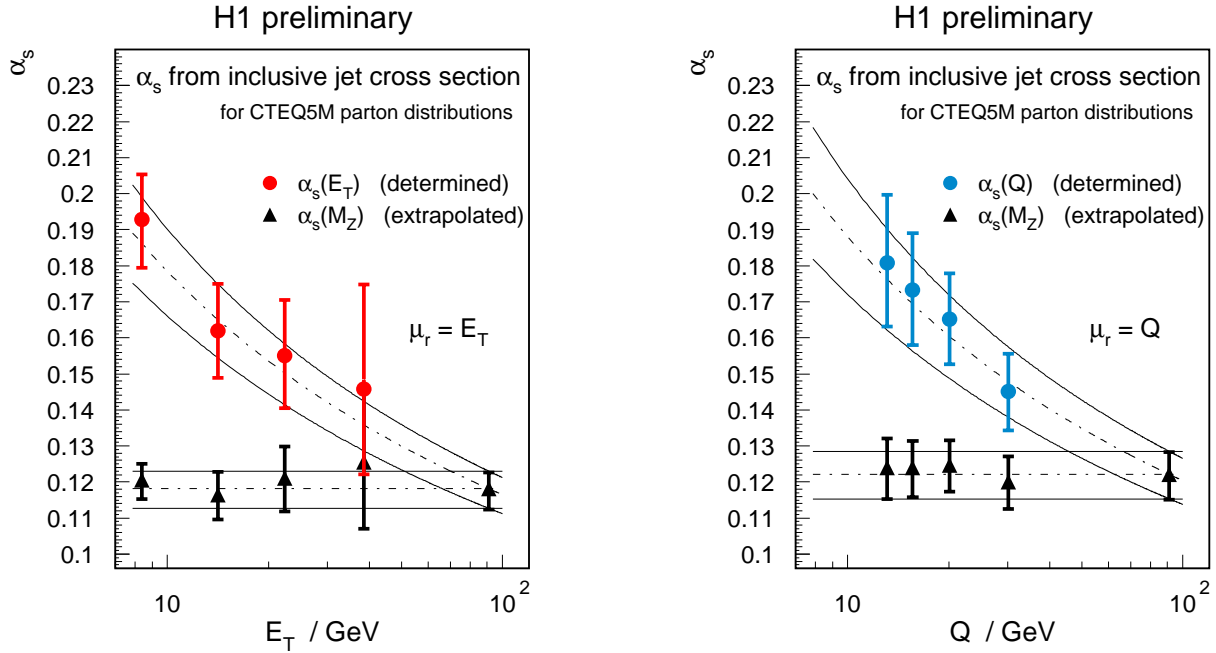


Figure 28: Renormalization scale dependence of α_s for either choice of scale $E_{T\ jet}$ or Q^2 .

3.2.2 Differential dijet event rates

In a different analysis H1 have determined the strong coupling with two additional jet algorithms, the factorizable k_T algorithm and the modified Durham algorithm, measuring the differential dijet rate $1/\sigma_{DIS}d\sigma_{dijet}/dy_2$ [94]. The analysis is essentially based on the same data sample as the analysis described above. Only the main results and the correlation of α_s with the parton densities are discussed below.

In the kinematic range of $575 < Q^2 < 5000$ GeV² H1 the strong coupling is determined to be

$$\begin{aligned}\alpha_s(M_Z^2) &= 0.1189_{-0.0081}^{+0.0064} (exp.) +_{-0.0046}^{+0.0059} (theor.) +_{-0.0055}^{+0.0013} (PDF) \\ \alpha_s(M_Z^2) &= 0.1143_{-0.0089}^{+0.0075} (exp.) +_{-0.0064}^{+0.0074} (theor.) +_{-0.0054}^{+0.0008} (PDF)\end{aligned}\quad (53)$$

for the factorizable k_T algorithm and for the modified Durham algorithm respectively.

The definitions of the two jet algorithms (and of the variables y_2) differ in many respects and it is a nice success of perturbative QCD that the values of α_s determined are similar. Note that the errors of the two α_s values are partly correlated.

Again it is important to investigate the correlation of the fit result with the value of α_s^{PDF} assumed in the parton density determinations. Thus the inclusive DIS cross section and the dijet

cross section in three different ranges of Q^2 are calculated with DISENT for a fixed value of $\alpha_s(M_Z)$, independent of α_s^{PDF} . The cross sections must be independent of α_s^{PDF} if there was no correlation between α_s^{PDF} and the parton density functions.

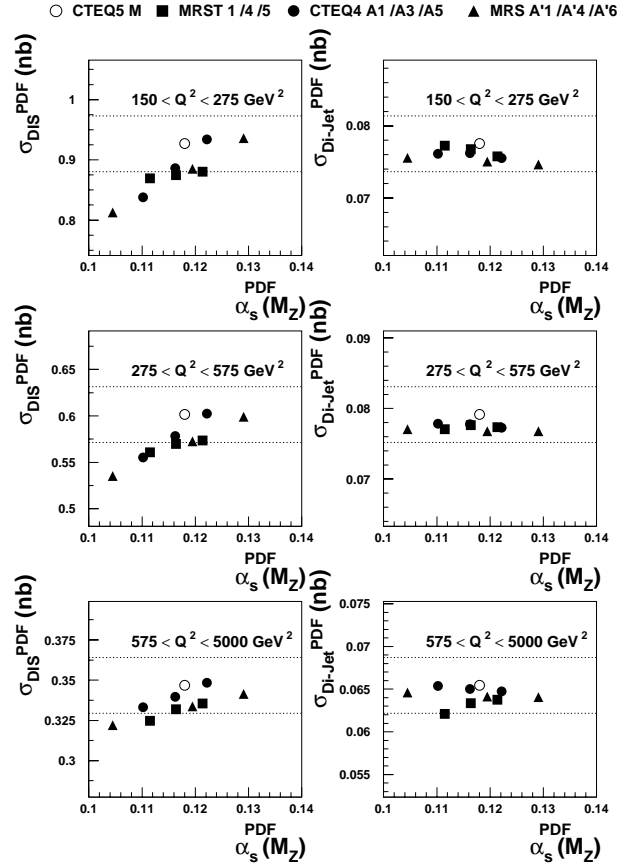


Figure 29: Inclusive DIS cross sections σ_{DIS} (left) and dijet cross sections σ_{dijet} (right) calculated in NLO for different sets of PDFs with different α_s^{PDF} . The dotted horizontal lines correspond to a deviation of $\pm 5\%$ from the CTEQ5M expectation.

The calculated *dijet* cross sections show no systematic dependence on α_s^{PDF} (see Figure 29). This corresponds to the results shown in Figure 27. In contrast, the *inclusive DIS* cross sections vary significantly with α_s^{PDF} for the CTEQ4A and MRSA' series of parton densities but vary significantly less for the MRST series. The dependence on α_s^{PDF} is largest in the lowest Q^2 range and decreases at high Q^2 . The large dependence of the inclusive DIS cross sections on α_s^{PDF} is counter-intuitive since the inclusive DIS cross section is independent of α_s in LO. In addition the differences between the different series may surprise. These observations stress the need for a consistent determination of parton densities and α_s in combined fits with full consideration of correlated errors.

The results given in (53) are determined from measurements of jet cross sections normalized by the inclusive DIS cross section. The dependence of the inclusive DIS cross section on α_s^{PDF}

leads to an increased PDF uncertainty compared with the measurement presented in section 3.2.1.

3.2.3 Dijet event rates $R_{2+1}(Q^2)$

ZEUS have measured dijet cross sections and the dijet event rate $R_{2+1}(Q^2)$ with data collected in 1996-97 in the range of $470 < Q^2 < 20,000 \text{ GeV}^2$ [122]. They use the longitudinally invariant k_T algorithm. The analysis is similar to previous jet analyses and again a good description of the data by QCD in NLO is obtained. The strong coupling is determined from a fit to the measured $R_{2+1}(Q^2)$ shown in Figure 30 with a set of NLO predictions based on the series of PDFs with different α_s^{PDF} .

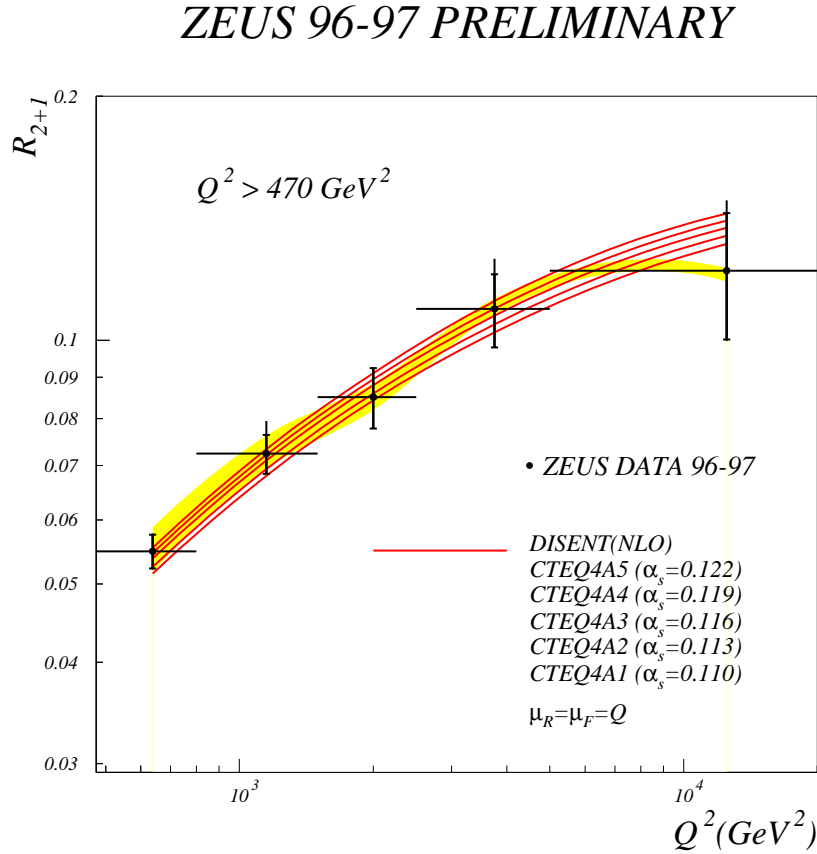


Figure 30: Dijet rate $R_{2+1}(Q^2)$ compared with NLO predictions for the CTEQ4A PDF series.

For the respective calculations of R_{2+1} , α_s is always consistently set to α_s^{PDF} . The fit value is obtained from an interpolation of the resulting NLO predictions. Thus the correlation of PDFs and α_s is consistently considered.

ZEUS obtain

$$\alpha_s(M_Z^2) = 0.120_{-0.003}^{+0.003} (stat.)_{-0.006}^{+0.005} (exp.)_{-0.002}^{+0.003} (theor.) . \quad (54)$$

Unfortunately not all global fits provide series of PDFs with different α_s assumptions. Thus the number of parton densities included in the theoretical error is smaller than that above. The renormalization scale was varied from $\mu_R^2 = Q^2$ to $\mu_R^2 = 1/2 Q^2$ and $\mu_R^2 = 2 Q^2$ (instead of the factors 1/4 and 4) which explains the smaller theoretical error compared with the results above.

3.3 Event shape distributions and test of power corrections

A meaningful comparison of hadronic final state observables with the corresponding perturbative QCD predictions requires the determination of hadronization effects. An approach alternative to the use of phenomenological fragmentation models is the calculation of analytical power corrections to the perturbative QCD predictions without modelling all the details of hadronization. Such corrections of the order of $1/Q^p$ are related to the higher-order behaviour of perturbation theory [124] or to the presence of a universal effective coupling α_{eff} at low momentum scales [125]. In the latter approach a non-perturbative parameter $\bar{\alpha}_{p-1}$ with

$$\bar{\alpha}_{p-1}(\mu_I) = \frac{p}{\mu_I^p} \int_0^{\mu_I} dk_T k_T^{p-1} \alpha_{eff}(k_T)^{p-1} \quad (55)$$

is introduced. The parameter $\bar{\alpha}_{p-1}$ parameterizes the behaviour of α_s below a certain infrared matching scale μ_I where the perturbative expression of $\alpha_s(\mu_R)$ diverges (see section 1.3). The infrared matching scale must fulfil $\Lambda_{QCD} \ll \mu_I \ll Q$ and is taken to be 2 GeV below. In the model of Dokshitzer and Webber the power corrections arise through the contribution of very soft gluon radiation which can be calculated for a given event shape variable. Meanwhile the leading power p and the exact form of the power corrections to the mean values of event shape distributions have been calculated for a large number of observables in both e^+e^- annihilation and deep-inelastic scattering. The mean value of a event shape variable F is given by

$$\langle F \rangle = \langle F \rangle^{pert} + \langle F \rangle^{pow} . \quad (56)$$

The purely perturbative contribution $\langle F \rangle^{pert}$ has the form of equation (52) and can be calculated using the NLO programs mentioned above.⁸ $\langle F \rangle^{pow}$ is predicted to be

$$\langle F \rangle^{pow} = a_F \frac{4C_F}{p\pi} M \left(\frac{\mu_I}{Q} \right)^p \left[\bar{\alpha}_{p-1}(\mu_I) - \alpha_s(Q) - \frac{\beta_0}{2\pi} \left(\ln \frac{Q}{\mu_I} + \frac{K}{\beta_0} + \frac{1}{p} \right) \alpha_s^2(Q) \right] \quad (57)$$

where $K = 67/6 - \pi^2/2 - 5/9 N_f$, with $N_f = 5$. The Milan factor M accounts for two-loop effects and is given by [126, 127]

$$M = \frac{2}{\pi} \left(1 + \frac{1.575 C_A - 0.104 N_f}{\beta_0} \right) . \quad (58)$$

The size of the power correction $\langle F \rangle^{pow}$ depends on the event shape variable, on the value of $\bar{\alpha}_{p-1}$, on the strong coupling constant α_s and, of course, on Q . DIS at HERA with its large coverage of Q is the ideal place to test the concept of power corrections.

⁸In practice, the programs based on the phase-space slicing method cannot be used because the contribution from $F \rightarrow 0$ cannot be calculated for realistic values of the phase-space slicing parameter.

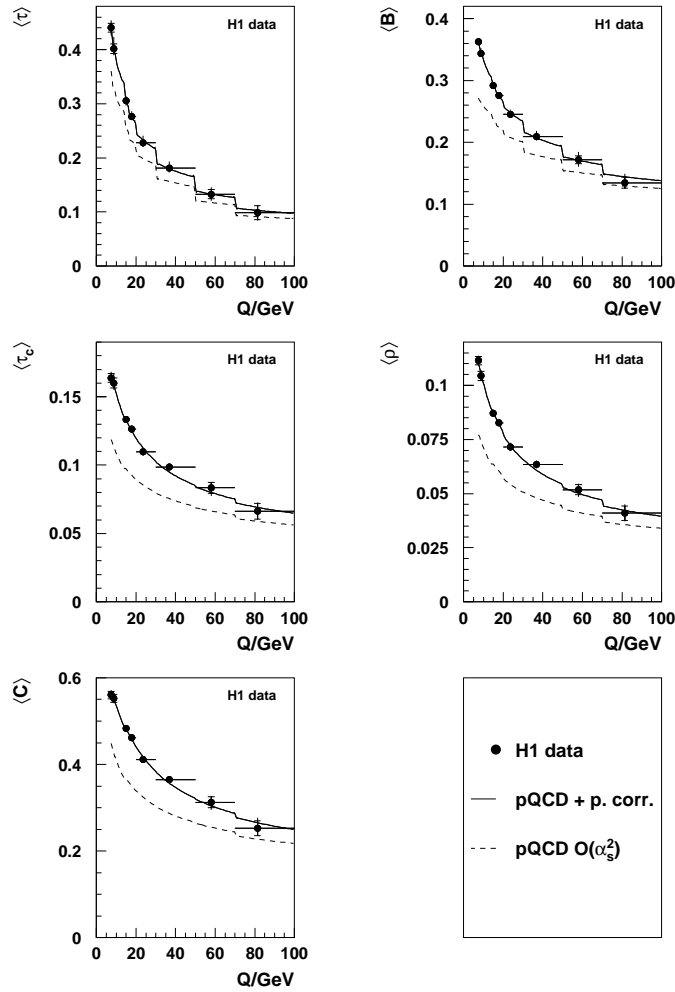


Figure 31: Mean values of event shape distributions compared with perturbative QCD calculations combined with power corrections fitted to the data.

H1 have investigated power corrections using data collected in ‘94-‘97 corresponding to an integrated luminosity of 38 pb^{-1} [113]. The event shape distributions of two definitions of thrust $\tau = 1 - T_Z$ and $\tau_C = 1 - T_C$, jet broadening B_c , C parameter, scaled jet mass ρ and of the minimum jet distances y_2 determined with the factorizable JADE and k_T jet algorithms are measured in the kinematic range of $7 < Q < 100 \text{ GeV}$.⁹ The mean values of selected variables are shown in Figure 31. In particular at low Q they are measured with high precision. For the variables shown the power $p = 1$. Consequently the power corrections tend to be large. Smaller power corrections are observed (not shown) for the factorizable k_T algorithm where the leading power is predicted to be $p = 2$.

The value α_s and $\bar{\alpha}_0$ ($p = 1$) is determined in two-dimensional fits of equation (56) to the measured mean values. Perturbative QCD in NLO in conjunction with the fitted power corrections describes the data well (see Figure 31). Perturbative QCD in NLO alone is clearly incompatible with the data. This is best visible at low Q where the power corrections are

⁹The definitions of the variables are given in section 1.9.

largest. Less sophisticated parameterizations of power corrections such as $\langle F \rangle^{pow} = c/Q$ or $\langle F \rangle^{pow} = c/Q^2$, where c is a constant, are excluded by the data [113].

The fitted α_s and $\bar{\alpha}_0$ are shown in Figure 32. They are determined with high experimental precision for most observables. The choice of the parton density functions has a marginal effect on the results. The values of $\bar{\alpha}_0$ are consistent with a single *universal* value of $\bar{\alpha}_0 = 0.5$ within $\pm 20\%$. The spread of the $\alpha_s(M_Z)$ values is uncomfortably large, however, and the values of $(\alpha_s, \bar{\alpha}_0)$ of various observables disagree within their experimental errors.

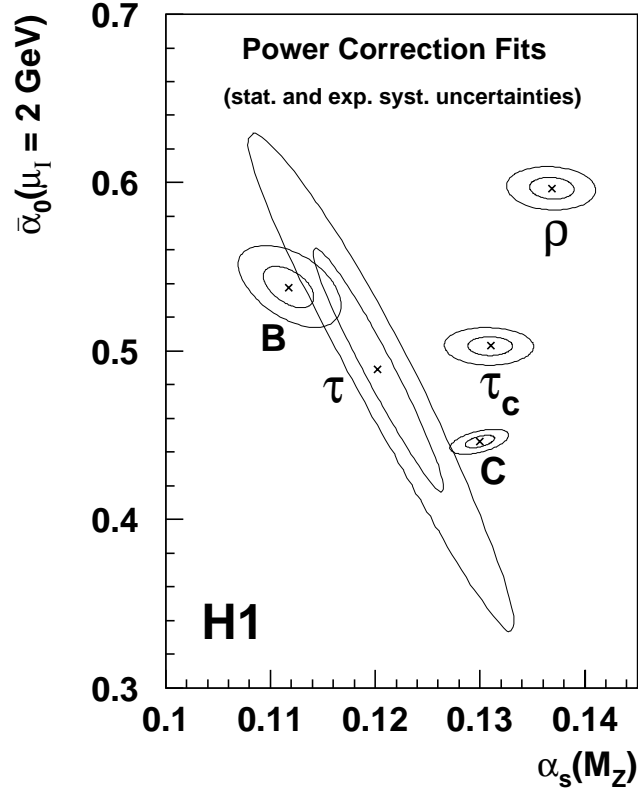


Figure 32: Values of $\alpha_s(M_Z)$ and $\bar{\alpha}_0$ from power correction fits for different event shape variables. The circles correspond to the 1- σ and 2- σ contours of the experimental errors.

There are several possible explanations for these discrepancies. The effect of unknown *higher order corrections* to the perturbative QCD prediction of $\langle F \rangle^{pert}$ may be large. This is suggested by the large renormalization scale dependences on the event shape variables. These dependences are much larger than those of the jet cross sections presented above where tight event selection criteria are applied. (It should be noted that in [113] μ_R^2 is varied by factors of 1/2 and 2 instead of the more conventional 1/4 and 4 in order to fulfil the condition $\Lambda_{\overline{MS}} \ll \mu_I \ll \mu_R$.) Varying the infrared matching scale μ_I between 1.5 and 2.5 GeV has a small effect on α_s compared with the renormalization scale dependence. Of course, the discrepancies may also suggest further refinement of the applied power correction model.

Summarizing the investigation of power corrections it can be stated: The basic concept of power corrections is supported by the data. The description of the data by an economic

model with only one free non-perturbative parameter $\bar{\alpha}_0$ is a major success. It promises deeper understanding of the interplay of perturbative and non-perturbative QCD. Further theoretical progress is, however, needed to evaluate the validity of power corrections properly.

A direct comparison of the fitted analytical power corrections with the hadronization corrections derived from fragmentation models seems natural but has not yet been performed.

3.4 Overview of α_s measurements at HERA

An overview of the α_s measurements performed at HERA is given in Table 6.¹⁰ Only analyses based on the measurements of jet event rates or jet cross sections are listed. The analyses of α_s using power corrections are not included since currently the theoretical uncertainties related to this method are difficult to estimate and further rapid development in this field is to be expected.

$\alpha_s(M_Z)$	$\Delta\alpha_s(M_Z)$			observable	Q^2 [GeV ²]	$\int \mathcal{L}$ [pb ⁻¹]	reference
	exp.	theor.	PDF				
0.123 ± 0.018	± 0.015	± 0.009	± 0.005	$R_{2+1}(Q^2)$	100 – 4000	0.3	[108]
0.117 ± 0.009	$+0.004$ -0.005	± 0.007	± 0.001	$R_{2+1}(Q^2)$	120 – 3600	3	[109]
$0.118^{+0.011}$ -0.010	± 0.008	$+0.007$ -0.006	$+0.005$ -0.002	y_2	200 – 10 000	7	[110]
0.117 ± 0.01	$+0.007$ -0.006	± 0.008	$+0.003$ -0.002	$R_{2+1}(Q^2)$	40 – 4000	9	[111]
0.122 ± 0.007	± 0.003	$+0.005$ -0.006	$+0.003$ -0.002	$\frac{d^2\sigma_{jet}}{dE_T dQ^2}$	150 – 5000	33	[121]
$0.119^{+0.009}$ -0.011	$+0.006$ -0.008	$+0.006$ -0.005	$+0.001$ -0.006	y_2	575 – 5000	33	[94]
0.120 ± 0.007	$+0.007$ -0.006	$+0.003$ -0.002	–	$R_{2+1}(Q^2)$	470 – 20 000	38	[122]

Table 6: α_s determinations in DIS at HERA. The last three results are preliminary.

Seen from today’s perspective the first pioneering determinations of α_s [108, 109] at HERA were clearly hampered by the small data samples available and by the fact that the first NLO programs made approximations that were imprecise. The analyses [110, 111] are much improved in many respects. Their dominant errors are caused by the renormalization uncertainty and the model dependence of the detector corrections. These analyses used the NLO program MEPJET which is not the favoured choice today.¹¹

The preliminary results discussed in the previous subsections benefit from data samples increased by factors of five. This makes possible the determination of α_s from two-dimensional distributions e.g. jet cross sections as a function of Q^2 and E_T^{Breit} . In addition, the increased data samples led to an improved understanding of the calibration of the calorimeters thus reducing a major experimental uncertainty. The phase space regions of large scales can be selected which leads to a significant reduction of the renormalization scale dependence. The development of

¹⁰Only a subset of the preliminary results is shown.

¹¹Using DISENT instead of MEPJET in [110] changes the extracted value of $\alpha_s(M_Z)$ by -0.003 .

additional NLO programs and their systematic comparisons gives confidence in the correctness of the NLO predictions used in the analyses.

The main limitations of the current α_s determinations are the renormalization scale dependence, the uncertainty of the parton density functions and the possible correlation of the extracted value of α_s with α_s^{PDF} . The renormalization scale dependence is likely to be reduced further by selecting processes at even higher Q^2 and $E_{T\ Breiit}$ when the large data samples expected after the luminosity upgrade are available. The correlation with the parton density functions will be overcome by combined fits of α_s and the parton densities using the techniques to be discussed in the next section.

Alternatively a fundamental reduction of the renormalization scale dependence at lower values of Q^2 could be achieved by theoretical progress. The advent of resummed calculations, as available in e^+e^- annihilation, for realistic jet selection criteria should allow also the huge data samples at $Q^2 < 100\ \text{GeV}^2$ to be fully exploited.

4 Determination of parton densities

The main motivation to determine the parton densities instead of α_s from hadronic final state measurements is the poor knowledge of the gluon density at large momentum fractions ξ compared with the uncertainty of α_s . The gluon density is strongly decreasing with increasing ξ , and at large ξ the structure function measurements in DIS at HERA start to be less sensitive to the gluon density. Selection of events with two jets in the final state gives direct access to the gluon density through boson-gluon-fusion. Similarly identification of charm quarks in the final state through reconstruction of D^* mesons produced by gluon induced $eg \rightarrow ec\bar{c}$ processes enhances the sensitivity to the gluon density greatly. These two methods have been applied at HERA and the results are presented below.

4.1 Fitting techniques

Typical parameterizations of parton density functions depend on four or five parameters for each parton species. In order to determine these parameters in multi-dimensional fits of dijet cross sections, perturbative QCD predictions in NLO must be calculated repeatedly for various parameter values. This creates a major practical difficulty since NLO calculations are time consuming. Two sophisticated techniques to overcome these difficulties have been developed: (a) *fits in Mellin space* [129] and (b) *fits using a discrete set of eigenfunctions in x -space* [118, 130]

(a) Mellin transform technique

The Mellin transform $\tilde{F}(n)$ of a function $F(x)$ is defined by

$$\tilde{F}(n) = \int_x^1 \frac{dx}{x} x^n F(x) \quad (59)$$

where n is a complex number. The convolution of parton density functions and the partonic cross sections simplifies to a series of products (for each n) in Mellin space

$$\sigma = \sum_q \int_x^1 \frac{d\xi}{\xi} f_q(\xi) C_q\left(\frac{x}{\xi}\right) \quad \Leftrightarrow \quad \tilde{\sigma}(n) = \sum_q \tilde{f}_q(n) \tilde{C}_q(n) \quad (60)$$

where σ and $\tilde{\sigma}$ are the (jet) cross section in x -space and Mellin space, respectively. The index q corresponds to different parton species $u, d, \dots, \bar{u}, \bar{d}, \dots, g$.

Given the $\tilde{\sigma}(n)$, σ can be regained by an inverse Mellin transform

$$\sigma = \frac{1}{2\pi i} \int_{c-i\infty}^{c+i\infty} dn x^{-n} \tilde{\sigma}(n) \quad (61)$$

where the real number c has to be chosen appropriately. In practice the integral can be evaluated numerically and only a limited number of moments $\tilde{\sigma}(n)$ needs to be known.

The time-consuming repeated calculations of the σ for different parton density functions is avoided by calculating the coefficients \tilde{C}_q once and for all. The transformations of the parton densities $f_q(\xi)$, the evaluation of the $\tilde{\sigma}(n)$ according to the right hand side of (60) and the inversions are fast. The $\tilde{f}_q(\xi)$ can be evolved in Mellin space using the parton evolution program of [128].

(b) Eigenfunction technique in x -space

In this approach the parton density functions $f_q(\xi)$ are approximated by a sum over a discrete set of values ξ_i multiplied by the corresponding eigenfunctions $E_i(\xi)$:

$$f_q(\xi) \approx \sum_i f_q(\xi_i) E_i(\xi) . \quad (62)$$

The perturbative expansion of the cross section σ given in equation (52) can then be expressed as

$$\sigma = \sum_{q,n} \int_x^1 d\xi f_q(\xi) c_{q,n} \alpha_s^n \approx \sum_{q,n,i} f_q(\xi_i) \alpha_s^n \int_x^1 d\xi E_i(\xi) c_{q,n} = \sum_{q,n,i} f_q(\xi_i) \alpha_s^n A_{q,n,i} . \quad (63)$$

The $A_{q,n,i}$ have to be calculated using a NLO program. Once they are determined the cross section σ can quickly be evaluated for a given set of parton density functions according to the right-hand side of equation (63). Two examples of eigenfunctions which were used for the extraction of the gluon density are cubic splines [130] and triangular functions [118].

4.2 Gluon density from dijet events

H1 have determined the gluon density from measurements of differential dijet cross sections in the range of $200 < Q^2 < 5000 \text{ GeV}^2$ and $0.2 < y < 0.6$ [131]. The jets are found with the longitudinally invariant k_T algorithm. The transverse jet energies have to satisfy $E_{T,jet}^{Breit} > 5 \text{ GeV}$ each and $E_{T1}^{Breit} + E_{T2}^{Breit} > 17 \text{ GeV}$. The angular jet acceptance is restricted to $-1 < \eta^{lab} < 2.5$. The double-differential cross sections $d^2\sigma/dQ^2 d\xi$ where $\xi = x \cdot (1 + m_{12}^2/Q^2)$ and $d^2\sigma/dQ^2 dx$ are used in the fit.

In particular the ξ distribution is directly sensitive to the ξ dependence of the parton densities and not to the overall fraction of gluon-induced events only. The distribution of ξ in different Q^2 ranges is shown in Figure 33. The values of ξ where the cross section is sizeable extend from 10^{-2} to 10^{-1} approximately (for $Q^2 > 200 \text{ GeV}$). The hadronization corrections to the dijet cross sections are taken as the mean value from ARIADNE, HERWIG and LEPTO. They are less than 10%. H1 have used both techniques (a) and (b) to extract the gluon density.

In the analysis based on method (a) [119], $d^2\sigma/dQ^2 dx$ is combined with inclusive DIS cross section measurements [132] in the kinematic range of $20 < Q^2 < 5000 \text{ GeV}^2$. The u

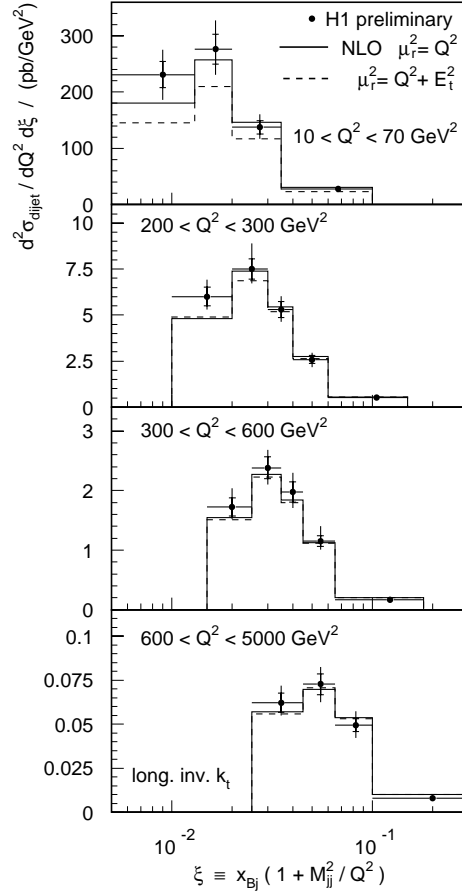


Figure 33: Dijet cross section $d^2\sigma/dQ^2d\xi$ compared with QCD predictions in NLO.

valence quark, gluon and combined sea quark distributions at the starting scale $Q_0^2 = 4 \text{ GeV}^2$ are parameterized as

$$xf(x, Q_0^2) = A_f x^{\lambda_f} (1-x)^{\beta_f} . \quad (64)$$

The d valence distribution is assumed to be correlated with the u valence distribution and further assumptions on the strange quark densities are made. Parton evolution is performed in Mellin space. The u and d valence quark sum rules and the momentum sum rule are applied. The value of the strong coupling is set to $\alpha_s(M_Z) = 0.119 \pm 0.003$. The fits consistently consider the correlation of the systematic experimental errors. Note that only H1 data are used in the fit.

The extracted gluon density (labeled “ $F_2 + \text{dijets, massless Mellin}$ ”) is shown in Figure 34. The precision of the gluon density is high. A fit including only the inclusive DIS cross section (labeled “ $F_2, \text{massless Mellin}$ ”) is fully consistent with the combined fit. The uncertainty of the fits with and without inclusion of the dijet cross sections is very similar. This is because the number of bins is much larger for the inclusive DIS cross section than for the dijet cross section.

In a second analysis based on method (b) [118], the dijet cross sections $d^2\sigma/dQ^2d\xi$ and $d^2\sigma/dQ^2dx$ are combined with the inclusive DIS cross section measurements [132] restricted to the kinematic range of $200 < Q^2 < 650 \text{ GeV}^2$ and $0.005 < x < 0.65$. This restriction

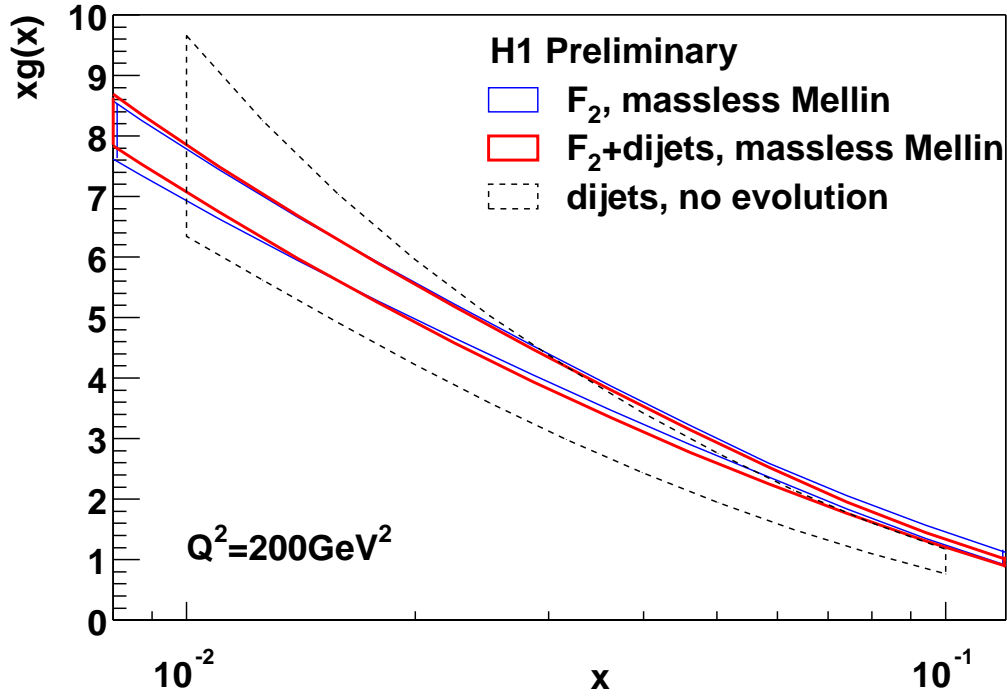


Figure 34: Gluon density at large momentum fractions determined using dijet and F_2 measurements.

puts more weight on the dijet measurement than the previous analysis. Here only the linear combination $\Delta(\xi) = \sum_q e_q^2 [q(\xi) + \bar{q}(\xi)]$ and the gluon density $g(\xi)$ is fitted which greatly reduces the number of fit parameters. No parton evolution is performed and the factorization scale is set to a fixed value of $\mu_F^2 = 200 \text{ GeV}^2$. This value is close to the average Q^2 of the inclusive event sample and to the average $E_{T,jet}^2$ of the dijet events. No constraints due to sum rules are made. The renormalization scale is set to $\mu_R^2 = Q^2$ for the inclusive cross sections and to $\mu_R^2 = Q^2 + \langle E_T^2 \rangle$ for the dijet cross sections. The value of the strong coupling is set to $\alpha_s(M_Z) = 0.119 \pm 0.005$.¹²

The resulting gluon density is also shown in Figure 34 (labeled “dijets, no evolution”). It is in excellent agreement with the gluon density discussed above while its systematic error is considerably larger. This is due to the much smaller range of the inclusive DIS cross section considered and due to the larger uncertainty assumed for α_s . The dominant error sources of the measurement are the hadronic energy scale uncertainty of the H1 liquid argon calorimeter, the renormalization scale uncertainty and the error of α_s .

These results are an important step on the way to combined fits of α_s and the parton density functions. While the first analysis fully exploits the power of theoretical constraints, very few assumptions are made in the second analysis which thus is more transparent. The extracted gluon density is relevant e.g. for the interpretation of large E_T jet production in $p\bar{p}$ collisions.

¹²For historical reasons the uncertainty of $\alpha_s(M_Z)$ is assumed to be $\Delta\alpha_s = \pm 0.005$.

4.3 Gluon density from D^* events

Both H1 and ZEUS have measured $D^{*\pm}$ cross sections in DIS [134, 135]. D^* mesons are almost entirely produced in gluon-induced processes $\gamma^{(*)}g \rightarrow c\bar{c}$. Their production cross section is thus sensitive to the gluon density of the proton and can be used to test perturbative QCD calculations.

The ZEUS analysis is based on data collected in '96-'97 corresponding to an integrated luminosity of 37 pb^{-1} . The kinematic range of the measurement is $1 < Q^2 < 600 \text{ GeV}^2$ and $0.02 < y < 0.7$. The decay channels $D^{*+} \rightarrow D^0 \pi_s^+ \rightarrow (K^- \pi^+ \pi_s^+)$ or $(K^- \pi^+ \pi^- \pi_s^+)$ and charge conjugates are selected. Only central drift chamber tracks in the polar angular range of $-1.75 < \eta < 1.75$ with transverse momentum of $p_T > 75 \text{ MeV}$ and a corresponding track reconstruction efficiency above 95% are included in the analysis. The D^* reconstruction is based on requirements on the track momenta of K and π candidates, the momentum ratio of the D^0 and slow pion π_s , the mass of the D^0 candidate and the mass difference ΔM of D^* and D^0 candidates. The corresponding mass distributions are shown in Figure 35. The D^* signal consists of ≈ 2000 and ≈ 1300 events in the $K2\pi$ and $K4\pi$ channel respectively.

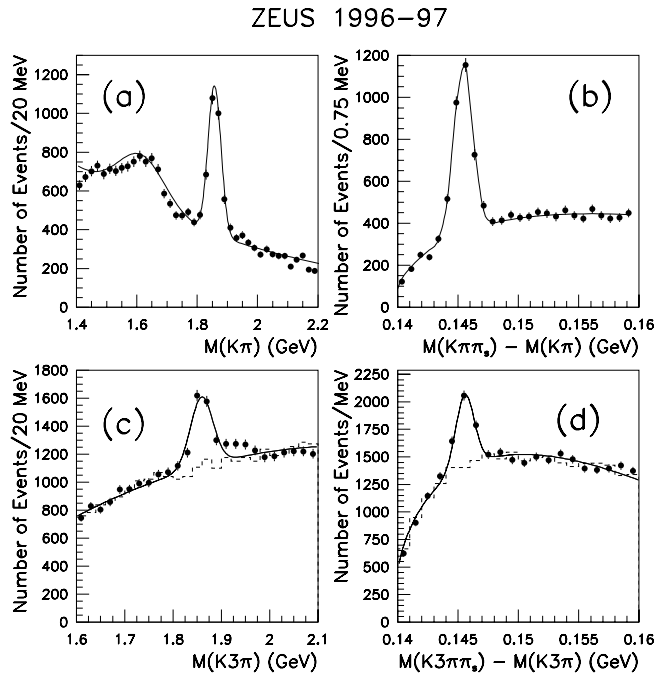


Figure 35: Examples of reconstructed D^0 mass and ΔM distributions from $D^* \rightarrow K2\pi$ (top) and $D^* \rightarrow K4\pi$ (bottom).

The D^* cross sections measured for the decay channel $D^0 \rightarrow K2\pi$ with $1.5 < p_T(D^*) < 15 \text{ GeV}$ and $|\eta(D^*)| < 1.5$ is

$$\sigma_{vis}(e^+p \rightarrow e^+D^{*\pm}X) = 8.31 \pm 0.31(stat.) {}^{+0.30}_{-0.50}(syst.) \text{ nb} . \quad (65)$$

The cross section for $D^0 \rightarrow K4\pi$ with $2.5 < p_T(D^*) < 15$ GeV and $|\eta(D^*)| < 1.5$ is

$$\sigma_{vis}(e^+p \rightarrow e^+D^{*\pm}X) = 3.65 \pm 0.36(stat.) {}^{+0.20}_{-0.41}(syst.) \text{ nb} . \quad (66)$$

The differential cross sections as a function of the kinematic variables and of the D^* transverse momentum $p_T(D^*)$, pseudorapidity $\eta(D^*)$ and momentum fraction $x(D^*)$ are compared with NLO predictions in Figure 36. The NLO predictions are obtained with the program HVQDIS [136] based on parton density functions determined from ZEUS and fixed target experiment data [133]. The charm quark mass m_c is assumed to be 1.4 GeV and the fragmentation function of RAPGAP is taken. The choice of m_c , of the fragmentation function and of the hadronization fraction $f(c \rightarrow D^{*+})$ each lead to systematic uncertainties of the prediction.

Although the data tend to be shifted towards larger $\eta(D^*)$ and smaller $x(D^*)$, the measurement roughly agrees with the expectation of perturbative QCD in NLO (full line). This shows the consistency with the gluon density measurements in inclusive processes.

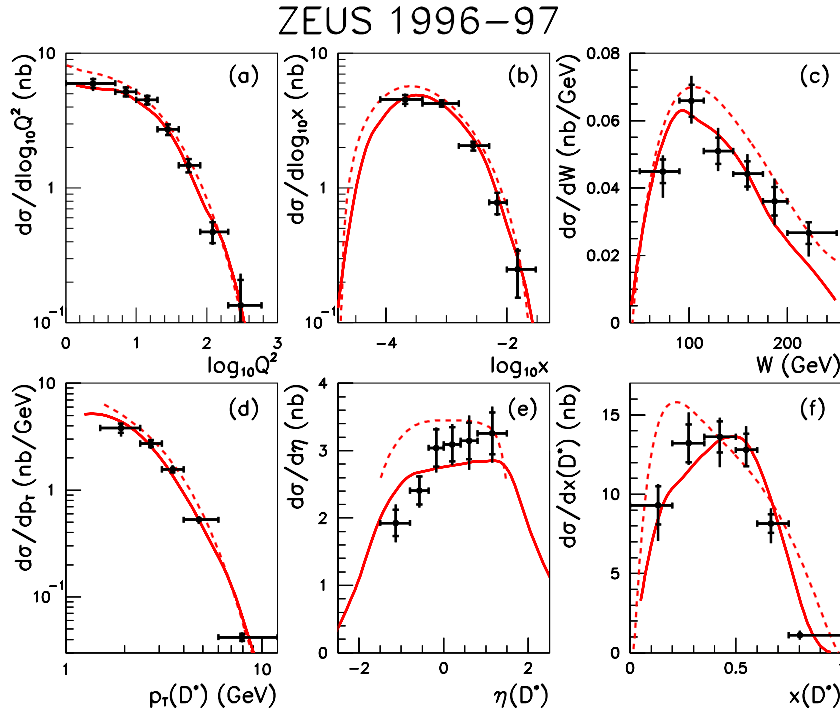


Figure 36: Differential D^* cross sections compared with NLO predictions.

ZEUS proceeds to extract the charm contribution $F_2^{c\bar{c}}$ to the structure function F_2 [135]. $F_2^{c\bar{c}}$ is defined by

$$\frac{d^2\sigma_{DIS}^{c\bar{c}}}{dx dQ^2} = \frac{2\pi\alpha^2}{Q^4 x} \{ [1 + (1-y)^2] F_2^{c\bar{c}}(x, Q^2) - y^2 F_L^{c\bar{c}}(x, Q^2) \} . \quad (67)$$

This corresponds to the definition of F_2 with σ_{DIS} replaced by $\sigma_{DIS}^{c\bar{c}}$, the cross section for the interaction of a virtual photon with a charm quark or antiquark.

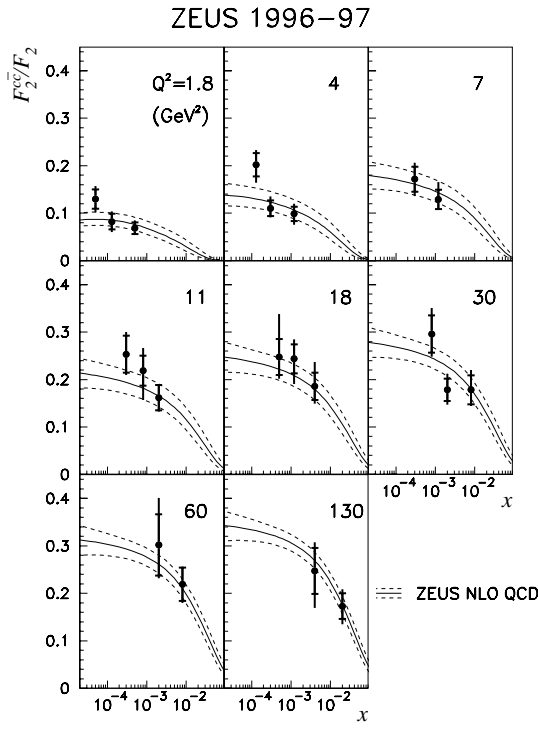


Figure 37: Ratio of $F_2^{c\bar{c}}$ and F_2 compared with predictions based on the parton densities extracted from F_2 [133].

The extraction of $F_2^{c\bar{c}}$ from the visible cross sections σ_{vis} requires the extrapolation to the full $p_T(D^*)$ and $\eta(D^*)$ range. This is performed using HVQDIS with the fragmentation function of RAPGAP. The extrapolated cross sections are much larger than the visible ones, and the extrapolation crucially relies on the correct data description by perturbative QCD in NLO outside the range of measurement. The contribution of $F_2^{c\bar{c}}$ to F_2 is roughly 10% at low Q^2 and can be as large as 30% at large Q^2 (see Figure 37).

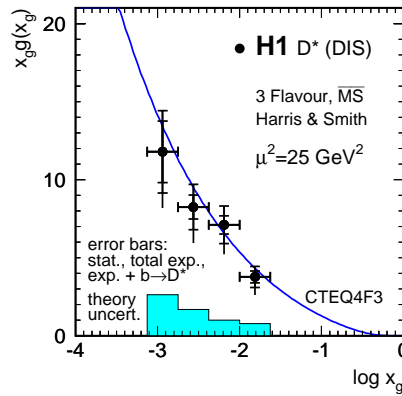


Figure 38: Gluon density from measurement of D^* cross sections.

H1 has extracted the gluon density from their D^* measurements [134]. The measurement is based on data collected in '95-'96 corresponding to an integrated luminosity of 9.7 pb^{-1} . The fit procedure is less involved than those discussed for jet distributions above. The quark-induced cross section is calculated with HVQDIS and is subtracted from the observed cross sections. The differential cross section are measured as a function of the variable x_g^{OBS} which is related to the momentum fraction of the incoming gluon. The gluon density $x g(x)$, determined using an iterative unfolding technique, is shown in Figure 38. It agrees well with that of [137] and other determinations within errors.

Further improvement of charm quark analyses in DIS largely rely on larger data samples due to higher luminosity and/or improved triggering on heavy quark events. Joint reconstruction of D^* and jets is desirable improving the resolution of x_g . In addition to reconstructing D^* mesons, high p_T leptons from semileptonic decays may be used to tag heavy quarks.

5 Test of parton evolution equations

One of the first striking results of HERA was the observation of the strong rise of the proton structure function F_2 at small x [138] corresponding to a large increase of the parton density in the proton. This stimulated the investigation of parton evolution equations alternative to DGLAP. In particular the BFKL equation which resums logarithms of $\ln(1/x)$ has raised much attention. With the increasing precision of structure function measurements and the extension of the kinematic range to $x \approx 10^{-5}$ it became apparent that *inclusive* F_2 measurements at HERA are fully compatible with DGLAP evolution (see Figure 11). In order to enhance the sensitivity to BFKL signatures dedicated measurements of the hadronic final state have been performed. The main observables are *transverse energy flow, charged particle transverse momentum spectra, dijet event rates, forward jet cross sections, inclusive forward charged particle and forward π^0 cross sections.*

The measurements are confronted with predictions based on *DGLAP evolution* as provided by the QCD models HERWIG, LEPTO, RAPGAP or by perturbative QCD calculations in NLO. *Alternative* approaches are represented by:

- analytical calculations based on BFKL evolution
- QCD programs based on CCFM evolution (CASCADE or LDC)
- the colour dipole model (ARIADNE)
- QCD models or perturbative NLO calculations with a resolved virtual photon (RAPGAP/HERWIG, JETVIP)

The measurements concentrate on the region of low x and Q^2 but frequently extend to larger x and Q^2 where DGLAP evolution is still expected to be valid. Ideally the onset of BFKL or related signatures is noticed as a deviation from the DGLAP predictions when x and Q^2 is decreased. Simultaneously the data description of the alternative models under investigation should improve.

5.1 E_T flow

The average transverse energy E_T in the angular region between the proton remnant and the struck (current) quark is expected to be larger if the parton cascade is not ordered in k_T as is assumed in the BFKL evolution. Various measurements of the E_T flow as a function of pseudorapidity in different ranges of x and Q^2 have been performed [139]. LO calculations of the average E_T as a function of x assuming DGLAP or BFKL evolution are available [140].

The comparison of these calculations with the measurements requires the knowledge of hadronization effects. These are found to be large and to be very model dependent [69]. Thus measurement of transverse energy flow does not discriminate between different parton evolution schemes. It has led to restrictions of MC model parameters instead [141, 142].

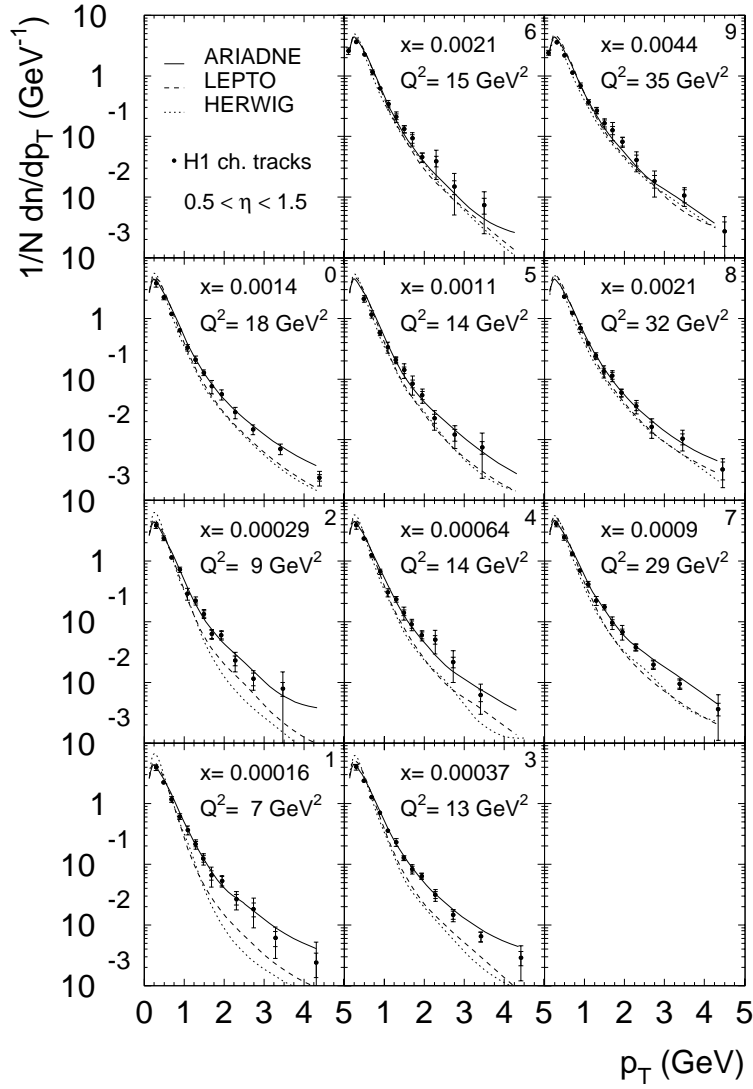


Figure 39: Charged particle transverse momentum spectra in different ranges of Q^2 and x .

5.2 Charged particle p_T spectra

Particles with large transverse momentum p_T are expected to originate from hard QCD radiation and are unlikely to be produced in the hadronization process. Charged particle p_T was proposed in [143] as an observable more sensitive to parton evolution than transverse energy flow.

H1 have measured charged particle p_T distributions in different ranges of x and Q^2 [144]. The measurement is based on the data collected in '94 corresponding to an integrated luminosity of 1.3 pb^{-1} . The kinematic range of the measurement is $5 < Q^2 < 50 \text{ GeV}^2$. The tracks are measured in the H1 forward and central tracking detectors. The minimal track length required is 10 cm. The track finding efficiency for particles with $p_T^{lab} > 0.15 \text{ GeV}$ exceeds 93% for central tracks. The dominant experimental errors are due to the variation of the track selection cuts and due to the model dependence of the acceptance corrections.

In Figure 39 the measured spectra are compared with QCD model predictions. The models LEPTO and HERWIG based on DGLAP evolution underestimate the number of high p_T particles at small x and Q^2 but fit the data for x larger than ≈ 0.002 . ARIADNE describes the data in the full kinematic range. An excellent description of these distributions is also obtained by CASCADE based on the CCFM equation (not shown) [71]. This suggests that deviations from DGLAP evolution have been seen.

A calculation based on the BFKL equation in conjunction with π^\pm and K^\pm fragmentation functions [145] describes the data well [146], and evidence for BFKL evolution has been claimed. Given that the calculation is based on BFKL in LO (without consistency constraint) and that its normalization is approximated by a fit to measured forward jet distributions, this conclusion now seems premature. An exact calculation based on the NLO matrix elements combined with fragmentation functions is not yet available.

5.3 Dijet cross sections at low Q^2 and large $E_{T\ jet}$

Measurements of dijet cross sections at low Q^2 have provided further indication that DGLAP parton evolution may be insufficient. As an example the dijet rate $R_2(Q^2)$ measured by H1 [147] is shown in Figure 40 in the range of $5 < Q^2 < 100 \text{ GeV}^2$. The measurement is based on the data collected in '94 corresponding to an integrated luminosity of 2 pb^{-1} . The jets are found with a cone algorithm. The minimum jet transverse energy is 5 GeV while the sum of the jets' transverse energies must exceed 13 GeV.

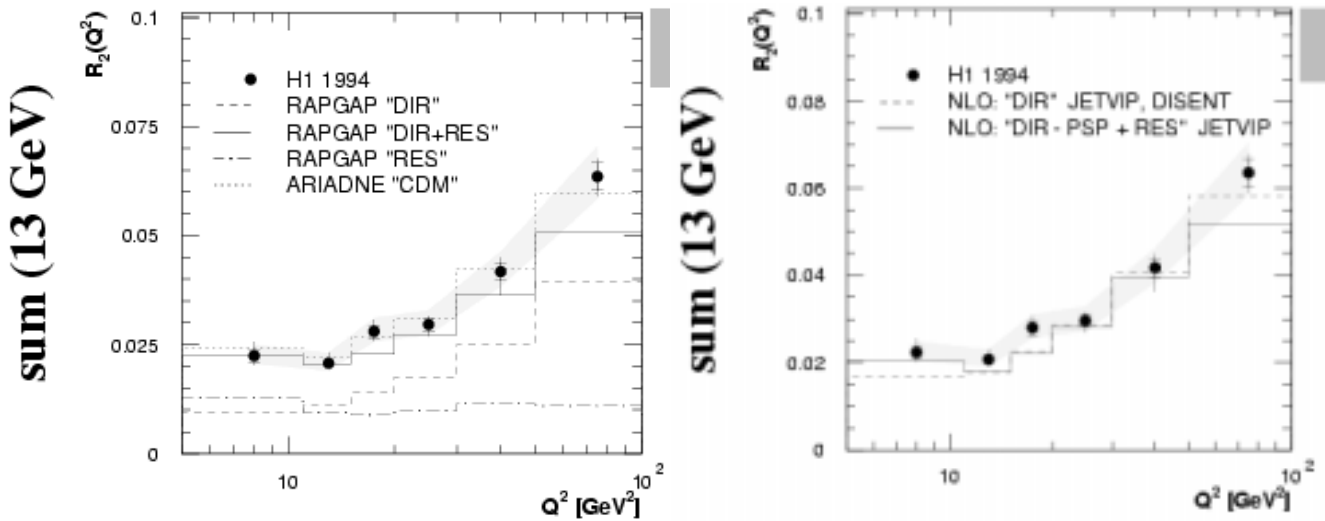


Figure 40: Dijet rates R_2 as a function of Q^2 compared with QCD models (left) and with perturbative QCD in NLO (right).

Again the data are not described by QCD models based on DGLAP parton showers (represented by the curve RAPGAP "Dir") while ARIADNE describes the data well. Including

processes with a resolved virtual photon (RAPGAP “DIR+RES”) improves the agreement of RAPGAP.

In Figure 40 (right) $R_2(Q^2)$ is compared with perturbative QCD predictions in NLO. DIS-ENT provides a fair description of the data. The calculations based on JETVIP (labeled “DIR-PSP+RES”) includes the contribution of a resolved virtual photon. In the range of this measurement the two NLO predictions are very similar. The agreement of the direct NLO calculation (DIS-ENT) with the data can be understood from Figure 41. The NLO matrix element which is considered by DIS-ENT (left) effectively corresponds to the convolution of the LO matrix element with the photon splitting term of the photon density function (middle) as contained in RAPGAP. Similarly the convolution of the NLO matrix element with the photon density function (right) as contained in JETVIP may effectively approximate the NNLO direct matrix element.

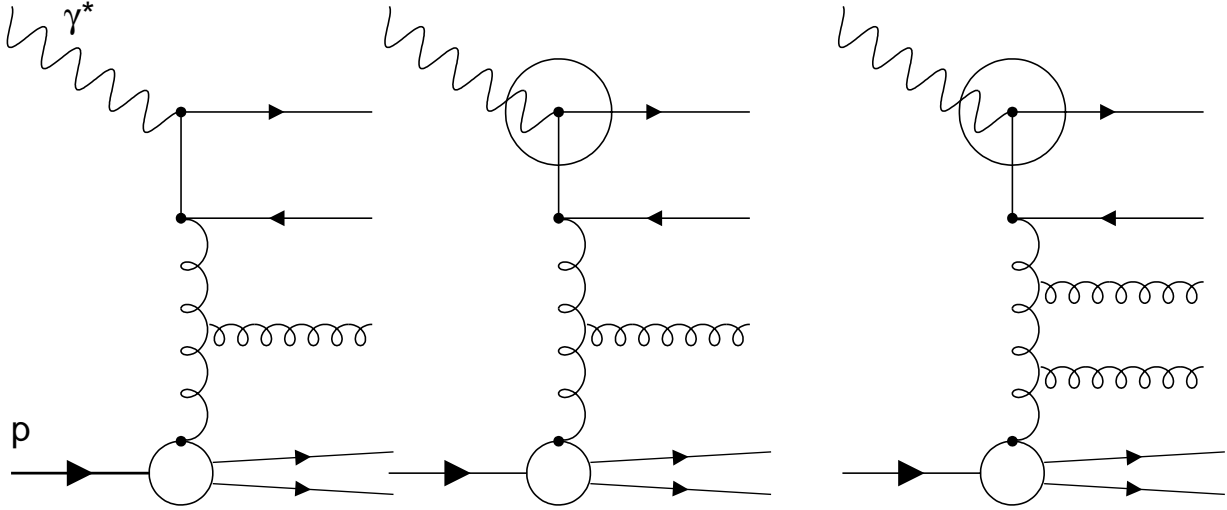


Figure 41: NLO diagram without photon structure $\gamma^* g \rightarrow q\bar{q}g$ (left), LO diagram with photon structure $\bar{q}g \rightarrow \bar{q}g$ (middle) and NLO diagram with photon structure $\bar{q}g \rightarrow \bar{q}gg$ (right).

Both H1 and ZEUS have performed dedicated measurements to provide direct evidence for virtual photon structure [148, 149]. H1 have measured the triple differential dijet cross section as a function of Q^2 , mean transverse jet energy squared $\overline{E}_{T,jet}^2$ and x_γ . The variable x_γ is related to the photon’s momentum fraction entering the hard scattering. It is reconstructed from the jets’ four-momenta. The measurement is based on data collected in ‘96 corresponding to an integrated luminosity of 6 pb^{-1} . The jets are reconstructed with the inclusive k_T algorithm. The kinematic range of the measurement is $1.6 < Q^2 < 80 \text{ GeV}^2$ while $\overline{E}_{T,jet}^2 > 30 \text{ GeV}^2$.

The distribution of x_γ in different regions of Q^2 and $\overline{E}_{T,jet}^2$ is shown in Figure 42. In any of the histograms a clear peak of the cross section at $x_\gamma \approx 1$ is seen. This corresponds to the interaction of a direct photon with a proton constituent. Significant contributions to the cross section at values of $x_\gamma \ll 1$ are expected if the photon has a structure and only the momentum carried by one of its partons enters the scattering process. Contributions at low x_γ are indeed observed whenever $\overline{E}_{T,jet}^2 \gg Q^2$. The data distributions are well reproduced by QCD models

incorporating virtual photon structure (HERWIG/DG) while models without it (HERWIG/DIR) only describe the region of large x_γ .

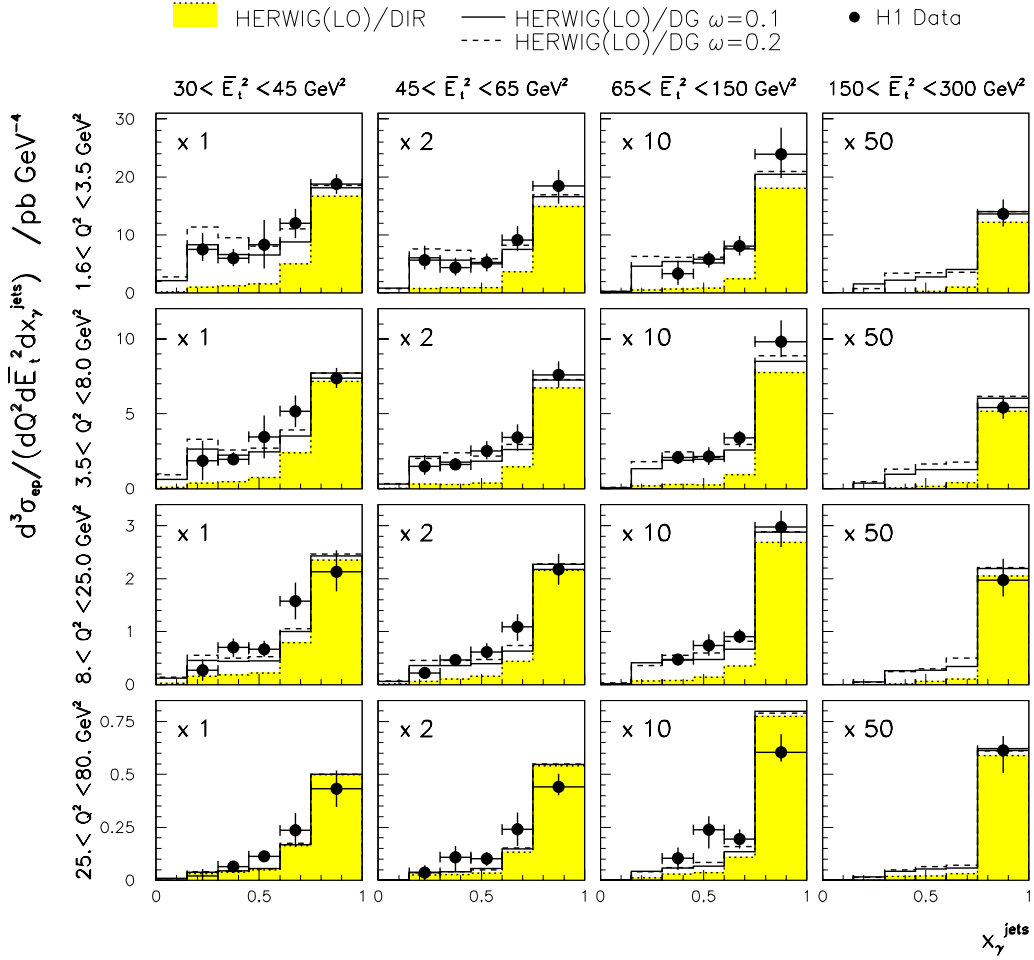


Figure 42: Triple differential dijet cross sections at low Q^2

5.4 Forward jet production

The cross section for jet production in the forward (proton) direction has been proposed as a measure sensitive to parton evolution in [150]. Applying the selection criteria

$$k_{T,jet}^2 \approx Q^2 \quad \text{and} \quad x_{jet} \gg x \quad (68)$$

the phase space region with gluons strongly-ordered in transverse momentum $Q^2 = k_{T,n}^2 \gg k_{T,n-1}^2 \gg \dots \gg k_{T,1}^2$ is suppressed, leading to increased sensitivity to BFKL dynamics.

Several measurements of forward jets are available [151, 152]. The measurement of ZEUS is shown in Figure 43. It is based on a data sample of 6.5 pb^{-1} collected in '95. The jets are reconstructed with a cone algorithm in the laboratory frame. The jets' transverse energy must

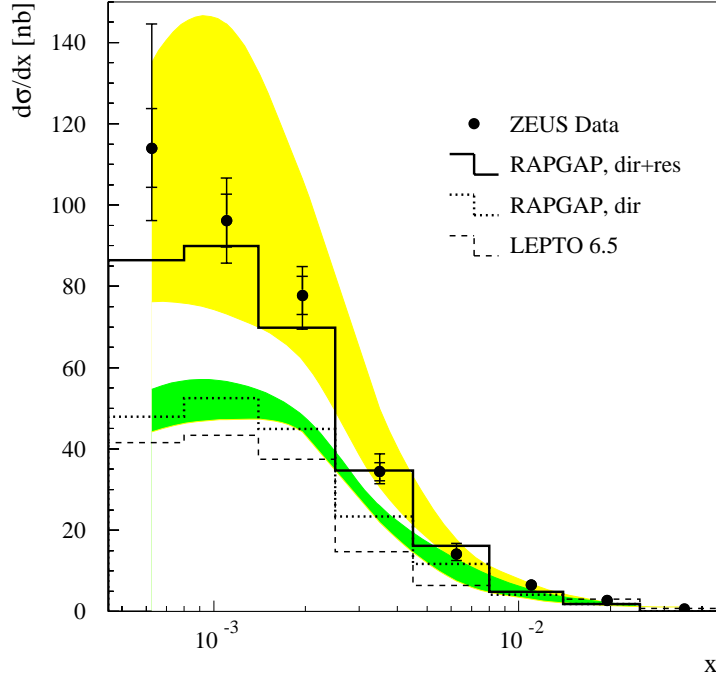


Figure 43: Forward jet cross section as a function of x . The shaded bands correspond to the factorization scale uncertainty.

exceed 5 GeV. The kinematic region is defined by $Q^2 > 10 \text{ GeV}^2$ and $2.5 \cdot 10^{-4} < x < 8 \cdot 10^{-2}$. It is required that $x_{jet} = p_{Z jet}/p_{proton} > 0.036$ and $0.5 < E_{T jet}^2/Q^2 < 2.0$, thus satisfying the condition (68). The measurement is experimentally challenging. Both detector acceptance and resolution are relatively low and the tight cuts lead to small cross sections.

Models like HERWIG, LEPTO and RAPGAP with $O(\alpha_s)$ matrix elements and DGLAP parton shower evolution again disagree with the data. They predict too small a forward jet cross section at low x . This is also valid for perturbative QCD calculations in NLO which were able to describe the dijet rate $R_2(Q^2)$ presented earlier. The data are described by: ARIADNE and by RAPGAP including resolved photon contributions [154]; by perturbative QCD in NLO with resolved virtual photon contribution as available in JETVIP; by calculations based on the LO BFKL equations modified to include sub-leading terms (consistency constraint) [37]. (Note that not all predictions mentioned are shown in the Figure.)

ZEUS have also measured the distribution of $E_{T jet}^2/Q^2$ without imposing the constraint $0.5 < E_{T jet}^2/Q^2 < 2.0$ (see Figure 44). This distribution is a particular challenge for QCD models since very different phase space regions are covered at the same time. Only RAPGAP with resolved virtual photon and JETVIP describe the data in the full range of $E_{T jet}^2/Q^2$.

Summarizing, it is a major achievement that several sophisticated theoretical approaches have meanwhile been developed that describe the forward jet cross sections. It must be kept in mind that the uncertainty of the predictions and that of the measurement are considerable. In some of the comparisons hadronization corrections are not included.

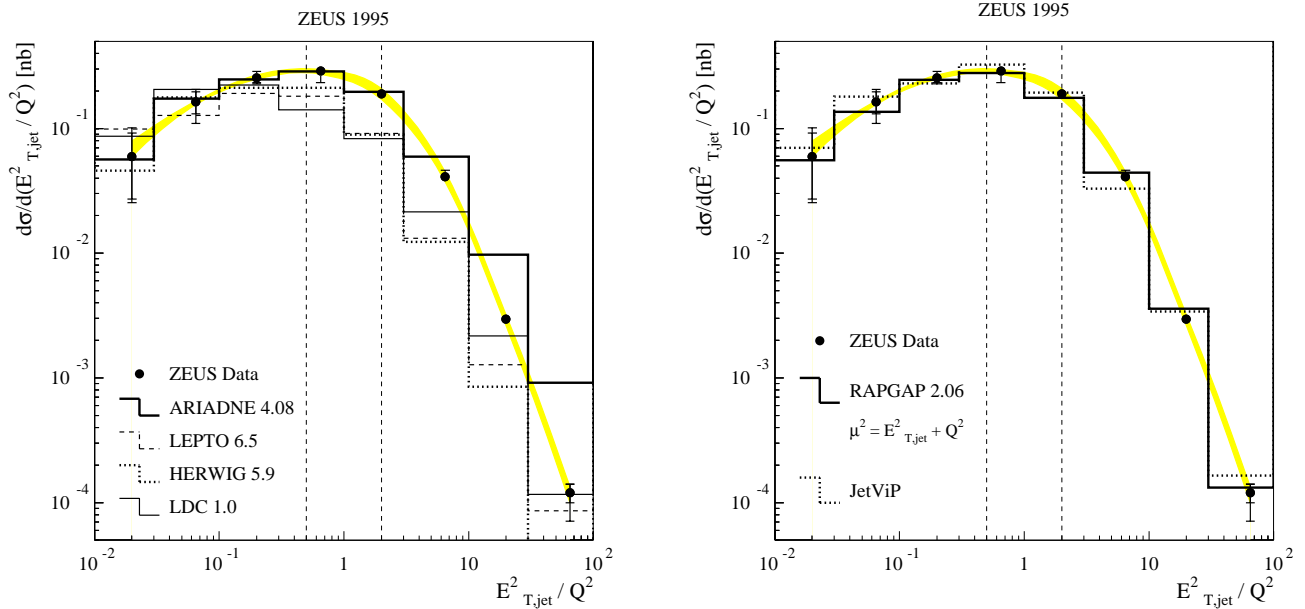


Figure 44: Forward jet cross section as a function of E_T^2 / Q^2 . The shaded bands correspond to the uncertainty of the energy scale of the calorimeter.

Further measurements with forward jets have been proposed. The distribution of the azimuthal angle between the forward jet and the scattered electron was suggested to discriminate between BFKL and DGLAP evolution (azimuthal decorrelations) [156]. The azimuthal distribution has been measured but its shape is roughly reproduced by all QCD models suggesting that this observable is less sensitive to parton evolution than expected [152]. In addition the study of the azimuthal angle between the jets in dijet events at small x was proposed and calculations exist [155]. Since no (preliminary) data are yet available this method is not discussed here.

5.5 Forward π^0 production

Inclusive forward pion cross sections as a function of x , Q^2 , transverse momentum and pseudorapidity have been measured by H1 [157]. The measurement is based on the data collected in '96 corresponding to an integrated luminosity of 5.8 pb^{-1} . The π^0 candidates are selected in a polar angular region of $5^\circ < \theta_\pi^{lab} < 25^\circ$. The π^0 transverse momentum in the hadronic centre-of-mass frame must exceed 2.5 GeV. The selection of particles with large transverse momenta gives sensitivity to the dynamics of the strong interaction. The π^0 s are identified using a shower shape analysis. (The π^0 energies are too high to detect the photons from the decay $\pi^0 \rightarrow \gamma\gamma$ directly). Due to the fine granularity of the H1 liquid argon calorimeter the reconstruction purity is significantly higher than that of forward jets. Forward neutral pions are also measured with higher precision than forward charged particles [152].

The data shown in Figure 45 show a strong rise of the cross section with decreasing x similar to that of the inclusive cross section. Models with parton shower evolution according to the DGLAP splitting functions fail to describe the data at low x . Inclusion of processes with a resolved virtual photon using RAPGAP improves the agreement with the data considerably

although some discrepancies at low x and low Q^2 remain. Calculations based on the modified LO BFKL equations (consistency constraint) [37] convoluted with π^0 fragmentation functions [145] give the best description of the data.

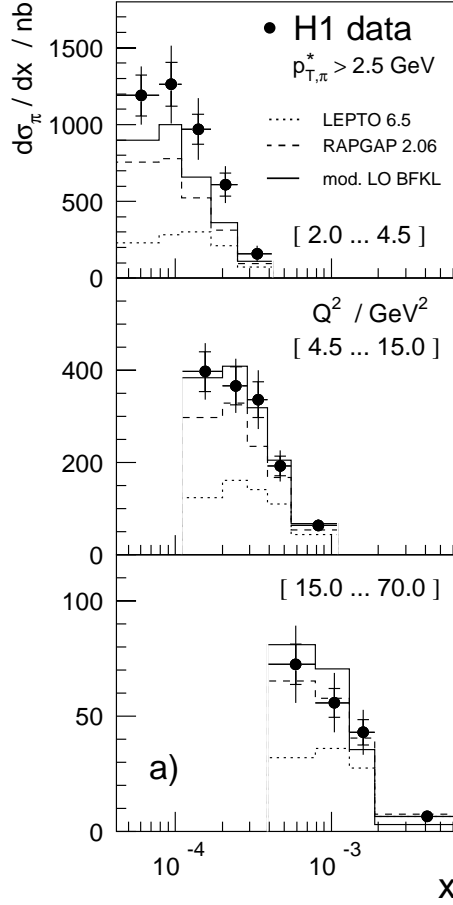


Figure 45: Inclusive forward π^0 cross section as a function of x in three ranges of Q^2 .

The forward pion cross sections belong to the observables most sensitive to parton evolution at low x . The success of the predictions based on the modified BFKL evolution is remarkable. It should be noted that the calculation depends on an infrared cut-off and on the choice of the renormalization scale. (The latter also limits the predictive power of DGLAP predictions.) Again calculations in NLO for parton evolution according to DGLAP or BFKL equations are not yet available.

6 Inclusive particle distributions

Perturbative QCD has been remarkably successful when applied to hard scattering processes with pronounced jet structures and when hadronization effects are relatively small. Soft interactions and the formation of hadrons are much less well understood. Thus particle momentum spectra and particle multiplicity distributions in high energy reactions cannot be rigorously calculated without model assumptions.

The study of these and related observables which are presented below tests perturbative QCD at its limits of validity. It investigates to which extent particle spectra still reflect the properties of perturbative parton shower evolution, and it allows to see effects of soft gluon interference. Comparison of measurements from different initial reactions, tests the ‘universality’ of the fragmentation process. Finally, perturbative QCD in NLO predicts the energy dependence of fragmentation functions, although –as for structure functions– the fragmentation functions themselves cannot be calculated.

The large range in Q^2 which is accessible in DIS at HERA is a particular advantage in many of the analyses presented below. The complex initial (and final) state and the presence of boson-gluon-fusion –in addition to quark scattering– may again be expected to make data description in DIS more challenging than in e^+e^- annihilation.

6.1 Charged particle multiplicities

The *mean charged particle multiplicity* in DIS at HERA was measured in [158, 159, 160, 161, 162]. A recent example is given in Figure 46 [162]. (Experimental aspects of the corresponding analysis are covered in section 6.2.)

The mean multiplicity increases over a factor of six in the kinematic range of $10 < Q^2 < 5120 \text{ GeV}^2$. For values of Q^2 larger than $\approx 80 \text{ GeV}^2$ the mean multiplicity agrees with that measured in e^+e^- annihilation [163] at the corresponding centre-of-mass energies.¹³ This confirms the expectation of approximate universality of quark fragmentation. At low Q^2 significant differences between e^+e^- annihilation and DIS are observed, however. These are caused by the depletion of the current hemisphere due to higher order processes which has no analogue in e^+e^- annihilation. The possible configurations of the quark and gluon produced in a QCD-Compton process as seen in the Breit frame are illustrated in Figure 47 [164]. The configuration (c) where the partons are both produced in the target hemisphere is likely to yield a significantly reduced number of particles in the current hemisphere.

Charged particle multiplicity distributions have been measured in different rapidity regions of the hadronic centre-of-mass frame in [160]. *Log-normal* distributions [166] and *negative binomial* probability functions give a fair parameterization of multiplicity distributions although deviations from the data are seen at small multiplicities. The scaled multiplicity distribution $\Psi(n/\langle n \rangle) = \langle n \rangle \times P(n)$ is widely used to investigate the multiplicity distributions at different Q^2 . $P(n)$ is the probability to observe an event with n particles, $\langle n \rangle$ is the mean multiplicity. The hypothesis of KNO scaling [167] predicts $\Psi(n/\langle n \rangle)$ to be independent of Q^2 . At low Q^2

¹³The mean multiplicity of the e^+e^- experiments is divided by two.

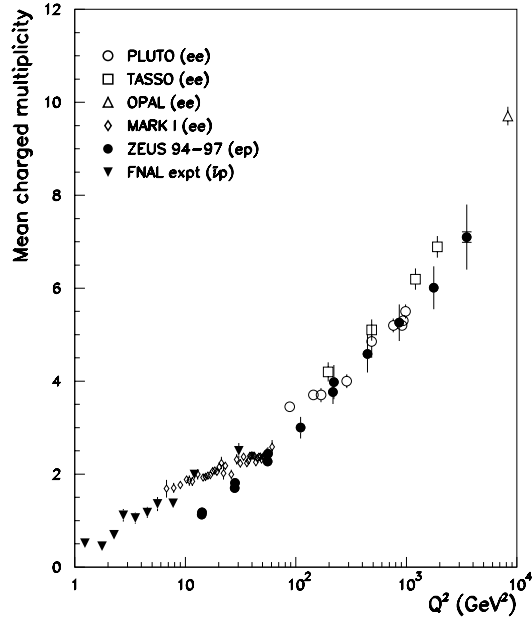


Figure 46: Mean charged particle multiplicity in the current hemisphere of the Breit frame. Measurements from e^+e^- annihilation and fixed-target DIS are also shown.

clear deviations from KNO scaling are observed in the current hemisphere of the Breit frame [158, 161]. This may again be attributed to the influence of higher order processes discussed above for the mean charged particle multiplicity.

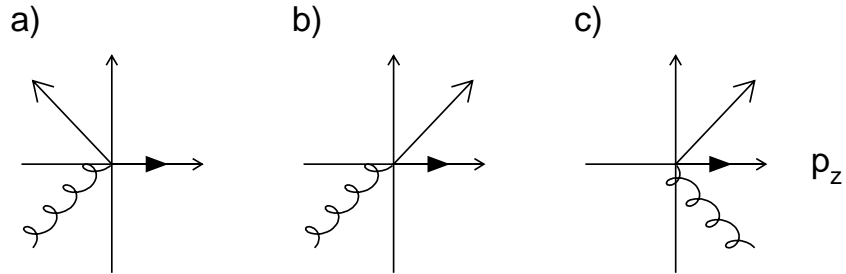


Figure 47: Possible parton configurations after absorption of the virtual photon in the Breit frame. The proton remnant points to the right.

6.2 Fragmentation functions and scaling violations

Inclusive charged particle distributions cannot yet be calculated within perturbative QCD. The fragmentation probability of a parton i into a hadron h with momentum fraction x can, however,

be parameterized by universal fragmentation functions $D_i^h(x, Q^2)$, where Q^2 represents the QCD scale of the process. As for the parton densities, perturbative QCD predicts the scale dependence of the fragmentation functions according to the DGLAP equations

$$\frac{dD_i^h(x, Q^2)}{\ln Q^2} = \sum_j \int_x^1 \frac{dz}{z} P_{ji}(z) D_j^h(x/z, Q^2) \quad (69)$$

where the P_{ji} are the splitting functions which are identical to those of equation (27) in LO. Convolution of the fragmentation functions with the *partonic* cross sections predicts the inclusive single *hadron* momentum distribution $1/\sigma_{DIS} d\sigma/dx_p$ where $x_p = 2p/Q$ is the scaled hadron momentum (denoted x in (69)). Comparing such predictions with inclusive charged particle distributions measured in e^+e^- experiments, fragmentation functions have been determined in a procedure very similar to the determination of structure functions in DIS [145].

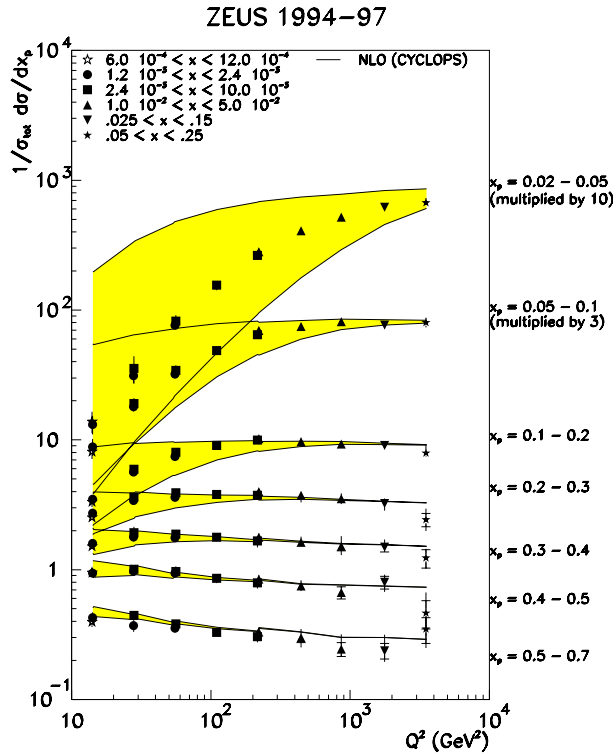


Figure 48: Fragmentation functions in the current hemisphere of the Breit frame compared with NLO predictions combined with a power correction.

Both H1 and ZEUS have measured inclusive charged particle spectra as a function of scaled hadron momentum $x_p = 2p^{Breit}/Q$. The ZEUS measurement is based on the data collected in '94-'97 corresponding to an integrated luminosity of 36 pb^{-1} . Tracks with $p_T^{lab} > 150 \text{ MeV}$ were selected in the range $-1.75 < \eta^{lab} < 1.75$, the region where the central tracker response is best understood. In Figure 48 the data are shown as a function of Q^2 for different ranges

of x_p . The spectra have been corrected for decay products of Λ and K_s^0 originating from the primary vertex. (The measurement is in fair agreement with preliminary measurements of H1 [168].)

At large x_p a significant decrease of the distributions with increasing Q^2 is observed corresponding to the production of more particles with smaller fractional momentum. This behaviour is indicative for scaling violations in the fragmentation function. For smaller values of x_p the distributions rise with increasing Q^2 .

The measurements are compared with a NLO calculation [173] folded with the fragmentation functions of [145]. At large Q^2 and not too small values of x_p the data and the calculation agree well. The agreement with a calculation using fragmentation functions derived from e^+e^- annihilation data shows the universality of the fragmentation process.

It is interesting to investigate the data description at small x_p and small Q^2 where the distribution is steeply falling. This region is likely to be influenced by power corrections. A power correction of the form $1/[1 + (\mu/Qx_p)^2]$ has been suggested [174] and is applied on top of the NLO prediction for the extreme scenarios $\mu = 0.1$ and 1.0 GeV (defining the shaded band in the Figure). First calculations of the power corrections were reported by [176]. The validity of the NLO prediction at small values of Q^2 and for particle momenta close to hadron masses is limited [173], and the pure NLO calculations significantly overshoot the data (not shown). The addition of the power correction gives agreement with the data. At large values of Q^2 and x_p where the power corrections are small, extraction of the strong coupling should be possible.

6.3 Particle spectra at small x

Although large deviations between NLO predictions and data are observed in the region of small momenta (small x_p), predictions in this region are still possible in the framework of Modified Leading-Logarithm Approximation (**MLLA**) where terms of $\xi = \log(1/x_p)$ are resummed.

In the MLLA the leading contributions from the collinear and soft singularities are resummed considering colour coherence. The non-leading single logarithms are also resummed. Assuming LPHD, parton distributions calculated in the MLLA can directly be related to the corresponding measurements of hadrons by simple normalization constants. MLLA in conjunction with LPHD makes predictions as a function of two parameters only, the effective QCD scale Λ and the cut-off parameter Q_0 .

Due to the coherence effects, the mean parton multiplicity in a parton cascade rises more slowly with initial parton energy than otherwise. The distribution of scaled particle momenta expressed in the variable $\xi = \ln(1/x_p) = \ln(Q/2p^{Breit})$ is modified to a skewed Gaussian. MLLA predictions exist for mean m , width w and the higher moments kurtosis k and skewness s of the ξ distributions. The ZEUS collaboration have measured ξ distributions in the current hemisphere of the Breit frame for $10 < Q^2 < 5120$ GeV². The distributions are well described by distorted Gaussian functions of the form

$$\frac{1}{\sigma_{DIS}} \frac{d\sigma}{d\xi} = \exp\left(\frac{1}{8}k - \frac{1}{2}s\delta - \frac{1}{4}(2+k)\delta^2 + \frac{1}{6}s\delta^3 + \frac{1}{24}k\delta^4\right), \quad (70)$$

ZEUS 1994–1997

- | | |
|---|--|
| <ul style="list-style-type: none"> * $0.6 \cdot 10^{-5} < x < 1.2 \cdot 10^{-5}$ • $1.2 \cdot 10^{-5} < x < 2.4 \cdot 10^{-5}$ ■ $2.4 \cdot 10^{-5} < x < 10 \cdot 10^{-5}$ ▲ $1.0 \cdot 10^{-2} < x < 5 \cdot 10^{-2}$ | <ul style="list-style-type: none"> ▼ $0.025 < x < 0.15$ * $0.05 < x < 0.25$ △ e^+e^- |
|---|--|

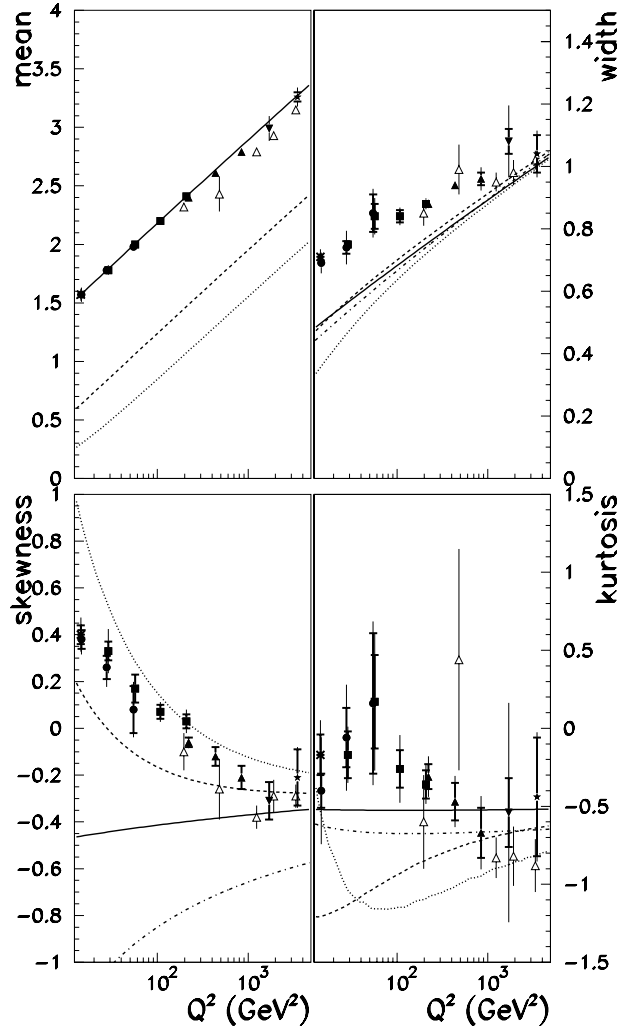


Figure 49: Q^2 dependence of mean, width and higher moments of the ξ distributions measured in the current hemisphere of the Breit frame. Also shown are fits to MLLA predictions.

where δ is related to the width and mean by $\delta = (\xi - m)/w$.

The evolution of mean, width, kurtosis and skewness with Q^2 is compared with MLLA predictions assuming LPHD for different values of Q_0 at $\Lambda = 175$ MeV in Figure 49. The Q^2 dependence of the mean is well described by MLLA but no consistent description of mean, width, kurtosis and skewness can be achieved. This may be related to the observed correlations between the target and current hemisphere as discussed in the next sections or to the assumption of massless partons in the MLLA predictions [171]. The DIS data roughly agree with data from

e^+e^- annihilation also shown.

The ξ distribution of particles with $x_p < 1$ have also been measured for the target hemisphere and are shown together with those of the current hemisphere in Figure 50. Note that values of $x_p > 1$ are kinematically allowed in the target hemisphere. The restriction $x_p < 1$ selects only a small part of the complete phase space which is expected in the MLLA to yield a Gaussian ξ distribution with a maximum in the range of $\xi = 1.5 - 2.5$ [172].

A very different behaviour of the ξ distributions in the target and current hemispheres is observed. The target hemisphere distributions do not show the approximate Gaussian shape as those in the current hemisphere. Thus again a clear deviation from MLLA is observed. The QCD models ARIADNE, LEPTO (without SCI) and LDC give a fair description of the distributions in the target hemisphere.

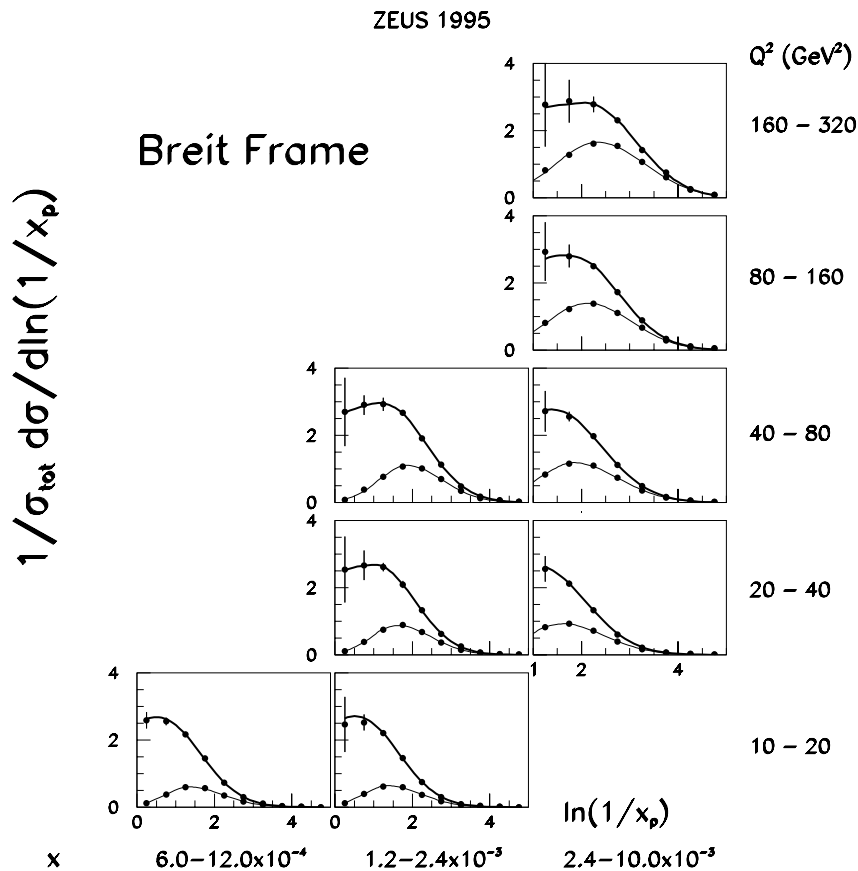


Figure 50: $\ln(1/x_p)$ distributions for the target and current hemispheres.

6.4 Angular correlations

Observables measuring two-particle correlations are complementary to the global particle multiplicity or inclusive particle spectra. They promise to be even more sensitive to the detailed

characteristics of the hadronic final state and their comparison with analytical QCD calculations, QCD model predictions and measurements in e^+e^- may be more likely to reveal current limitations of theoretical understanding.

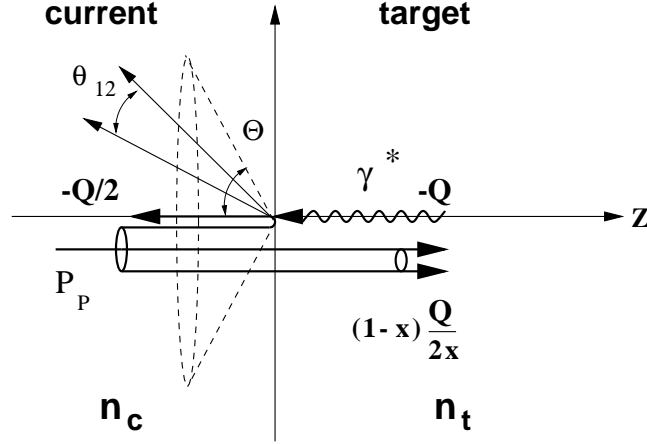


Figure 51: Illustration of the correlations between particles in a cone of opening angle Θ separated by the angle θ_{12} in the current hemisphere of the Breit frame.

In the Double Logarithmic Approximation (**DLA**), the leading contributions from the collinear and soft singularities are resummed. The change of energy and momentum of a parent parton due to parton radiation is ignored as well as finite energy effects (which are only considered in the MLLA). DLA predictions exist for the normalized two-particle density \hat{Y} and the correlation function Y . These observables are related to the inclusive two-particle density ρ which measures the density of particle pairs separated by the angle θ_{12} in a cone of opening angle Θ centered around the Breit frame axis as illustrated in Figure 51. The DLA predictions are available as a function of the scaling variable ϵ given by

$$\epsilon = \frac{\ln(\Theta/\theta_{12})}{\ln(P \sin \Theta/\Lambda)} \quad (71)$$

where Λ is the QCD scale and the initial parton momentum P is set to $Q/2$. The variables \hat{Y} and Y are given by

$$\hat{Y}(\epsilon) = \frac{\ln \left[\frac{\rho(\epsilon)}{\langle n(\Theta) \rangle^2 \beta \sqrt{\ln [P \sin \Theta/\Lambda]}} \right]}{\sqrt{\ln [P \sin \Theta/\Lambda]}} \quad \text{and} \quad Y(\epsilon) = \frac{\ln \frac{\rho(\epsilon)}{\rho_{mix}(\epsilon)}}{\sqrt{\ln [P \sin \Theta/\Lambda]}} \quad (72)$$

where β is 1.15 for $n_f = 3$, and $\langle n(\Theta) \rangle$ is the mean particle multiplicity in the cone of opening angle Θ . ρ_{mix} is the two-particle density calculated using particles from different events. By introducing ρ_{mix} , Y is expected to be less dependent on the single-particle spectra than \hat{Y} . Both observables are predicted to be independent of Q and Θ .

ZEUS have studied two-particle correlations with the data collected in '95 corresponding to an integrated luminosity of 6.4 pb^{-1} [177]. The \hat{Y} distributions measured in a large range of Q^2 are shown together with the DLA predictions for both constant and running α_s in Figure 52. A

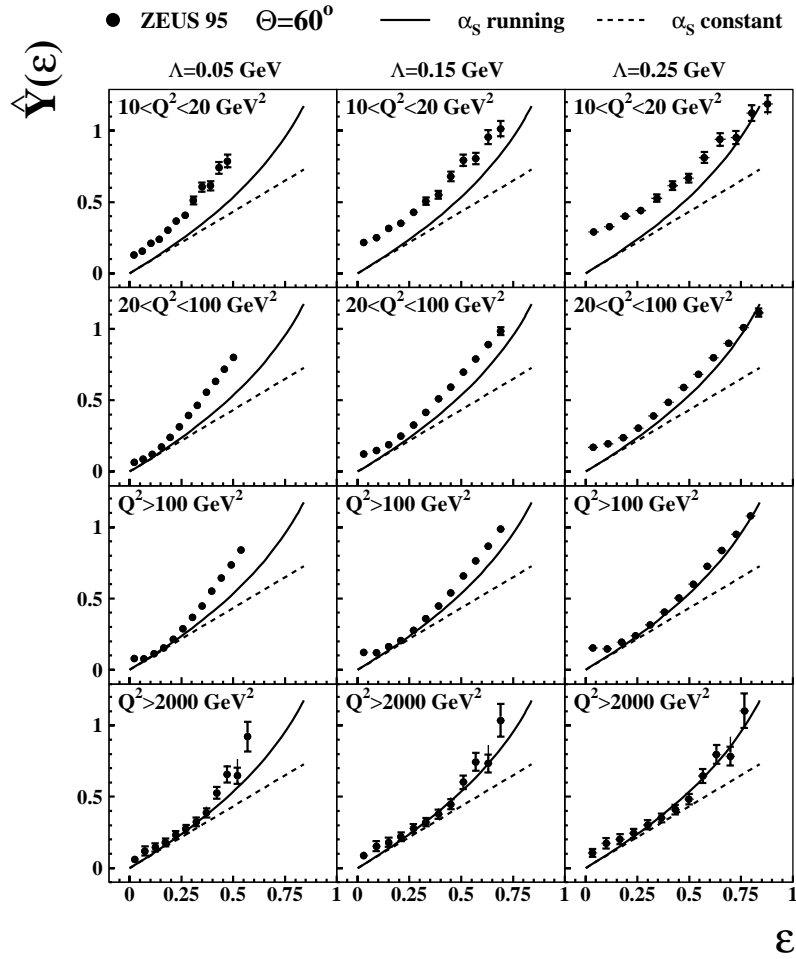


Figure 52: The normalized two-particle density $\hat{Y}(\epsilon)$ compared with analytical QCD predictions in the DLA.

fair description of the data is achieved for $\Lambda = 250$ MeV at sufficiently high Q^2 . The measurement nicely excludes a constant value of α_s . For both \hat{Y} and Y the predicted independence on Θ is supported (not shown) and the discrepancies between data and predictions decrease with increasing Q^2 .

Y is significantly less well described than \hat{Y} in particular at low Q^2 . A comparison with e^+e^- annihilation at comparable energy (see Figure 53) suggests that two-particle correlations are non-universal although errors are still large.

6.5 Current-target hemisphere correlations

Long-range correlations in rapidity have been studied in various reactions at different energies. Positive correlations have been reported in e^+e^- annihilation at LEP1 and are mainly due to heavy quark production [180].

Correlations between the particle multiplicity in the current and target hemispheres of the Breit frame have been investigated by the ZEUS collaboration using the same data as above

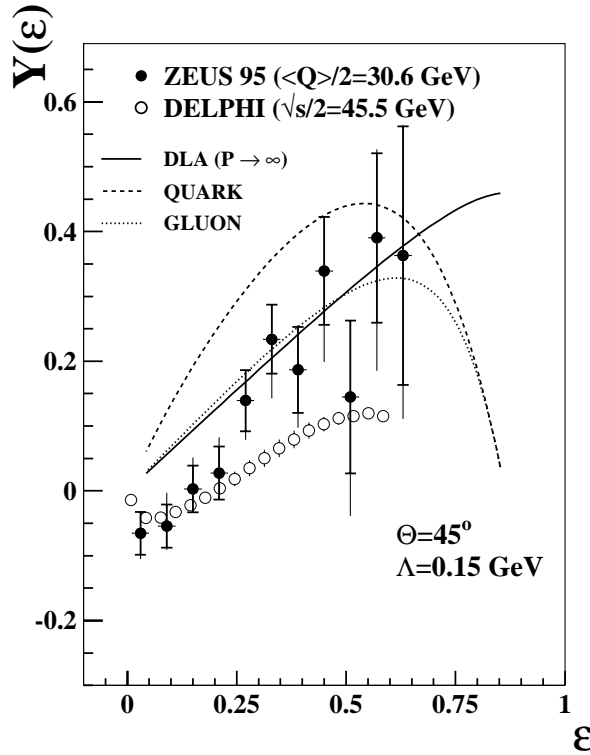


Figure 53: The correlation function $Y(\epsilon)$ for $Q^2 > 2000 \text{ GeV}^2$ compared with analytical QCD predictions and results from e^+e^- annihilation.

[177]. As a simple measure of the correlation strength the correlation coefficient

$$\kappa = \frac{\langle n_c n_t \rangle - \langle n_c \rangle \langle n_t \rangle}{\sigma_c \sigma_t} \quad (73)$$

is introduced. Here, n_c and n_t are the number of charged particles in the current and target hemispheres, respectively. σ_c and σ_t are the standard deviation of the corresponding multiplicity distributions.

The measured value of κ is shown as a function of Q^2 and x in Figure 54. Large anti-correlations –corresponding to negative κ – are observed, which decrease with Q^2 and x . Once again ARIADNE describes the data best.

Anti-correlations in DIS are expected to arise due to the higher order processes QCD-Compton scattering and boson-gluon-fusion [178]. Essentially no correlation, corresponding to $\kappa \approx 0$, is expected for QPM events. At low Q^2 BGF is by far the dominant higher order process. Measurement of κ may thus provide a tool to determine the fraction of BGF events, complementary to the measurements of jet rates.

6.6 Bose–Einstein correlations

Identical bosons prefer to occupy the same quantum state. This leads to Bose-Einstein correlations (**BEC**) –an increased probability of identical bosons to be produced at small momentum

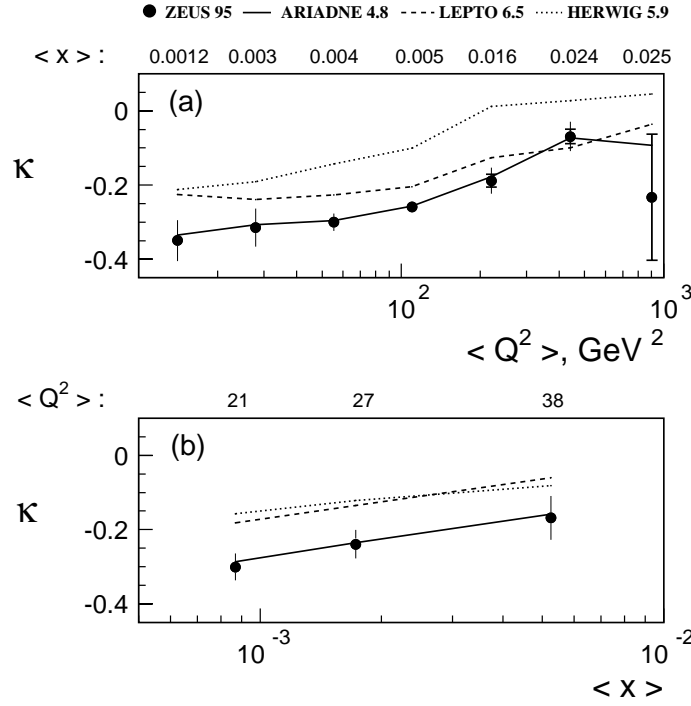


Figure 54: Multiplicity correlations between the current and target hemisphere of the Breit frame.

separation compared with the probability for non-identical bosons. BEC were first observed for charged pions by Goldhaber in $p\bar{p}$ collisions [181] and have since been investigated by various experiments in different scattering processes [182, 183, 184, 185].

BEC are usually expressed in terms of the normalized correlation function

$$C(T) = \frac{\rho_2(p_1, p_2)}{\rho_1(p_1)\rho_1(p_2)} \quad (74)$$

where $\rho_2(p_1, p_2)$ is the probability density for production of two identical bosons with four-momenta p_1 and p_2 . The Lorentz invariant variable $T^2 = (p_1 - p_2)^2 = M_2^2 - 4m_\pi^2$ is a measure of distance of the bosons. Here M_2 is the invariant mass of the two bosons and m_π is the pion mass. The product of the single-boson densities ρ_1 in equation (74) serves as a reference distribution which ideally considers any correlations other than BEC. Such correlations can be due to the decay of resonances, due to energy, momentum and charge conservation and due to the overall event topology.

Several parameterizations of the correlation function $C(T)$ have been proposed. Assuming a spherically symmetric pion source with a Gaussian radial distribution, results in the correlation function

$$C(T) = N(1 + \lambda e^{-T^2 R^2}) \quad (75)$$

where R is the source size and the parameter λ , with values from 0 to 1, measures the strength of the correlation. N is a normalization factor.

BEC have been measured by the H1 collaboration [186]. The measurement is based on a data sample of $\approx 50,000$ events collected in '94. The reference distribution was constructed using unlike-charge pairs of particles from the same event or from mixing charged particles from different events. The residual biases were estimated using Monte Carlo calculations without BEC and are considered by taking the double ratio $C^{Data}(T)/C^{MC}(T)$. The measurement crucially relies on the precise reconstruction of T in particular at small T . The resolution of T is determined to be 3.5 MeV for $T=0.1$ GeV. Misidentification of a single track as two separate track pieces leads to two like-sign tracks at small T and thus mimics BEC. After application of track quality requirements the splitting probability is 0.3%.

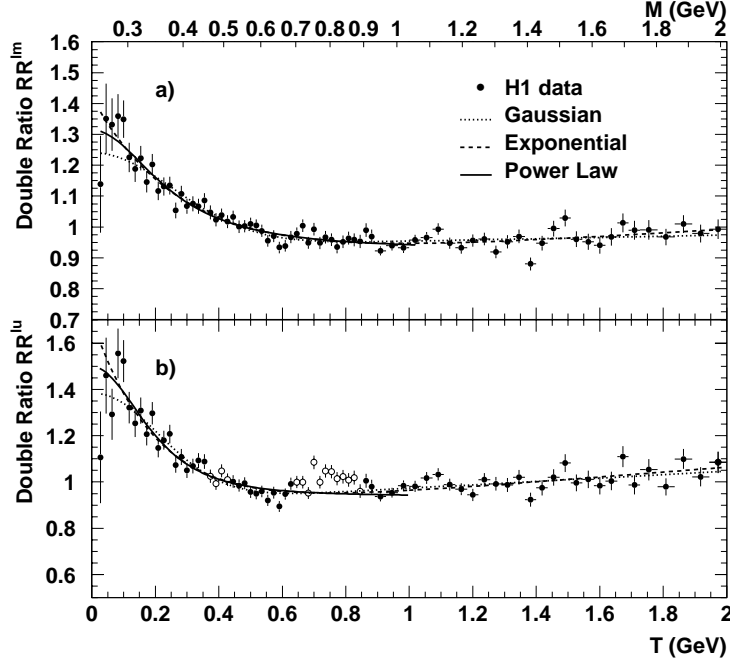


Figure 55: Bose-Einstein-correlations for references samples based on event-mixing (top) and unlike-charge pairs (bottom) fitted to different parameterizations of the correlation function.

In Figure 55 a significant signal of BEC is observed. The size of the effect does not depend on T^2 , x or W . No significant difference for diffractive and non-diffractive events is seen. The systematic errors are smallest for the event-mixing method. Using this method and the Gaussian parameterization of the correlation functions, the source size R and the correlation strength λ are determined to be

$$\begin{aligned} R &= 0.54 \pm 0.03 \text{ (stat.) } {}^{+0.03}_{-0.02} \text{ (syst.) fm} \\ \lambda &= 0.32 \pm 0.02 \text{ (stat.) } \pm 0.06 \text{ (syst.)} \end{aligned} \quad (76)$$

The measured source size R is in fair agreement with that determined in lepton-nucleon scattering experiments at lower energies and that in e^+e^- annihilation. This confirms the universal character of hadronization and the approximate size of the hadronization region of 1 fm.

There is continuous interest in Bose-Einstein correlations e.g. in connection with the W mass measurement from W^+W^- production at LEP2 [187]. Theoretical models have been proposed which treat the shape of the pion emitting source in more than one dimension [188]. Corresponding measurements have been performed at LEP [189]. Given these developments analysis of BEC in DIS based on a much increased data sample seems worthwhile.

7 Conclusions

With the advent of the ep collider HERA a new era in DIS has begun. HERA extends the kinematic range accessible in fixed target experiments by several orders of magnitude in x and Q^2 . The collider detectors H1 and ZEUS are instrumented to measure the scattered lepton and the hadronic final state precisely. Powerful tests of QCD and of the electroweak sector of the standard model are made possible through measurement of inclusive DIS cross sections. A wealth of additional information is provided through investigation of the hadronic final state.

Due to the complexity of DIS events and the pioneering character of hadronic final state measurements at HERA, analysis concepts and interpretation of results have not always been obvious. This has led to a particularly close collaboration of experimentalists and theorists. In parallel with the increasing number and precision of experimental results the development of QCD Monte Carlo models, analytical QCD calculations and of NLO programs has taken place. Eight years after the start of ep collisions at HERA understanding of the hadronic final state in terms of QCD has reached maturity. The most important results covered in this review are:

- Perturbative QCD in next-to-leading order gives a good description of multi-jet production including the kinematic range of $Q^2 > 10,000 \text{ GeV}^2$ and invariant dijet masses up to 150 GeV as well as the regions of low Q^2 and x .

Current QCD Monte Carlo programs, in contrast, have difficulties modelling the hadronic final state precisely.

- The value of the strong coupling α_s is found to be consistent with the world average. The renormalization scale dependence of α_s has been determined as a function of Q^2 and jet transverse energy and corresponds to the QCD expectation.
- Overall, the concept of analytical power corrections to mean values of event shape distributions is supported. The spread of the values of $\alpha_s(M_Z)$ and of the effective strong coupling $\bar{\alpha}_0$ for different event shape variables indicates that further theoretical progress is necessary.
- The gluon density of the proton is determined for momentum fractions $x > 0.01$ where determinations from structure function measurements start to be less sensitive.
- Various experimental signatures suggesting deviations from DGLAP parton evolution are observed at low x , the region of high parton densities. Further experimental and theoretical progress is still needed for unambiguous interpretation of the data.
- Analyses of charged particle multiplicities and momentum spectra reveal limitations of analytical QCD predictions.

In autumn 2001 after completion of the luminosity upgrade, HERA is expected to provide an integrated luminosity of $150 \text{ pb}^{-1}/\text{year}$. Equipped with the huge data sample that will finally be collected, major progress is expected from:

- *the extension of existing measurements with higher precision*

This concerns in particular the region of $Q^2 > 10,000 \text{ GeV}^2$, which can be investigated with high experimental precision. In addition stricter selection criteria for multi-jet events will reduce theoretical uncertainties and notably increase the precision of α_s measurements. Combined fits of structure functions and jet cross sections are expected to reduce the impact of other experiments and the related systematic uncertainties substantially.

Note that the larger data sample will not only lead to smaller statistical errors but will also help reduce experimental systematic errors through e.g. improved calibration.

- *access to fields that are as yet unexplored*

This includes the systematic study of jets in tagged heavy flavour events; systematic measurement of identified particle distributions; separation of quark/antiquark and gluon jets with jet charge methods; study of the three-gluon vertex and measurement of the QCD colour factors in three-jet events at moderate Q^2 .

- *new theoretical developments*

Improved data description by QCD Monte Carlo models remains important. It will lead to better estimates of experimental errors and to better understanding of the hadronic final state. NLO programs should include Z^0 and W^\pm exchange since the region of high Q^2 is the main focus of attention after the upgrade. Further clarification of inconsistencies between existing programs is desirable. Resummed calculations for typical experimental observables, if feasible, should have enormous impact on the precision of QCD tests and would extend the region that can be tested with perturbative QCD.

References

- [1] E.D. Bloom *al.*, Phys. Rev. Lett. **23** (1969) 930;
M. Breidenbach *al.*, Phys. Rev. Lett. **23** (1969) 935;
R.E. Taylor, Rev. Mod. Phys. **63** (1991) 573; H.W. Kendall, *ibid.* 597; J.I. Friedmann, *ibid.* 615.
- [2] C. Chang *al.*, Phys. Rev. Lett. **35** (1975) 901;
E.M. Riordan *al.*, Phys. Lett. **B52** (1974) 249.
- [3] See H. Abramowicz, DESY-00-025 and hep-ph/0001054, Proceedings of LP99, Stanford, USA;
P. Marage, hep-ph/9911426, Proceedings of HEP99, Tampere, Finland;
M. Diehl, K. Piotrkowski and R. Roosen, Proceedings of the Workshop on Monte Carlo Generators for HERA Physics, Eds. A.T. Doyle, G. Grindhammer, G. Ingelman and H. Jung, DESY-PROC-1999-02 349.
- [4] R. Frisch and O. Stern, Z. Phys. **85** (1933) 4;
I. Estermann and O. Stern, Z. Phys. **85** (1933) 17.
- [5] M. Gell-Mann, Phys. Lett. **8** (1994) 214.
- [6] G. Zweig, CERN-TH-401 and CERN-TH-412 (1994) also in *Developments in the Quark Theory of Hadrons, A Reprint Collection*, Vol. I, Hadronic Press, Eds. D.B. Lichtenberg and S.P. Rosen (1980).
- [7] M.Y. Han and Y. Nambu, Phys. Rev. **B139** (1965) 1006.
- [8] H. Fritzsch, M. Gell-Mann, H. Leutwyler, Phys. Lett. **B47** (1973) 365.
- [9] D.J. Gross and F. Wilczek, Phys. Rev. Lett. **30** (1973) 1343;
H.D. Politzer, Phys. Rev. Lett. **30** (1973) 1346;
D.J. Gross and F. Wilczek, Phys. Rev. **D8** (1973) 3633;
D.J. Gross and F. Wilczek, Phys. Rev. **D9** (1974) 980.
- [10] G. Hanson *et al.*, Phys. Rev. Lett. **35** (1975) 1609.
- [11] TASSO Collaboration, R. Brandelik *et al.*, Phys. Lett. **B86** (1979) 243;
MARK J Collaboration, D.P. Barber *et al.*, Phys. Rev. Lett. **43** (1979) 830;
PLUTO Collaboration, Ch. Berger *et al.*, Phys. Lett. **B86** (1979) 418;
JADE Collaboration, W. Bartel *et al.*, Phys. Lett. **B91** (1980) 142.
- [12] TASSO Collaboration, R. Brandelik *et al.*, Phys. Lett. **B97** (1980) 453;
PLUTO Collaboration, Ch. Berger *et al.*, Phys. Lett. **B97** (1980) 459;
CELLO Collaboration, H.J. Behrend *et al.*, Phys. Lett. **B110** (1982) 329.
- [13] OPAL Collaboration, M.Z. Akrawy *et al.*, Z. Phys. **C49** (1991) 49;
L3 Collaboration, B. Adeva *et al.*, Phys. Lett. **B248** (1990) 227;
DELPHI Collaboration, P. Abreu *et al.*, Phys. Lett. **B255** (1991) 466;
ALEPH Collaboration, D. Decamp *et al.*, Phys. Lett. **B284** (1992) 151.

- [14] See e.g. R.K. Ellis, W.J. Sterling and B.R. Webber, *QCD and Collider Physics*, Cambridge University Press (1996).
- [15] W.A. Bardeen, A.J. Buras, D.W. Duke and T. Muta, *Phys. Rev. D* **18** (1978) 3998.
- [16] C.G. Callan, *Phys. Rev.* **D2** (1970) 1541;
K. Symanzik, *Comm. Math. Phys.* **18** (1970) 227.
- [17] T. van Ritbergen, J.A.M. Vermaseren, S.A. Larin, *Phys. Lett.* **B400** (1997) 379.
- [18] W. Furmanski and R. Petronzio, *Z.Phys.* **C11** (1982) 293.
- [19] Particle Data Group, *Eur. Phys. J.* **C3** (1998) 81.
- [20] K.G. Chetyrkin, B.A. Kniehl and M. Steinhauser, *Phys. Rev. Lett.* **79** (1997) 2184.
- [21] W. Bernreuther and W. Wetzel, *Nucl. Phys.* **B197** (1982) 228 and Erratum *Nucl. Phys.* **B513** (1998) 758;
W. Bernreuther, *Ann. Phys. (NY)* **151** (1983) 127.
- [22] W. Marciano, *Phys. Rev.* **D29** (1984) 580.
- [23] Particle Data Group, *Phys. Rev.* **D54** (1996) 77.
- [24] BCDMS Collaboration, A. Benvenuti *et al.*, *Phys. Lett.* **B223** (1989) 485 and *Phys. Lett.* **B237** (1990) 592.
- [25] NMC Collaboration, M. Arneodo *et al.*, *Nucl. Phys.* **B487** (1997) 3.
- [26] E665 Collaboration, M.R. Adams *et al.*, *Phys. Rev.* **D54** (1996) 3006.
- [27] SLAC, L.W. Whitlow *et al.*, *Phys. Lett.* **B282** (1992) 475.
- [28] H1 Collaboration, C. Adloff *et al.*, DESY-99-107 and hep-ex/9908059, accepted by *Eur. Phys. J.* **C**.
- [29] H1 Collaboration, *Measurement of the charged and neutral current cross sections at HERA*, contributed paper to HEP99, Tampere, Finland.
- [30] ZEUS Collaboration, J. Breitweg *et al.*, *Eur. Phys. J.* **C11** (1999) 427;
ZEUS Collab., J. Breitweg *et al.*, *Eur. Phys. J.* **C12** (2000) 411.
- [31] ZEUS Collaboration, *Measurement of High- Q^2 Charged-Current e^-p Deep Inelastic Scattering Cross-Sections and Measurement of High Q^2 Neutral Current Deep Inelastic Scattering Cross Sections in e^-p Scattering at HERA*, contributed papers to HEP99, Tampere, Finland.
- [32] Yu.L. Dokshitzer, *Sov. Phys. JETP* **46** (1977) 641;
V.N. Gribov and L.N. Lipatov, *Sov. Phys. J. Nucl. Phys.* **15** (1972) 438 and 675;
G. Altarelli and G. Parisi, *Nucl. Phys.* **B126** (1977) 297.
- [33] A. de Rujula, S.L. Glashow, H.D. Politzer, S.B. Treiman, F. Wilczek and A. Zee, *Phys. Rev.* **10** (1974) 1649.

- [34] E.A. Kuraev, L.N. Lipatov and V.S. Fadin, Phys. Lett. **B60** (1975) 50; Sov. Phys. JETP **44** (1976) 433; *ibid.* **45** (1977) 199;
Ya.Ya. Blaitsky and L.N. Lipatov, Sov. J. Nucl. Phys **28** (1978) 822.
- [35] V.S. Fadin and L.N. Lipatov, Phys. Lett. **B429** (1998) 127;
G. Camici and M. Ciafaloni, Phys. Lett. **B430** (1998) 349.
- [36] J. Kwiecinski, A.D. Martin, P.J. Sutton, Z. Phys. **C71** (1996) 585.
- [37] J. Kwiecinski, A.D. Martin, J.J. Outhwaite, Eur. Phys. J. **C9** (1999) 611.
- [38] M. Ciafaloni, Nucl. Phys. **B296** (1988) 49;
S. Catani, F. Fiorani and G. Marchesini, Phys. Lett. **B234** (1990) 339 and Nucl. Phys. **B336** (1990) 657.
- [39] M. Glück, E. Reya, A. Vogt, Eur. Phys. J. **C5** (1998) 461.
- [40] CTEQ5 Collaboration, H.L. Lai *et al.*, Eur. Phys. J. **C12** (2000) 375.
- [41] A.D. Martin, R.G. Roberts, W.J. Stirling and R.S Thorne, hep-ph/9907231.
- [42] A.D. Martin, R.G. Roberts, W.J. Stirling and R.S Thorne, Eur. Phys. J. **C4** (1998) 463.
- [43] see for example Max Klein, Proceedings of LP 99, Stanford, USA and hep-ex/0001059.
- [44] J.G. Körner, E. Mirkes and G.A. Schuler, Int. J. Mod. Phys. **A4** (1989) 1781.
- [45] M. Bengtsson and T. Sjöstrand, Comp. Phys. Comm. **37** (1988), 465.
- [46] G. Gustafson, Phys. Lett. **B175** (1986) 453;
G. Gustafson and U. Petterson, Nucl. Phys. **B306** (1988) 746;
B. Andersson, G. Gustafson L. Lönnblad and U. Petterson, Z. Phys. **C43** (1989) 625.
- [47] B. Andersson, G. Gustafson, G. Ingelman and T. Sjostrand, Phys. Rep. **97** (1983) 31.
- [48] B.R. Webber, Nucl. Phys. **B238** (1984) 492.
- [49] Ya.I. Azimov, Yu.L. Dokshitzer, V.A. Khoze and S.I. Troyan, Z. Phys. **C27** (1985) 65; Z. Phys. **C31** (1986) 231.
- [50] D. Amati and G. Veneziano, Phys. Lett. **B83** (1979) 87;
G. Marchesini, L. Trentadue and G. Veneziano, Nucl. Phys. **181** (1981) 335.
- [51] G. Sterman and S. Weinberg, Phys. Rev. Lett. **39** (1977) 1436.
- [52] see e.g. J.E. Huth *et al*, Proceedings of the Summer Study on High Energy Physics, Snowmass, Colorado (1990), Ed. E.L. Berger, World Scientific (1992).
- [53] M.H. Seymour, Nucl. Phys **B513** (1998) 269.
- [54] JADE Collaboration, W. Bartel *et al.*, Z. Phys. **C33** (1986) 23;
JADE Collaboration, S. Bethke *et al.*, Phys. Lett. **B213** (1988) 235.

- [55] see e.g. M. Fleischer, G. Ingelman, G. Knies, K. Meier, C. Pichler and A. Wegner, Proceedings of the Workshop Physics at HERA (Hamburg 1991), Eds. W. Buchmüller and G. Ingelman, Vol.1 303;
H1 Collaboration, I. Abt *et al.*, Z. Phys. **C61** (1994) 59;
ZEUS Collaboration, M. Derrick *et al.*, Z. Phys. **C67** (1995) 81.
- [56] S. Catani, Yu.L. Dokshitzer and B.R. Webber, Phys. Lett. **B285** (1992) 291; S. Catani, Yu.L. Dokshitzer, M.H. Seymour and B.R. Webber, Nucl. Phys. **B406** (1993) 187.
- [57] B.R. Webber, J. Phys. **G19** (1993) 1567.
- [58] S. Catani, Yu.L. Dokshitzer, M.H. Seymour and B.R. Webber, Nucl. Phys. **B406** (1992) 187.
- [59] S.D. Ellis, E. Soper, Phys. Rev. **D48** (1993) 3160.
- [60] A.A. Sokolov and L.N. Ternov, Soviet Physics Doklady **NO. 12** (1964) 1203.
- [61] H1 Collaboration, I. Abt *et al.*, Nucl. Instr. and Meth. **A386** (1997) 310 and 348.
- [62] ZEUS Collaboration, M. Derrick *et al.*, Phys. Lett. **B293** (1992) 465;
The ZEUS Detector, Status Report 1993, DESY (1993).
- [63] L. Lönnblad, Comp. Phys. Comm. **71** (1992) 15.
- [64] G. Marchesini, B.R. Webber, G. Abbiendi, I.G. Knowles, M.H. Seymour, L. Stanco, Comp. Phys. Comm. **67** (1992) 465.
- [65] G. Ingelman, LEPTO, version 6.1, Proc. of the Workshop ‘Physics at HERA’, Eds. W. Buchmüller and G. Ingelman, Vol. 3 (1992) 1366;
G. Ingelman, A. Edin and J. Rathsman, Comp. Phys. Comm. **101** (1997) 108.
- [66] H. Jung, Comp. Phys. Comm. **86** (1995) 147;
RAPGAP program manual (1998) unpublished.
- [67] L. Lönnblad, Z. Phys. **C65** (1995) 285.
- [68] L. Lönnblad, Proceedings of the Workshop on Monte Carlo Generators for HERA Physics, Eds. A.T. Doyle, G. Grindhammer, G. Ingelman and H. Jung, DESY-PROC-1999-02 47.
- [69] A. Edin, G. Ingelman and J. Rathsman, Phys. Lett. **B366** (1996) 371;
A. Edin, G. Ingelman and J. Rathsman, Z. Phys. **C75** (1997) 57.
- [70] J. Rathsman, Phys. Lett. **B452** (1999) 364.
- [71] H. Jung, Proceedings of the Workshop on Monte Carlo Generators for HERA Physics, Eds. A.T. Doyle, G. Grindhammer, G. Ingelman and H. Jung, DESY-PROC-1999-02 75.
- [72] H. Spiesberger *et al.*, Proceedings of the Workshop Physics at HERA (Hamburg 1991), Eds. W. Buchmüller and G. Ingelman, Vol.2 798.

- [73] for a recent overview see L. Favart, S. Schlenstedt and H. Spiesberger, Proceedings of the Workshop on Monte Carlo Generators for HERA Physics, Eds. A.T. Doyle, G. Grindhammer, G. Ingelman and H. Jung, DESY-PROC-1999-02 519;
A. Arbuzov, D. Bardin, J. Blümlein, L. Kalinovskaya and T. Riemann, Comp. Phys. Comm. **94** (1996) 128.
- [74] A. Kwiatkowski, H. Spiesberger, H.-J. Möhring, Comp. Phys. Comm. **69** (1992) 155.
- [75] K. Charchula, G.A. Schuler and H. Spiesberger, Comp. Phys. Comm. **81** (1994) 381;
H. Spiesberger, DJANGO program manual (1998) unpublished.
- [76] K. Fabricius, I. Schmitt, G. Kramer, G. Schierholz Z. Phys. **C11** (1981) 315.
- [77] R.K. Ellis, D.A. Ross, A.E. Terrano, Nucl. Phys. **B178** (1981) 421.
- [78] E. Mirkes and D. Zeppenfeld, Phys. Lett. **B380** (1996) 205.
- [79] S. Catani and M.H. Seymour, Nucl. Phys. **B485** (1997) 291.
- [80] D. Graudenz, *DISASTER++*, *version 1.0.1*, hep-ph/9710244 (1997).
- [81] G. Kramer and B. Pötter, Eur. Phys. J. **C5** (1998) 665;
B. Pötter, Comp. Phys. Comm. **119** (1999) 45.
- [82] T. Brodorb and E. Mirkes, MAD-PH-821 and hep-ph/9404287.
- [83] D. Graudenz, Comp. Phys. Comm. **92** (1995) 65.
- [84] C. Duprel, Th. Hadig, N. Kauer and M. Wobisch, Proceedings of the Workshop on Monte Carlo Generators for HERA Physics, Eds. A.T. Doyle, G. Grindhammer, G. Ingelman and H. Jung, DESY-PROC-1999-02 142; G. McCance *ibidem*.
- [85] see also B. Pötter, *JETVIP 2.1: THE HBOOK VERSION.*, MPI-PHT-99-54 (1999) and hep-ph/9911221.
- [86] Dirk Graudenz and Marc Weber, Proceedings of the Workshop on Monte Carlo Generators for HERA Physics, Eds. A.T. Doyle, G. Grindhammer, G. Ingelman and H. Jung, DESY-PROC-1999-02 117.
- [87] V. Antonelli, M. Dasgupta and G.P. Salam, hep-ph/9910343.
- [88] ZEUS Collaboration, J. Breitweg *et al.*, Eur. Phys. J. **C8** (1999) 367.
- [89] ZEUS Collaboration, J. Breitweg *et al.*, Eur. Phys. J. **C2** (1998) 61.
- [90] H1 Collaboration, C. Adloff *et al.*, Nucl. Phys. **B545** (1999) 3.
- [91] D. Chapin, Proceedings of DIS 2000, to be published in World Scientific.
- [92] M. Klasen and G. Kramer, Phys. Lett. **B366** (1996) 385;
S. Frixione and G. Ridolfi, Nucl. Phys. **B507** (1997) 315; S. Catani and B.R. Webber, JHEP **10** (1997) 5.

- [93] R.Pöschl, Proceedings of DIS 2000, to be published in World Scientific.
- [94] H1 Collaboration, *Study of Differential Dijet Event Distributions and Determination of α_s in Deeply Inelastic Scattering at Large Q^2* contributed paper to HEP99, Tampere, Finland.
- [95] F. Keil, Proceedings of DIS 2000, to be published in World Scientific.
- [96] ZEUS Collaboration, M. Derrick *et al.*, Z. Phys. **C72** (1996) 47.
- [97] N.H. Brook, T. Carli, E. Rodrigues, M.R. Sutton, N. Tobien, M. Weber, Proceedings of the Workshop on Monte Carlo Generators for HERA Physics, Eds. A.T. Doyle, G. Grindhammer, G. Ingelman and H. Jung, DESY-PROC-1999-02 10.
- [98] H. Georgi and H.D. Politzer, Phys. Rev. Lett. **40** (1978) 3.
- [99] R.N. Cahn, Phys. Lett. **B78** (1978) 269.
- [100] G. Köpp, R. Maciejko and P.M. Zerwas, Nucl. Phys. **B144** (1978) 123.
- [101] A. Mendez, Nucl. Phys. **B145** (1978) 199.
- [102] J. Chay, S.D. Ellis and W.J. Stirling, Phys. Lett. **B269** (1991) 175.
- [103] M. Ahmed and T. Gehrmann, Phys. Lett **B465** (1999) 297.
- [104] EMC Collaboration, M. Arneodo *et al.*, Z. Phys. **C34** (1987) 277.
- [105] E665 Collaboration, M.R. Adams *et al.*, Phys. Rev. **D48** (1993) 5037.
- [106] H1 Collaboration, *First Measurement of Three Jet Cross Sections in DIS at HERA*, contributed paper to HEP99, Tampere, Finland.
- [107] S. Geer, T. Asakawa, Phys. Rev. **D53** (1996) 4793.
- [108] H1 Collaboration, T. Ahmed *et al.*, Phys. Lett. **B346** (1995) 415.
- [109] ZEUS Collaboration, M. Derrick *et al.*, Phys. Lett. **B363** (1995) 201.
- [110] H1 Collaboration, C. Adloff *et al.*, Eur. Phys. J. **C5** (1998) 4 625.
- [111] H1 Collaboration, C. Adloff *et al.*, Eur. Phys. J. **C6** (1999) 4 575.
- [112] H1 Collaboration, C. Adloff *et al.*, Phys. Lett. **B406** (1997) 256.
- [113] H1 Collaboration, C. Adloff *et al.*, DESY 99-193, subm. to Eur.Phys.J. **C**.
- [114] Particle Data Group, Eur. Phys. J. **C3** (1998) 69.
- [115] S.J. Brodsky, G.P. Lepage and P.B. Mackenzie, Phys. Rev. **D28** (1983) 228.
- [116] G. Grunberg, Phys. Lett. **B95** (1980) 70; Phys. Lett. **B110** (1992) 501 and Phys. Rev. **D29** (1984) 2315.

- [117] P.M. Stevenson, Phys. Lett. **B100** (1981) 61; Phys. Rev. **D23** (1981) 2916; Nucl. Phys. **B203** (1982) 472 and Nucl. Phys. **B231** (1984) 65.
- [118] M. Wobisch, PhD thesis, RWTH Aachen (2000) unpublished.
- [119] T. Hadig, PhD thesis, RWTH Aachen (2000) unpublished;
T. Hadig, Proceedings of DIS 2000, to be published in World Scientific.
- [120] R.D. Ball and S. Forte, Phys. Lett. **B358** (1995) 411; A. de Roeck *et al.*, Phys. Lett. **B385** (1996) 411.
- [121] H1 Collaboration, *Determination of the strong coupling constant from the Inclusive Jet Cross Section in Deep-Inelastic Positron-Proton Collisions at HERA*, contributed paper to HEP99, Tampere, Finland.
- [122] ZEUS Collaboration, *Measurement of Differential Cross Sections for Dijet Production in Neutral Current DIS at high Q^2 and Determination of α_s* , contributed paper to HEP99, Tampere, Finland.
- [123] M. Botje, DESY-99-038 and hep-ph/9912439.
- [124] see e.g. A.H. Mueller, *QCD 20 Years Later*, Vol. 1, eds. P.M. Zerwas and H.A. Kastrup, World Scientific (1993).
- [125] Yu.L. Dokshitzer, B.R. Webber, Phys. Lett. **B352** (1995) 451.
- [126] Yu.L. Dokshitzer, G. Marchesini, B.R. Webber, Nucl. Phys. **B469** (1996) 63;
Yu.L. Dokshitzer, A. Lucenti, G. Marchesini, G.P. Salam, Nucl. Phys. **B511** (1998) 396;
Yu.L. Dokshitzer, A. Lucenti, G. Marchesini, G.P. Salam, JHEP **5** (1998) 3.
- [127] Yu.L. Dokshitzer, hep-ph/99111299;
M. Dasgupta, L. Magnea, G.E. Smye, JHEP **11** (1999) 25.
- [128] J. Blümlein and A. Vogt, Rev. Phys. **D58** (1998) 014020.
- [129] D. Graudenz, M. Hampel, A. Vogt, C. Berger, Z. Phys. **C70** (1996) 77.
- [130] G. Lobo, Proceedings of the Workshop Future Physics at HERA, Eds. G. Ingelman, A. De Roeck and R. Klanner, Vol. 1 537 (1995/1996).
- [131] H1 Collaboration, *Measurement of Dijet Cross Sections in Deep-Inelastic Scattering at HERA and a Direct Determination of the Gluon Density in the Proton*, contributed paper to ICHEP98, Vancouver, Canada.
- [132] H1 Collaboration, *A Measurement of the Proton Structure Function $F_2(x, Q^2)$ at High Q^2 at HERA*, contributed paper to ICHEP97, Jerusalem, Israel;
the final result is given in [28].
- [133] ZEUS Collaboration, J. Breitweg *et al.*, Eur. Phys. J. **C7** (1999) 609.
- [134] H1 Collaboration, C. Adloff *et al.*, Nucl. Phys. **B545** (1999) 21.

- [135] ZEUS Collaboration, J. Breitweg *et al.*, Eur. Phys. J. **C12** (2000) 35.
- [136] B.W. Harris and J. Smith, Phys. Rev. **D57** (19198) 2806.
- [137] H. Lai *et al.*, Phys. Rev. **D55** (1997) 1280.
- [138] ZEUS Collaboration, M. Derrick *et al.*, Z. Phys. **C65** (1995) 379;
H1 Collaboration, T. Ahmed *et al.*, Nucl. Phys. **B439** (1995) 471;
for a recent review see e.g. [41, 42].
- [139] H1 Collaboration, S. Aid *et al.*, Phys. Lett. **B356** (1995) 118;
H1 Collaboration, S. Aid *et al.*, Z. Phys. **C70** (1996) 609;
H1 Collaboration, C. Adloff *et al.*, DESY 99-091, submitted to Eur. Phys. J. **C**.
- [140] J. Kwiecinski, A.D. Martin, P.J. Sutton and K. Golec-Biernat, Phys. Rev **D50** (1994) 217;
J. Kwiecinski *et al.*, Phys. Lett. **B335** (1994) 220.
- [141] N. Brook, T. Carli, R. Mohr, M. Sutton and R.G. Waugh, Proceedings of the Workshop
Future Physics at HERA, Eds. G. Ingelman, A. De Roeck and R. Klanner, Vol. 1 613
(1995/1996).
- [142] G. Grindhammer, D. Krücker and G. Nellen, Proceedings of the Workshop on Monte
Carlo Generators for HERA Physics, Eds. A.T. Doyle, G. Grindhammer, G. Ingelman and
H. Jung, DESY-PROC-1999-02 36.
- [143] M. Kuhlen, Phys. Lett. **B382** (1996) 441.
- [144] H1 Collaboration, C. Adloff *et al.*, Nucl. Phys. **B485** (1997) 3.
- [145] J. Binnewies, B.A. Kniehl and G. Kramer, Phys. Rev. **D52** (1995) 4947.
- [146] J. Kwiecinski, S. LAng and A.D. Martin, Eur. Phys. J. **C6** (1999) 671.
- [147] H1 Collaboration, C. Adloff *et al.*, Eur. Phys. J. **C13** (2000) 415.
- [148] H1 Collaboration, C. Adloff *et al.*, Eur. Phys. J. **C13** (2000) 397.
- [149] ZEUS Collaboration, J. Breitweg *et al.*, DESY-00-017 (2000) and hep-ex/0002010, ac-
cepted by Phys. Lett. **B**.
- [150] A.H. Mueller, Nucl. Phys. (Proc. Suppl.) **18C** (1990) 125;
A.H. Mueller, J. Phys. **G17** (1991) 1443.
- [151] ZEUS Collaboration, J. Breitweg *et al.*, DESY 99-162, submitted to Phys. Lett. **B**;
ZEUS Collaboration, J. Breitweg *et al.*, Eur. Phys. J. **C6** (1999) 239.
- [152] H1 Collaboration, C. Adloff *et al.*, Nucl. Phys. **B538** (1999) 3.
- [153] G. Kramer and B. Pötter, Phys. Lett. **B453** (1999) 295.
- [154] H. Jung, L. Jonsson, H. Kuster, Eur. Phys. J. **C9** (1999) 383.

- [155] A.J. Askew, D. Graudenz, J. Kwiecinski, A.D. Martin, Phys. Lett. **B338** (1994) 92; J. Kwiecinski, A.D. Martin, A.M. Stasto, Phys. Lett. **B459** (1999) 644.
- [156] J. Bartels, V. Del Duca, M. Wusthoff, Z. Phys. **C76** (1997) 75.
- [157] H1 Collaboration, C. Adloff *et al.*, Phys. Lett. **B462** (1999) 440.
- [158] ZEUS Collaboration, M. Derrick *et al.*, Z. Phys. **C67** (1995) 93.
- [159] H1 Collaboration, S. Aid *et al.*, Nucl. Phys. **B445** (1995) 428.
- [160] H1 Collaboration, S. Aid *et al.*, Z. Phys. **C72** (1996) 573.
- [161] H1 Collaboration, C. Adloff *et al.*, Nucl. Phys. **B504** (1997) 3.
- [162] ZEUS Collaboration, J. Breitweg *et al.*, Eur. Phys. J. **C11** (1999) 271.
- [163] TASSO Collaboration, W. Braunschweig *et al.*, Z. Phys. **C45** (1989) 193;
 PLUTO Collaboration, Ch. Berger *et al.*, Phys. Lett. **B95** (1980) 313;
 OPAL Collaboration, P.D. Acton *et al.*, Z. Phys. **C53** (1992) 539;
 HRS Collaboration, M. Derrick *et al.*, Phys. Rev. **D34** (1986) 3304;
 MARK I Collaboration, J.L. Siegrist *et al.*, Phys. Rev. **D26** (1986) 969.
- [164] K.H. Streng, T.F. Walsh and P.M. Zerwas, Z. Phys. **C2** (1979) 237.
- [165] NOMAD Collaboration, J. Altegoer *et al.*, Phys. Lett. **B445** (1999) 439.
- [166] S. Carius and G. Ingelmann, Phys. Lett. **B252** (1990) 647;
 R. Szwed, G. Wrochna and A.K. Wróblewski, Mod. Phys. Lett. **A6** (1991) 245;
 M. Gazdzicki *et al.*, Mod. Phys. Lett. **A6** (1991) 981.
- [167] Z. Koba, H.B. Nielsen and P. Oelsen, Nucl. Phys. **B40** (1972) 317.
- [168] D. Kant, Proceedings of the Workshop Deep Inelastic Scattering and QCD, Nucl. Phys. B(Proc. Suppl.) **79** (1999) 453.
- [169] Yu.L. Dokshitzer, V.A. Khoze and S.I. Troyan, Int. J. Mod. Phys. **A7** (1992) 1875.
- [170] C.P. Fong and B.R. Webber, Phys. Lett. **B229** (1989) 289 and Nucl. Phys. **B355** (1991) 54.
- [171] S. Lupia and W. Ochs, Eur. Phys. J. **C2** (1998) 307.
- [172] A.V. Anisovich *et al.*, Nuovo Cimento **A106** (1993) 547.
- [173] D. Graudenz, Fortsch.Phys.45 (1997) 629-726;
 D. Graudenz, CYCLOPS program, private communication.
- [174] Yu. Dokshitzer, B.R. Webber, discussion at the 3rd UK Phenomenology Workshop on HERA Physics, Durham (1998).
- [175] P. Dixon, D. Kant, G. Thompson, J. Phys. G **25** (1999) 1453;
 D. Kant, Nucl. Phys. B (Proc. Suppl.) 453 (1999).

- [176] M. DasGupta and G.E. Smye, Nucl. Phys. B (Proc. Suppl.) 450 (1999).
- [177] ZEUS Collaboration, J. Breitweg *et al.*, accepted by Eur. Phys. J.
- [178] S.V. Chekanov, J. Phys. **G25** (1999) 59.
- [179] W. Ochs and J. Wosiek, Phys. Lett. **B289** (1992) 159; and Phys. Lett. **B304** (1993) 144 and Z. Phys. **C68** (1995) 269.
- [180] see e.g. DELPHI Collaboration, P. Abreu *et al.*, Z. Phys. **C50** (1991) 185; OPAL Collaboration, R. Akers *et al.*, Phys. Lett. **B320** (1994) 417.
- [181] G. Goldhaber *et al.*, Phys. Rev. Lett. **3** (1959) 181 and Phys. Rev. **120** (1960) 300.
- [182] A. Breakstone *et al.*, Phys. Lett. **B162** (1985) 400; UA1 Collaboration, C. Albajar *et al.*, Phys. Lett. **B226** (1989) 410 and Erratum *ibid.* **B229** (1989) 439; E735 Collaboration, T. Alexopoulos, Phys. Rev. **D48** (1993) 1931.
- [183] EHS/NA22 Collaboration, N.M. Agababian *et al.* Phys. Lett. **B422** (1998) 359.
- [184] NA35 Collaboration, T. Alber *et al.*, Z. Phys. **C66** (1995) 77; NA44 Collaboration, I.G. Bearden, Phys. Rev. **C58** (1998) 1656.
- [185] ALEPH Collaboration, D. Decamp *et al.*, Z. Phys. **C54** (1992) 75; DELPHI Collaboration, P. Abreu *et al.*, Phys. Lett. **B286** (1992) 201; OPAL Collaboration, G. Alexander *et al.*, Z. Phys. **C72** (1996) 389.
- [186] H1 Collaboration, C. Adloff *et al.*, Z. Phys. **C75** (1997) 437.
- [187] see e.g. L. Lönnblad and T. Sjöstrand, Eur. Phys. J. **C2** (1998) 165; L. Lönnblad and T. Sjöstrand, Phys. Lett. **B351** (1995) 293.
- [188] Bo Andersson, Markus Ringner, Phys. Lett. **B421** (1998) 283.
- [189] OPAL Collaboration, G. Abbiendi *et al.*, CERN-EP-2000-004, submitted to Eur. Phys. J. **C**.